The Modeling and Control of a Wind Farm and Grid Interconnection in a Multi-machine System

Siriya Skolthanarat

Dissertation submitted to the faculty of the
Virginia Polytechnic Institute and State University
in partial fulfillment of the requirements for the degree of

Doctor of Philosophy
in
Electrical Engineering

Virgilio Centeno
Jaime De La Ree
Yilu Liu
Fred Wang
Werner E Kohler

August 26th, 2009
Blacksburg, VA

Keywords: wind energy, grid interconnection, harmonic distortion, dynamic modeling

The Modeling and Control of a Wind farm
and
Grid interconnection in a multi-machine system

Siriya Skolthanarat

(Abstract)

This dissertation focuses on the modeling and control of WECS (Wind Energy Conversion System) in a multi-machine system. As one of the fastest growing renewable energy resources, the trend of the wind energy changes to variable speed wind turbines. The concept of the variable speed wind turbines is based on the variable speed according to the instantaneous wind speed of wind turbines. Since the utility grid requires the stable frequency and magnitude voltages, there must be a grid interconnection of the wind farm and the utility grid. The grid interconnection must support the concept of the variable speed wind turbines. Since each wind turbine locates in a different location in a wind site, it receives a different wind speed. Hence the grid interconnection must convert the variable frequency and magnitude output voltages of the wind turbines to the synchronous frequency and magnitude voltages of the grid.

With new technologies of power semiconductor devices, a power converter can operate with high voltage, high current, and high switching frequency. This results in a higher power capacity of a wind farm. The power converters, nonetheless, generate harmonic distortions to the utility grid. The harmonic distortions in the voltages and currents of the grid degrade the power quality. This results in the damage of electrical components in the power system such as capacitor banks, inductors, protection devices, etc. The harmonic distortions can be reduced with the technologies of the multi-level inverter. It is required that the wind energy provides the real and reactive power control for frequency and voltage stability. In order to achieve the power control, there must be the modeling and control of the power electronic grid interconnection.

The grid interconnection is modeled with linearization techniques. The models in frequency domain in the form of transfer functions are used to design the compensators in the control system. The model is considered as a SISO (Single Input Single Output) system to design the compensators in the SISO tool of the MATLAB. The selected control system is the current control that can control the real and reactive powers independently. Furthermore, since the grid interconnection is modeled separately for each sub-system, the control system is verified with

integration of the sub-systems. The grid interconnection is modeled in the Simulink and simulated in the PSCAD. Chapter 2 presents the modeling and control of the grid interconnection and verification of the system integration.

In reality, the power system is comprised of multi-machines. They affect the power system stability, reliability, and quality. The dynamic modeling of an aggregated wind farm with synchronous generator and grid interconnection in a multi-machine system is presented in chapter 3. The test system is a 10-bus system with three generators and three loads. The dynamic modeling involves the power flow calculations that determine the equilibrium points of the system. The system is modeled with small signal equations of wind turbines, synchronous generators, and grid interconnection in the time domain and arranged in the state space form. The system characteristics can be determined by poles or eigenvalues obtained from the characteristic equations. Since the system is a MIMO (Multi Input Multi Output) system, the optimal control theory is used to reduce the deviation of system behaviors during disturbances. The LQR (Linear Quadratic Regulator) is utilized to control the system with eigenvalue assignment method. Simulation results in Simulink are illustrated in chapter 4.

To

My mother, sister and brother

Acknowledgement

I would like to thank Dr.Virgilio Centeno who advised me the do research in the wind energy. He also motivated me to the research regarding the dynamic stability of the power system. I am very grateful to my committees, Dr.Yilu Liu who accepted me to the power system and helped me in the hard time, Dr.Virgilio Centeno and Dr.Jaimes De la Ree for financial support, Dr. Fred Wang for the power electronic knowledge, and Dr. Werner Kohler. I also would like to thank all my colleagues and labmates for the cheerful meetings. I am thankful to the professors in the Electical Engineering department at Virginia Tech for their knowledge and time.

All other thanks I would like to give to my family, Royal Thai government, professors at school and college who supported me. Without them, I cannot come to this far.

Table of Contents

Chapter1 Introduction

Chapter2 Grid Interconnection

Chapter3 Dynamic modeling of a multi-machine system

Chapter 4 Simulation Results

Chapter 5 Conclusion and future work

Appendix

List of Illustrations

Chater1 Introduction

Chapter2 Grid Interconnection

Chapter3 Dynamic modeling of a multi-machine system

Chapter 4 Simulation Results

List of Tables

Chapter2 Grid Interconnection

Chapter3 Dynamic modeling of a multi-machine system

Chapter 1-Introduction

1.1 Motivation

The call for improved renewable energy technologies is increasing due to the global warming. It affects humans in several aspects such as economies, public health, environment, etc. The global warming is caused from green house gases, which comes from burning fossil fuels such as oil or coal. The advent of renewable energy resources is the promising solution to the problems. There are several renewable energy resources for the electrical power system. Among those, wind energy is one of the fastest growing renewable energy resources. In Sep 2008, the capacity of the wind energy in the U.S. was around 21,017 MW totally while more than 7,500 MW are under construction [1]. The advantage of the wind energy for the power system is not only its free and clean energy but also its high capacity. The high electrical power can be generated from an aggregation of multiple wind turbines as a wind farm or wind park. To interconnect the wind energy to the utility grid, there must be an appropriate grid interconnection and control system to ensure high power quality and stability. As the level of penetration of the wind energy is increasing, there are regulations for the interconnection regarding the power quality and reliability.

The power electronic grid interconnection supports the variable speed wind power, real and reactive power control, and reduces the influences of fluctuations in the wind such as voltage flickers. Nonetheless, it generates other problems due to the switching devices of the power converters. One problem of the grid interconnection is harmonic distortions of the grid currents and voltages. The harmonic distortions degrade the power quality. This leads to more severe problems in the power system such as transformer saturations, failure of protective devices, etc. The first part of this research is about the grid interconnection of a wind farm that reduces the harmonic distortions and supports the variable speed wind turbines.

Most researches of the wind energy focus on the behavior of one wind turbine, one generator and the power electronic grid interconnection connected to an infinite bus. In reality, the wind energy and the power system affect each other in accordance with the level of penetration of the wind energy. Since the power system is complex and consisted of a lot of components, it is challenging to find a model of a multi-machine system with the wind energy. Thus, the second part is relevant to dynamic modeling of an aggregated wind farm in a multi-machine system. The modeling introduced in this dissertation focuses on synchronization and voltage fluctuations of the generators. The synchronization stability relates to the rotor angle stability of the generators in the system. The power system is not constant but subjected to disturbances at all times. The dynamic model demonstrates the effects of the disturbances to the system. To provide secured stability and reliability electrical power to customers, an optimal control theory is used to reduce the impacts of the disturbances.

1.2 Wind generation

The wind energy is used for a long time in farms to grind grains or pump water in the form of a wind mill. The principle is to convert the kinetic energy from the wind to the mechanical energy. This principle is applied to the wind energy in the power system. A wind turbine captures the kinetic energy from the flowing air and changes it to the mechanical energy. A generator installed in the wind turbine converts the mechanical energy to the electrical energy. As shown in figure 1.1, the kinetic energy of the wind turns the rotor blades of the wind turbine. This results in revolving of the shaft of the generator, which is mounted on the rotor blades. The generator converts the mechanical energy from the rotating shaft to the electrical energy. It is optional to tie the low speed shaft of the rotor blades to the high speed shaft of the generator with a gear box. In some cases, gearboxes are undesirable because they are expensive, bulky, and heavy. A multi-pole generator is an alternative way of a gearless system. The configurations of wind turbines and the grid interconnection depend on the type of generators that will be described in section 1.6.

The power cable transmits the electrical power to a transformer. The transformer steps up the low voltages of the generator to the distribution or sub-transmission level of the connected system. The voltages from the generator are typically in a few hundred volts. The maximum output voltage of the wind turbines is 690 Volts.

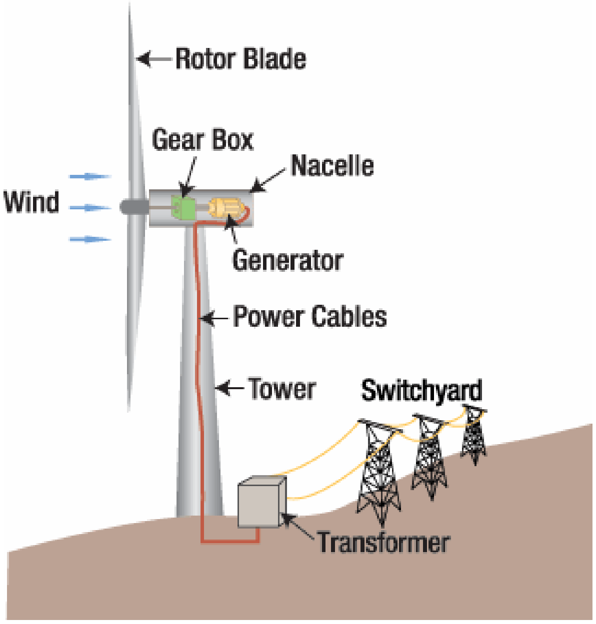

Figure 1.1 Wind generation

1.3 Wind turbine

To fully understand the wind energy, it is important to learn about wind turbines. Wind turbines can be categorized according to the axis of rotation: vertical and horizontal axis. Figure 1.2 shows three types of the vertical wind turbines.

Figure 1.2a) Darrieus winds turbine

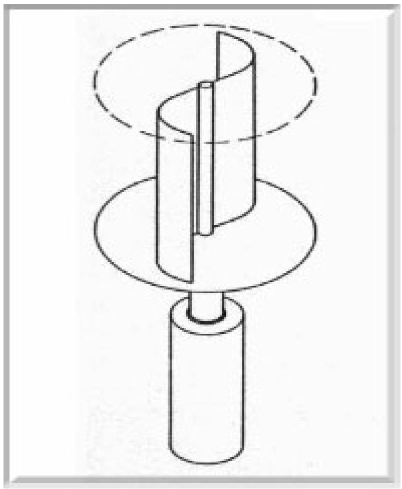

Figure 1.2b) Savonius wind turbine

Figure 1.2c) H-rotor wind turbine

The vertical wind turbines are suitable for low power applications. The power efficiency is limited to 25% [2]. The advantage of the vertical wind turbines is that the generator and transformer can be placed on the ground near the rotor blades. This results in low installation and maintenance cost.

More popular type of wind turbines, as shown in figure 1.3, is horizontal wind turbines [3]. Similar to the vertical wind turbines, the horizontal wind turbines can be built with two or three blades. Apart from the parts introduced in section 1.2, the wind turbine has control system that controls the speed of rotor blades. The anemometer measures the wind speed and transmits the data to the controller. The pitch angle of the rotor blades is controlled by the controller to attain the maximum wind power and to limit the mechanical power in case of the strong wind. The rotor blades are pitched to decrease the angle of attack from the wind when the rated power is reached. The yaw drive can turn the wind turbine compartment or so called nacelle according to the direction of the wind measured by the wind vane.

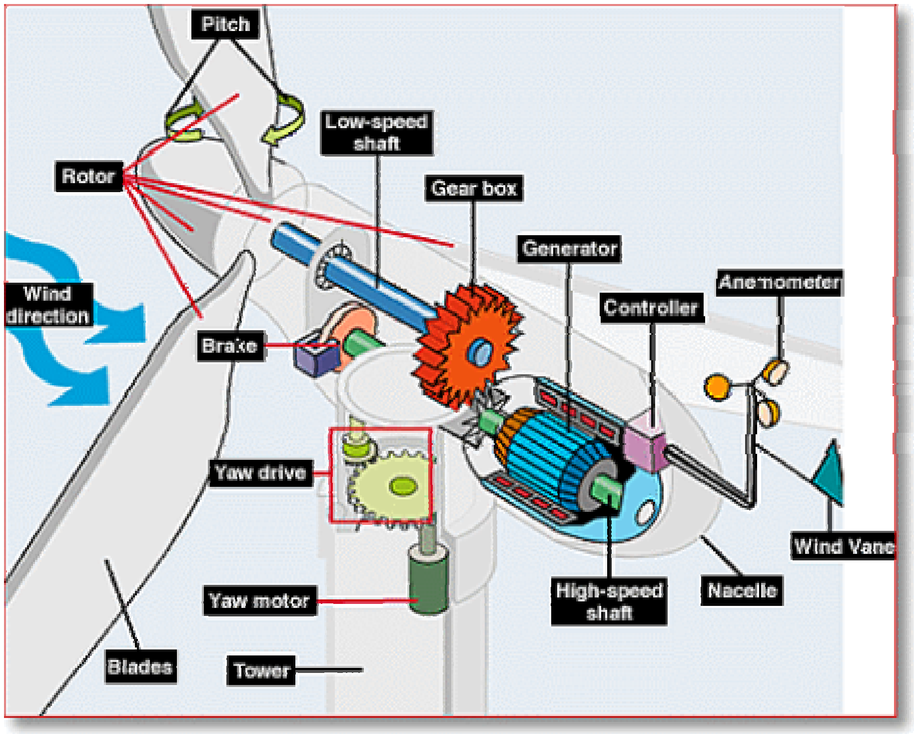

Figure 1.3 Horizontal wind turbine

In addition to the pitch control, the maximum power from the wind can be limited by passive stall control for small and medium-size wind turbines. The stall control avoids the rotation of the blades. Contrarily to the pitch-angle control, passive stall control has fixed pitch-angle rotor blades. The passive stall control relates to the design of the rotor blades that leads to turbulence or so called stall on the back of the blades to reduce the power extracted from the wind [4]. As the capacity of wind turbines is increasing, active stall control is used for large wind turbines, more than 1MW. The active stall control is similar to the pitch-angle control. The rotor blades are rotated to obtain the maximum power extract. When the extracted power reaches the rated power, opposite to the pitch-angle control, the active stall control turns the rotor blades to increase the angle of attack from the wind to provoke the turbulence [4].

Wind turbines can be distinguished into 2 categories, fixed speed and variable speed wind turbines. The fixed speed wind turbines are connected directly to the utility grid and operate with the synchronous speed of the grid angular frequency regardless of the wind speed. The fluctuations in the wind generate mechanical stresses to the generator. Furthermore, since the wind generation system is connected to the utility grid directly, the fluctuations of the wind appear on the electrical side. The variable speed wind turbines operate in an opposite way. The speed of the generator is varied according to the wind speed solving the problem of the mechanical stresses. As a result, the output voltages of the generator have variable amplitudes and frequencies. Hence there must be a grid interconnection to convert the variable magnitude and frequency voltages of the wind turbines to the synchronous frequency of the supply grid. The indirect connection with the grid interconnection reduces the problems caused from the mechanical stresses.

1.4 Wind energy

Like other substances, the moving air caused from the variations of the air pressure and temperature has the kinetic energy. The relationship of the kinetic energy, *E*, of the flowing air mass *m*, with velocity v_w can be expressed as

$$E = \frac{1}{2} m {v_w}^2$$

The instantaneous power of the wind flowing through an area A_v can be expressed as

$$P_{wind} = \frac{dE}{dt} = \frac{1}{2} \rho_{air} \cdot A_v \cdot v_w^3 \qquad \text{equ.1.1}$$

Where ρ_{air} is the mass density of the flowing air

In the light of variable speed wind turbines, the rotor blades rotate freely in accordance with the speed and direction of the wind. The power extracted from the wind is dependent on the rotor power efficiency to capture the wind power. This is based on the fact that the speed of the wind after passing the rotor blades cannot be zero velocity leading to efficiency less than 1. This has nothing to do with the efficiency of the generator. Refer to Betz limit or Betz law, the mechanical power captured by the wind turbine depends on the rotor power efficiency of the turbine C_p as shown below

$$P_{tur} = \frac{1}{2} C_p(\lambda) \cdot \rho_{air} \cdot A_v \cdot v_w^3 \qquad \text{equ.1.2}$$

The rotor power efficiency of the turbine C_p is the function of the blade tip speed ratio λ and blade pitch angle β. Equation 1.3 and 1.4 express the relationship of C_p *and* λ, β with a graph illustrated in figure 1.4.

$$C_p(\lambda, \beta) = 0.5176(\frac{116}{\lambda_i} - 0.4\beta - 5) \cdot e^{-\frac{21}{\lambda_i}} + 0.0068\lambda \qquad \text{equ.1.3}$$

$$\frac{1}{\lambda_i} = \frac{1}{\lambda + 0.08\beta} - \frac{0.035}{\beta^3 + 1} \qquad \text{equ.1.4}$$

The maximum rotor power efficiency, regardless of the configurations, is 0.593 [5]. After passing rotor blades, the downstream wind has lower speed and energy. Therefore, wind turbines in a wind farm affect each other. Wind turbines, typically, are located apart from the others three times of their rotor radius to avoid the wake effect [6]. If the tip speed ratio is less than 3, the wake effect reduces the maximum rotor power efficiency further [5]. The tip speed ratio can be calculated from

$$\lambda = \frac{\omega_b R}{v_w} \qquad \text{equ.1.5}$$

Where ω_b is the rotor speed in radian/s

R is rotor radius from axis to tip in meter

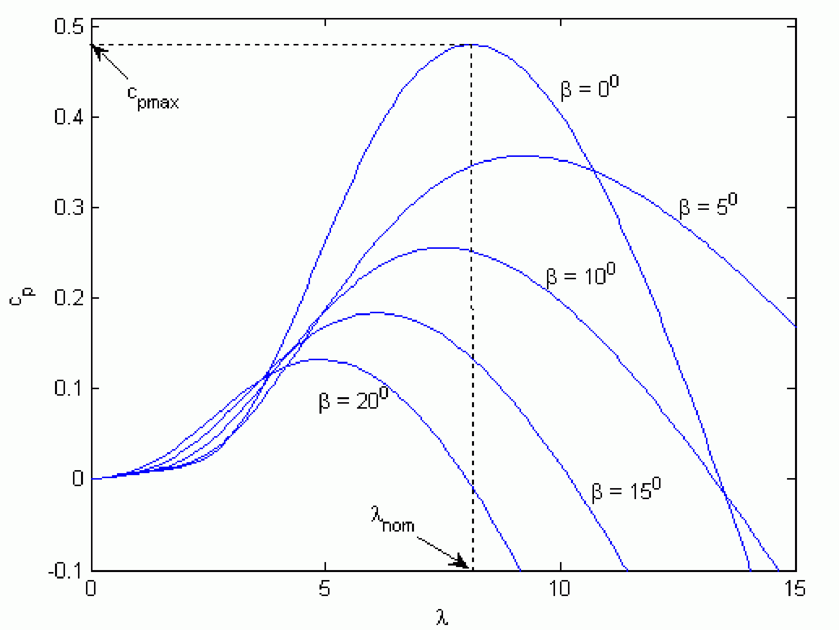

Figure 1.4 Rotor power efficiency vs. Tip speed ratio

1.5 Wind farm

One main advantage of the wind energy is that multiple wind turbines can be aggregated to generate the high power. A wind farm or wind park is comprised of tens or up to a few hundred of wind turbines and can locate onshore and offshore. The offshore wind farm generates more stable power than onshore wind farm because the wind speed is higher and steadier [7]. Figure 1.5 shows an onshore and offshore wind farm. Furthermore, the wind energy can be a grid connected or stand alone system. In a remote area, a group of small wind turbines supply the electrical power to households or business buildings separately from the grid. Even though the initial installation cost is high, it is worth investment for lifetime self-generating electricity power units.

As described in previous section, variable speed wind turbines mitigate the problems of the mechanical stresses. Because of the variable magnitude and frequency outputs of the variable speed wind turbines, there must be power electronic grid interconnection to decouple the outputs of the wind turbines to the grid. Moreover, the rotor blades of the wind turbines rotate following to the wind speed in their vicinity areas. As the wind speed is different in each location of a wind farm, each wind turbine rotates with different speed. Therefore, it is necessary that each wind turbine has individual connection to the power electronic grid interconnection.

Figure 1.5 a) Onshore wind farm

Figure 1.5 b) Offshore wind farm

Figure 1.6 illustrates a group connection and individual connection of a wind farm [8]. The group connection eliminates the variable speed concept since all wind turbines are connected to one converter. Hence they must operate with same speed. Contrarily, the individual connection supports the concept of the variable speed. Moreover, this type of the connection provides reliability to the power system since only one converter is crucial, which is the grid-side converter. When one of the rotor-side converters is inoperable, other wind turbines can supply the power. For the group connection, both converters are critical. A fault in either converter results in failure of the wind farm.

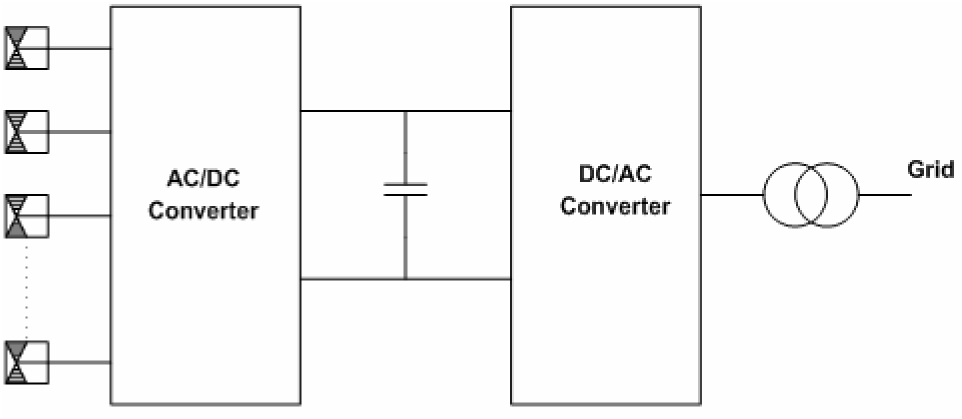

Figure 1.6 a) Group connection

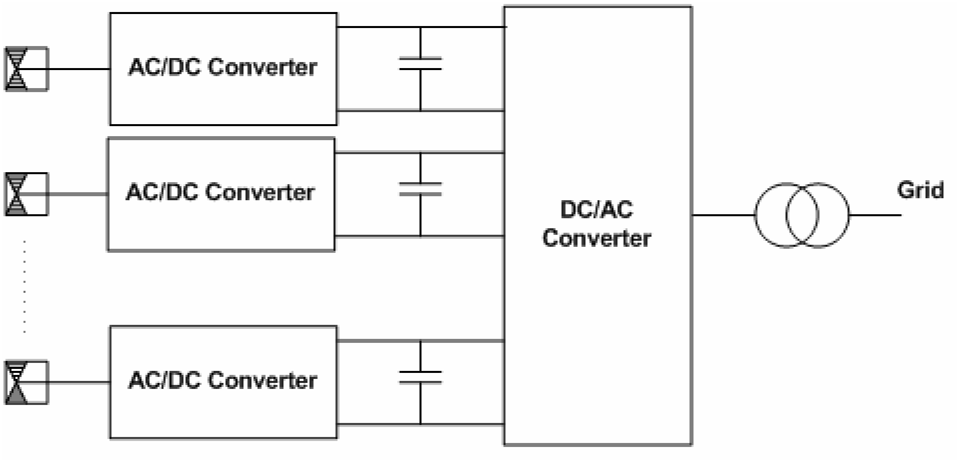

Figure 1.6 b) Individual connection

1.6 The power electronic grid interconnection

In the context of the grid interconnection, it is inevitable to learn about the wind generators. Each type of the generators requires different power electronic grid interconnection. Induction generator is widely used in the wind industry. There are two types of the induction generators. The squirrel-cage induction generator can be directly connected to the utility grid or connected with a full-rated power electronic interface at a variable speed [9]. The system with a fixed speed is inexpensive due to its simplicity and low maintenance requirements. Nonetheless, the direct connection of the wind turbines and the utility grid causes the mechanical stress problems and high inrush current during start up. This problem can be solved by a soft-starter mechanism. A soft starter is comprised of thyristors, a power electronic semiconductor device, limiting the maximum inrush current [8]. After start up, the thyristors are bypassed to avoid thermal breakdown, as shown in figure 1.7.

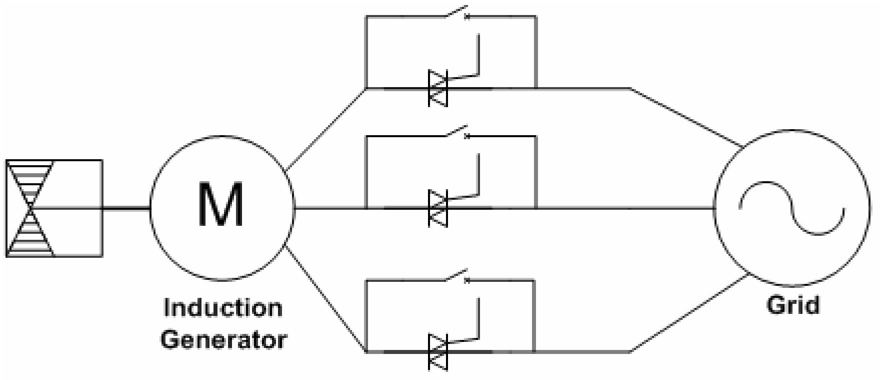

Figure 1.7 Soft starter

Additionally, the induction generator requires reactive power from the utility grid that causes unacceptable conditions such as the voltage drop or low power factor. The compensated reactive power can be supplied from a switched capacitor bank or a power converter. For the fixed speed or direct connection induction generators, the switched capacitor banks can supply the reactive power, thereby improving the power factor. For the variable speed squirrel-cage induction generator, the power converter, therefore, must be able to provide reactive power to the generators. The simplest topology is the back-to-back converter as shown in figure 1.8.

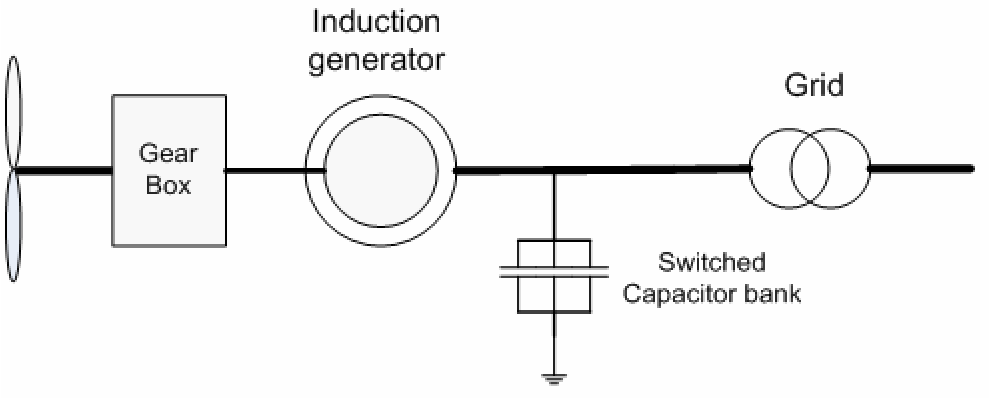

Figure 1.8 a) Squirrel-cage induction generator with direct connection to the grid

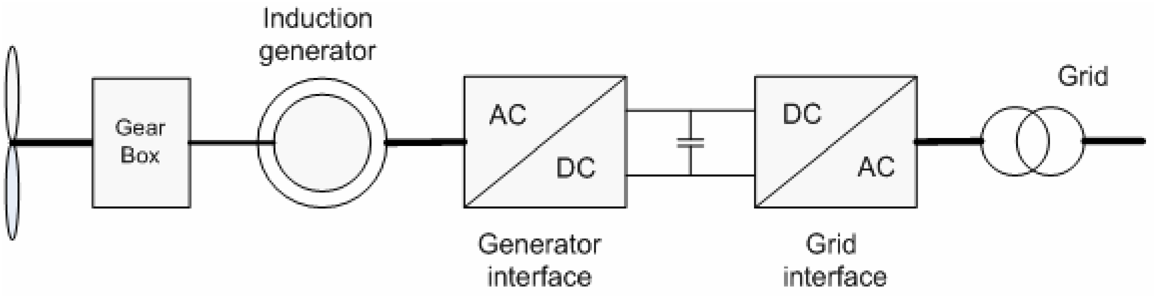

Figure 1.8 b) Squirrel-cage induction generator with power converters

For the direct connection, the induction generator has to operate at the synchronous frequency of the grid. Thus, there must be a gearbox to increase the low speed shaft of the rotor blades to the speed of the grid.

The doubly-fed induction generator is partly connected to the grid. That allows only a part of the power fed through the power converter. Therefore, the nominal power of the converter is less than the nominal power of the generator. The stator of the generator is directly connected to the grid whereas the rotor is connected to the power converter decoupling the angular frequency of generator rotor from the grid, as shown in figure 1.9. To supply the power to the grid, the doubly-fed induction generator must operate at super-synchronous frequency of the grid. Therefore, it is necessary to increase the speed of the rotor blade shaft with the gearbox.

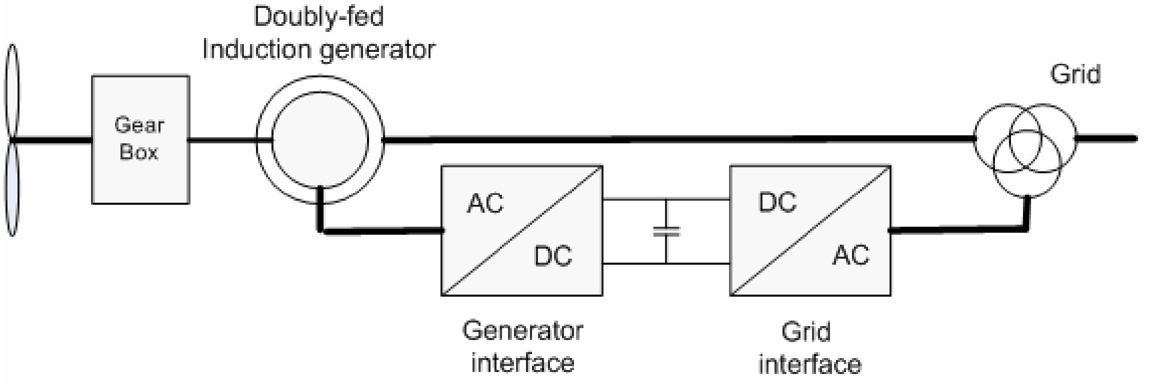

Figure 1.9 Doubly-fed induction generator

Another type of the generators utilized in a wind farm is a synchronous generator. The rotor winding of the synchronous generator can be excited by an external field exciter, which requires the field current supplied from the grid with an AC-DC converter as shown in figure 1.10. The stator winding is connected to the full-rated power converters supporting the variable speed concept. A multi-pole synchronous generator can eliminate the gear box as mentioned previously. The relationship of the multiple poles and frequency can be expressed as

$$f_{(elec)} = \frac{P}{2} f_{(rotor)} \qquad \text{equ.1.6}$$

Where P is number of poles

This results in a simpler system and reduction in maintenance cost. The synchronous generator can be also excited by an internal permanent magnet, as shown in figure 1.11. The gearless multi-pole permanent magnet synchronous generator is attractive because it is light and requires low maintenance cost. It also reduces the cost of transportation and installation. Furthermore, it is considerably efficient compared to the other types of generators.

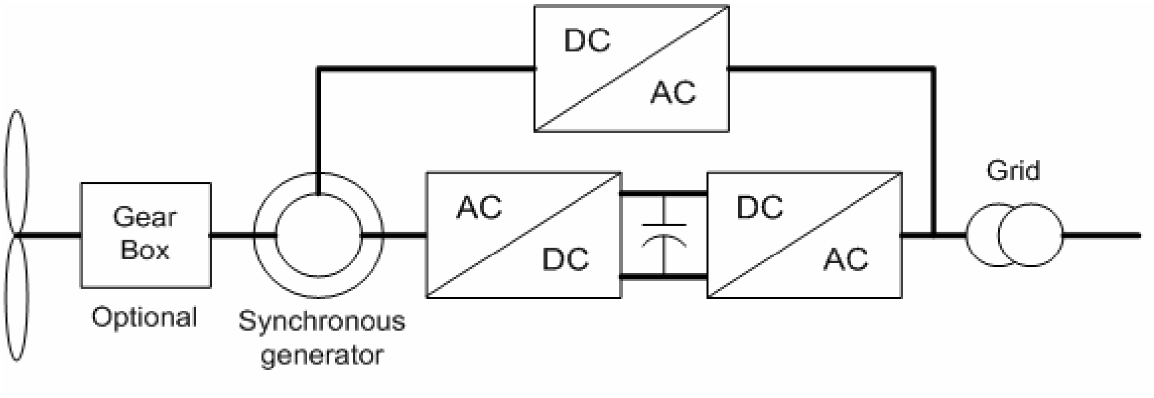

Figure 1.10 Synchronous generator with a field exciter

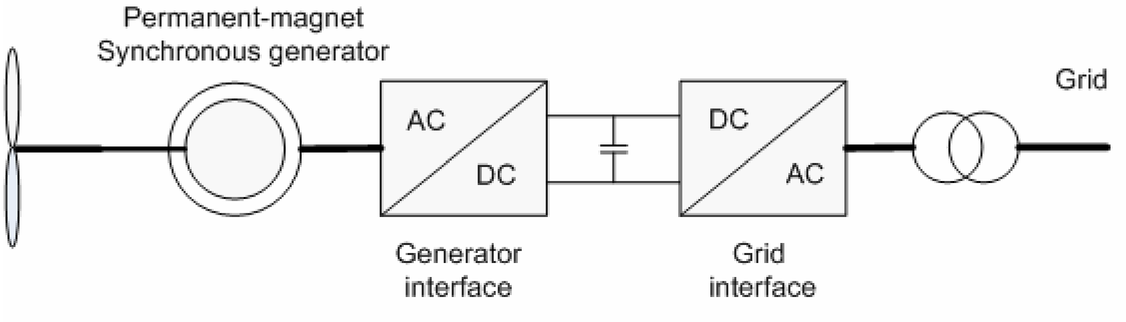

Figure 1.11 Permanent magnet synchronous generator

1.7 Power system

The power system relates to the transmission of the electricity produced from generating units to loads in various locations throughout the network. The electrical power network is consisted of generators, transformers, transmission lines, protective devices, customers, etc. The electrical power network can be categorized according to the voltages of the network to 3 levels [10]:

a) Transmission level: The operating voltage in this level is the highest, 230 KV and above. The output voltages from the generating units, which are in the range of 11-35 KV, are stepped up by transformers to the transmission level. The capacity of power plants is large. The generating units are, typically, steam or gas turbines.

As the power capacity of the wind power is growing, it can be connected to transmission network based on availability of the wind source.

b) Sub-transmission level: The sub-transmission network transmits the power generated by large power plants in the transmission network to the distribution network. Therefore, the operating voltage in this level is between the transmission level and distribution level, which is in the range of 34.5 KV to 138 KV. Some large industrial customers are connected to the sub-transmission network directly.

c) Distribution level: The operating voltage in this level is between 4KV and 34.5 KV. In this level, the power supplied to the customers can be either from the sub-transmission level or directly from distribution power plants. The small power plants in distribution level can be wind turbines, solar cells, fuel cells, micro turbines, and etc.

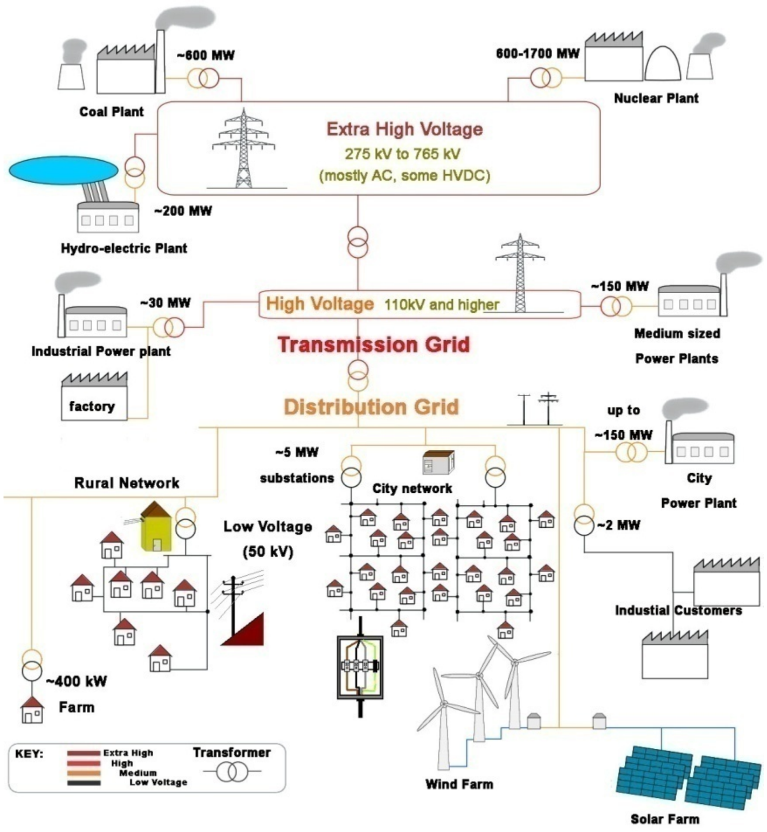

Figure 1.12 Power system

1.8 Power system stability

The power system involves many components that are not constant but change at all times. Switching on or off of a light bulb causes a change in load demand. Moreover, the power system is subjected to disturbances perturbing steady states of the system. The loss of equilibrium points leads to a failure of a critical component such as a generator or a transmission line. One faulted component may result in cascading failure of other components, and finally power outages. Therefore, it is important to understand about power system stability.

Power system stability means the capability of the power system to regain to equilibrium points after experiencing disturbances. The system retrieving to the original equilibrium points after small disturbances is called oscillation stability or dynamic stability. The small disturbances are in the form of load changes, variations of excitation field circuits, and changes in mechanical torques. The system that recovers from large disturbances reaches new equilibrium points is called transient stability. The large disturbances can be the loss of a large generator or a short circuit of a transmission line [11]. The dynamic stability is determined by the rotor angle stability and voltage stability [12].

The rotor angle stability concerns the synchronization of generators in the system. Figure 1.13 illustrates a system comprised of a synchronous generator connected to an infinite bus. An infinite bus represents a strong system, which can be substituted by a constant voltage source. The generator is represented by a voltage source behind transient reactance $x_d^{'}$. The modeling of a synchronous generator will be fully described in chapter 3. The active power generated by the generator to the system can be expressed as

$$P_e = \frac{E_g E_N}{X_T} \sin\delta \qquad \text{equ.1.7}$$

Where δ is the rotor angle

X_T is the total reactance $= x_d^{'} + x_{tx} + (x_1 \| x_2)$

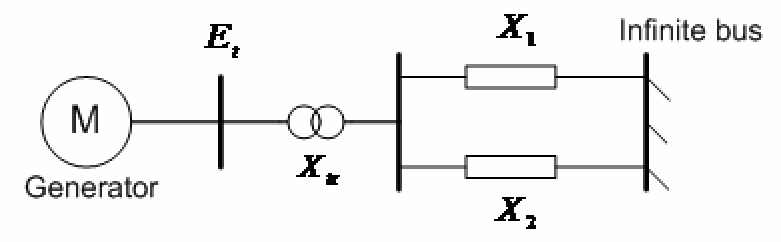

Figure 1.13 a) A single generator system

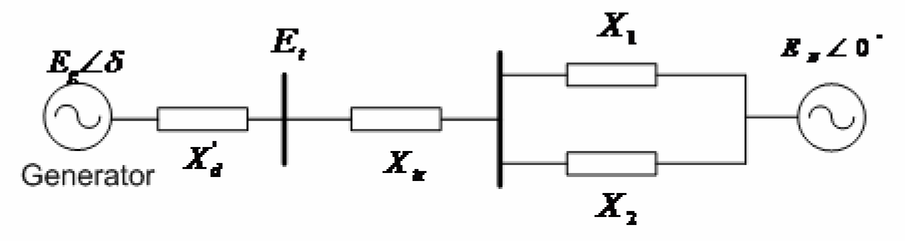

Figure 1.13 b) The reactance model of a single generator system

The inequality of the generated electrical power and mechanical power supplied to the turbine shaft results in acceleration or deceleration of the rotors of the generators. If the mechanical power is more than the electrical power, the generator is accelerated resulting in increasing of the rotor speed. On the other hand, when the electrical power is less than the mechanical power, the generator is decelerated resulting in decreasing of the rotor speed. Both acceleration and deceleration causes rotor angle separation of that generator respect to the other generators in the system. The increasing or decreasing of one rotor angle leads to the lack of synchronization of the generators.

As seen from figure 1.14, the rotor of the generator experiences a step change in the mechanical power from P_{m0} to P_{m1}. The generator rotor is accelerated since the mechanical power P_m is more than the electrical power P_e. The initial rotor angle δ_o increases to δ_1. At this point, the electrical power is equal to the mechanical power. The rotor angle continues increasing to $\delta_{\max}$. Beyond point b, the electrical power is more than the mechanical power. The generator rotor is decelerated until it reaches point d. Then the rotor angle swings back to point b. The area A1 and A2 represent the energy gained during the acceleration and the energy lost during the deceleration, respectively. For a stable system, the decelerating energy is more than or equal to the accelerating energy. In the other words, the area A2 is more than or equal to the area A1.

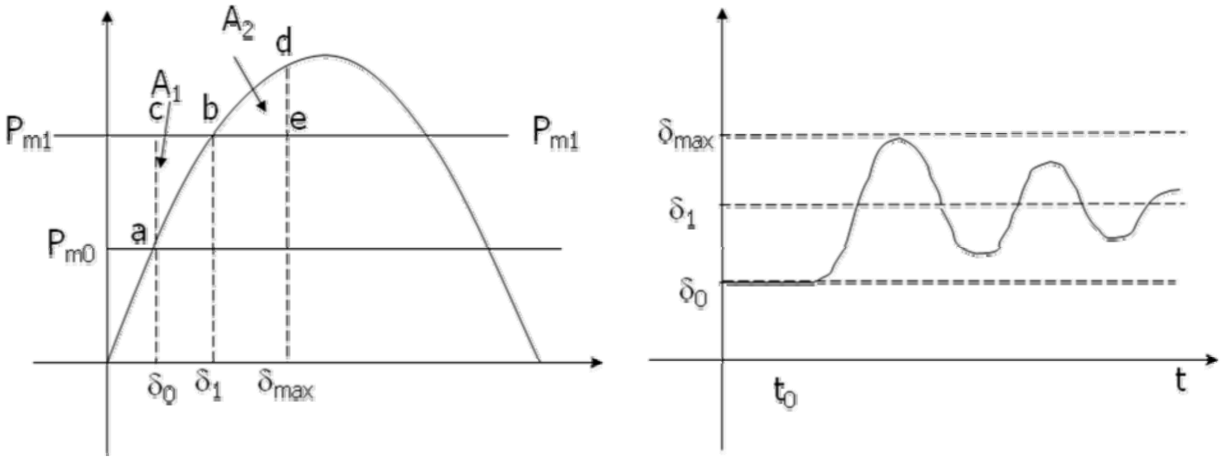

Figure 1.14 Power-angle curve

1.9 Dynamic modeling

The dynamic modeling is relevant to analysis of the steady state stability of a system. This means that the system restores the pre-fault equilibrium points after perturbations. In this dissertation, the equilibrium points of the system are determined by Newton Raphson power flow. The dynamic performance of the system involves the linearized model of a synchronous generator, an aggregated wind farm, and a grid interconnection in a multi-machine system. The dynamic modeling can be achieved in different ways. One way is to simulate in a software package such as SIMULINK Power System Block set, PSS/E, PSCAD, or DIgSILENT. The other way is to program the system with source codes. There are two methodologies of modeling in software packages. One methodology is the modeling by the control strategies of the wind generation. [13] presents modeling of GE wind turbines, published in 2003. This paper focuses on the wind turbine control, electrical control, and wind power control. By this method, the state variables of the generators and converters are avoided. [14] presents the modeling of an aggregated wind farm in a small power system simulated in PSS/E. This paper utilizes the modeling presented in [13] and analyzes for short circuit faults.

The other method is to model a test system with differential equations of wind turbines, generators, and converters. There are some differences in detail and applications for each paper. [15] and [16] determine the initial values of the variables by load flow and algebraic equations. [17]-[19] demonstrate the dynamic modeling of a wind farm connected to the grid represented by an infinite bus. [20] models the dynamic performance of a wind farm connected to an infinite bus in frequency domain and verifies the model with the time domain simulation in PSCAD. [21] demonstrates the modeling of parallel wind turbines in a stand-alone system. The differential equations of induction generators are solved by Runge-Gutta integration method with automatic adjustment of step and simulated in MATLAB. This paper focuses on the interaction of parallel wind turbines in steady-state and transient simulations such as load and generator variations. [22] presents the modeling of a wind farm during steady state and faults. This paper mentions the influences of the wake effect, types and locations of wind turbines, and shadow effect. The model is verified with experimental results of wind farms installed in Portugal. [23] validates the modeling of a wind farm represented by a single unit. Nonetheless, it is necessary in some specific cases that a wind farm has to be modeled with more than one single unit. [24] models a wind turbine connected to an infinite bus with dynamic phasor modeling. The model includes the Fourier series and separates the model to positive and negative sequence models. So the models can predict the system in both balanced and unbalanced conditions. [25] describes the modeling of the wind and PV energy in a micro grid system. This paper models the system in time domain and uses eigenvalue analysis to analyze the system stability.

Chapter 3 in this dissertation introduces dynamic modeling of an aggregated wind farm in a multi-machine system. The test system is programmed in MATLAB and simulated in time domain in SIMULINK. In fact, the power system is a non-linear system represented by a set of differential equations. Since the equilibrium points are the points of interest, the power system can be linearized. A set of first order nonlinear differential equations is defined as [26]

$$x_i^{\bullet} = f_i(x_1, x_2, \ldots, x_n; u_1, u_2, \ldots, u_n; t) \qquad \text{equ.1.8}$$

Where x is vector of state variables

u is a vector of inputs

$$x_i = \begin{bmatrix} x_1 \\ x_2 \\ \vdots \\ x_n \end{bmatrix} \qquad\qquad u_i = \begin{bmatrix} u_1 \\ u_2 \\ \vdots \\ u_n \end{bmatrix}$$

Nonlinear state variables can be represented as averaged variables at operating point with perturbations or so called small signal variables.

$$x_i = \bar{x}_i + \hat{x}_i \qquad \text{equ.1.9}$$

Where (-) denotes the averaged variable at operating point

(^) denotes the small signal variable

The nonlinear function *f(x,u)* can be expressed in terms of Taylor's series expansion. The perturbations are assumed to be so small that the second order and higher order terms can be neglected.

$$\begin{aligned} f_i(\bar{x}+\hat{x},\bar{u}+\hat{u},t) = f_i(\bar{x},\bar{u},t) + \left.\frac{\partial f_i}{\partial x_1}\right|_{\bar{x},\bar{u}}\cdot\hat{x}_1 + \ldots + \left.\frac{\partial f_i}{\partial x_n}\right|_{\bar{x},\bar{u}}\cdot\hat{x}_n \\ + \left.\frac{\partial f_i}{\partial u_1}\right|_{\bar{x},\bar{u}}\cdot\hat{u}_1 + \ldots + \left.\frac{\partial f_i}{\partial u_n}\right|_{\bar{x},\bar{u}}\cdot\hat{u}_n + h.o.t \end{aligned} \qquad \text{equ.1.10}$$

The term *h.o.t* means the second and higher order terms, which can be neglected. Substituting equation 1.9 and 1.10 into equation 1.11 yields

$$\begin{aligned} \bar{x}^{\bullet}{}_i + \hat{x}^{\bullet}{}_i = f_i(\bar{x},\bar{u},t) + \left.\frac{\partial f_i}{\partial x_1}\right|_{\bar{x},\bar{u}}\cdot\hat{x}_1 + \ldots + \left.\frac{\partial f_i}{\partial x_n}\right|_{\bar{x},\bar{u}}\cdot\hat{x}_n \\ + \left.\frac{\partial f_i}{\partial u_1}\right|_{\bar{x},\bar{u}}\cdot\hat{u}_1 + \ldots + \left.\frac{\partial f_i}{\partial u_n}\right|_{\bar{x},\bar{u}}\cdot\hat{u}_n \end{aligned} \qquad \text{equ.1.11}$$

The above equation satisfies the equality of nominal and perturbation terms. Therefore, we can separate equation 1.11 to two terms

$$\bar{x}^{\bullet}{}_i = f_i(\bar{x},\bar{u},t)$$

$$\hat{x}^{\bullet}{}_i = \left.\frac{\partial f_i}{\partial x_1}\right|_{\bar{x},\bar{u}}\cdot\hat{x}_1 + \ldots + \left.\frac{\partial f_i}{\partial x_n}\right|_{\bar{x},\bar{u}}\cdot\hat{x}_n + \left.\frac{\partial f_i}{\partial u_1}\right|_{\bar{x},\bar{u}}\cdot\hat{u}_1 + \ldots + \left.\frac{\partial f_i}{\partial u_n}\right|_{\bar{x},\bar{u}}\cdot\hat{u}_n \qquad \text{equ.1.12}$$

A linearized dynamic system can be expressed in state space form as

$$\dot{x}(t) = Ax(t) + Bu(t) \qquad \text{equ.1.13}$$

Output equation

$$y(t) = Cx(t) + Du(t) \qquad \text{equ.1.14}$$

Where x is a vector of state variables

u is a vector of input variables

y is a vector of output variables

A is a state matrix

B is an input matrix or control matrix

C is an output matrix or observation matrix

D is a coefficient matrix

The state space model demonstrates the system in time domain. By applying Laplace's transformation, the system can be expressed in frequency domain.

$$sX(s) = AX(s) + BU(s)$$

$$(sI - A)X(s) = BU(s)$$

$$X(s) = (sI - A)^{-1} BU(s)$$

$$Y(s) = \{C(sI - A)^{-1} B + D\}U(s)$$

The output transfer function

$$G(s) = \frac{Y(s)}{U(s)} = \{C(sI - A)^{-1} B + D\}$$

The inverse of the matrix $(sI - A)$ can be found by

$$(sI - A)^{-1} = \frac{adj(sI - A)}{\det(sI - A)} \qquad \text{equa.1.15}$$

Therefore, the state variables and outputs in equation 1.13 and 1.14 have roots or so called eigenvalues found by setting the denominator of equation 1.15 equal to zero

$$\det(sI - A) = 0 \qquad \text{equ.1.16}$$

The equ.1.16 is the characteristic equation of the state variables and outputs of the system. The state space model can be drawn in block diagram as shown in figure 1.15.

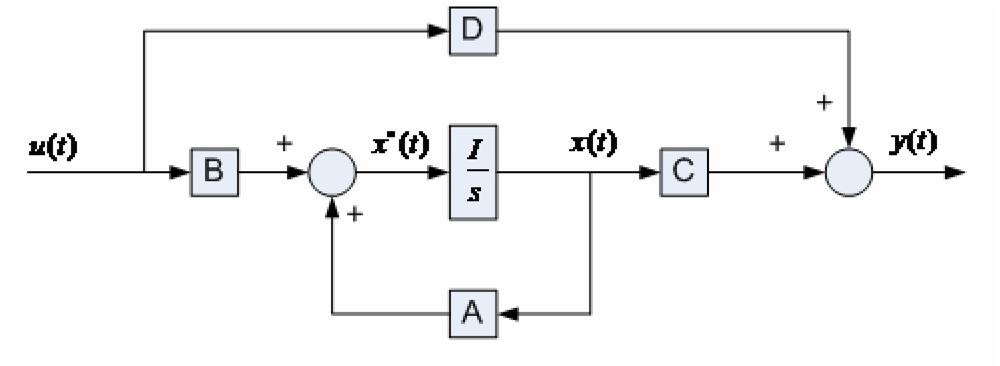

Figure 1.15 Linearized state space model

The stability of the system can be determined by locations of roots or eigenvalues. For a stable system, eigenvalues must lie in LHP (left half plane) of the S-plane. In the other words, the real part of all eigenvalues must be negative. Typically, the eigenvalues are in complex form.

$$\sigma \pm j\omega \qquad \text{equ.1.17}$$

Each eigenvalue is called a mode. The real part or σ is called damping representing the decay rate of that mode. The higher damping of that mode is, the faster the oscillation of that mode decays to zero. ω is called angular frequency representing the frequency of oscillation. The period of oscillation can be found by [27]

$$T = \frac{2\pi}{\omega} \qquad \text{equ.1.18}$$

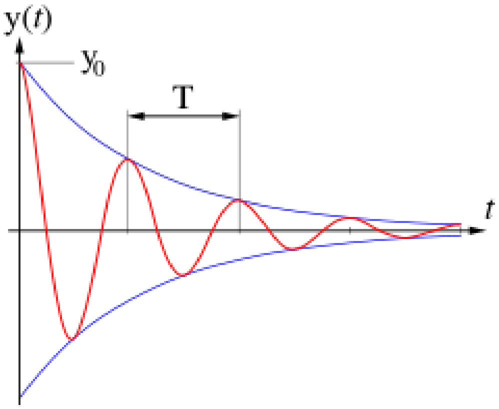

Figure 1.16 Damped oscillation mode

1.10 Power system stability controls

The power system is subjected to variations at all times. The variations can perturb the steady state stability. The feedback control reduces the effects of disturbances by keeping the outputs to the desired values. The negative feedback reduces the changes of outputs by means of altering the inputs to decrease the changes in outputs [27]. The location of eigenvalues is of importance to the stability of the system as described in the previous section. With feedback control, the pole locations can be assigned to pre-defined location assuring the stability after perturbations.

Chapter 2-Grid interconnection

2.1 Overview of power electronic grid interconnection

Each wind turbine necessarily has individual connection of the power electronic grid interconnection to support the variable speed concept. The grid interconnection converts the variable frequency and magnitude outputs from the wind turbines to the synchronous frequency of the utility grid. The grid interconnection is consisted of 2 power converters, AC-DC and DC-AC converters. The grid interconnection decouples the voltages of the generators and the utility grid. The variable frequency and magnitude output voltages from the wind turbines are converted to DC voltages or so called DC links by the AC-DC converter. The grid side inverter converts the DC link voltages to the synchronous voltages of the grid.

The ability to control the reactive power of the power electronic grid interconnection contributes to the voltage stability of the utility grid. The power electronic interface, however, produces harmonic distortions due to the switching devices of the power converters. As the technologies of power semiconductor devices grow, the higher switching frequency can be utilized to obtain a cleaner waveform. This comes with the expenses of low efficiency of the wind power caused from high switching losses of the power semiconductor devices. The promising solution of this problem is the multi-level inverter [28]. The multi-level inverter produces synthesized staircase voltages as shown in figure 2.1. Consequently, the currents and voltages at the point of common connection have lower harmonic distortions leading to a small low pass filter and high power quality. Additionally, the multi-level inverter requires $(n-1)$ capacitors for n-level voltages. As a result, each power semiconductor switch withstands only the voltage across one capacitor or $\frac{1}{(n-1)}$ of the voltage that a switch in the conventional converter has to withstand. Therefore, the multi-level inverter reduces the voltage stresses of the switching devices. Figure 2.1 shows one phase leg and voltage wave form of a multi-level inverter.

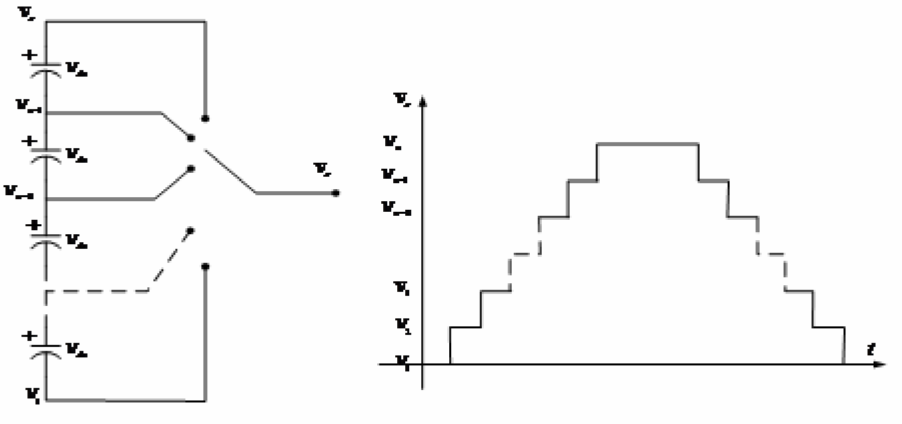

Figure 2.1 Multi-level inverter and voltage waveform

There are three types of multi-level inverter [29], [30]. The first type is a diode clamped inverter. Figure 2.2 shows one phase leg and voltage waveform of a five-level diode clamped inverter. The neutral point *n* is the reference voltage of the output phase voltage v_{an}. There are four complementary switch pairs in each phase leg. These pairs are (s_1, s_1'), (s_2, s_2'), (s_3, s_3'), and (s_4, s_4').The complementary switch pairs cannot turn on at the same time. Therefore, when s_1 is turned on, s_1' must be turned off. Table 1 summarizes the switching function of the diode clamped inverter to synthesize five-level voltages. One represents switch open whereas zero represents switch close.

Table 1 Switch combinations of diode clamped inverter

Voltage	S_1	S_2	S_3	S_4	S_1'	S_2'	S_3'	S_4'
$2V_{dc}$	1	1	1	1	0	0	0	0
V_{dc}	0	1	1	1	1	0	0	0
0	0	0	1	1	1	1	0	0
$-V_{dc}$	0	0	0	1	1	1	1	0
$-2V_{dc}$	0	0	0	0	1	1	1	1

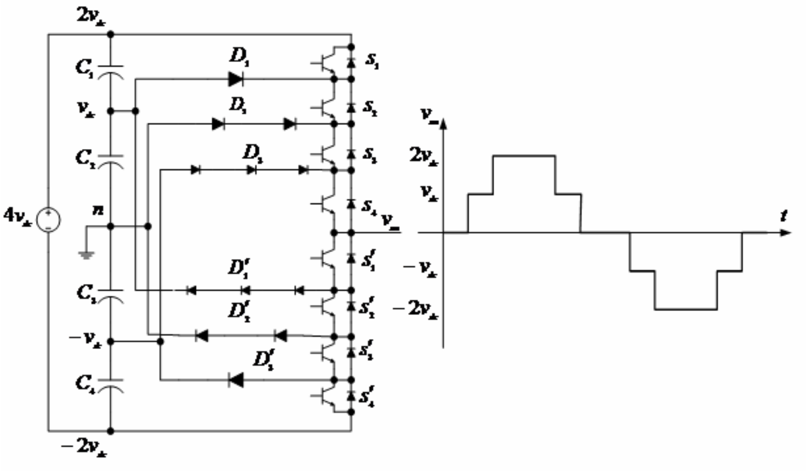

Figure 2.2 Five-level diode clamped inverter and voltage waveform

Each switching device of the diode clamped inverter blocks the voltage across one capacitor. The clamping diodes, however, block different voltages. When switch $(s_1 - s_3)$ are turned on, diode D_3 blocks voltages across capacitor$(C_1 - C_3)$. Similarly, when switch (s_3', s_4') are turned on, diode D_2' blocks voltage across capacitor(C_3, C_4). Therefore this type of inverter requires high voltage blocking capability of diodes. Alternatively, the same voltage rating of diodes as the switching devices can be used with the quadratic number of clamping diodes $(n-1)(n-2)$ for *n*-level voltages [29], [30]. For the real power transfer, it is possible that the voltage across capacitors decay unequally. This results in unbalance of capacitor voltages.

The second type of the multi-level inverter is a flying capacitor inverter. Each switching device is clamped to one capacitor voltage level. One phase leg of the flying capacitor inverter shown in figure 2.3 provides five-level voltages, which can be synthesized by the switch combinations summarized in table 2. There are three combinations to synthesize voltage V_{dc} and $-V_{dc}$ whereas there are six different combinations to synthesize the zero voltage.

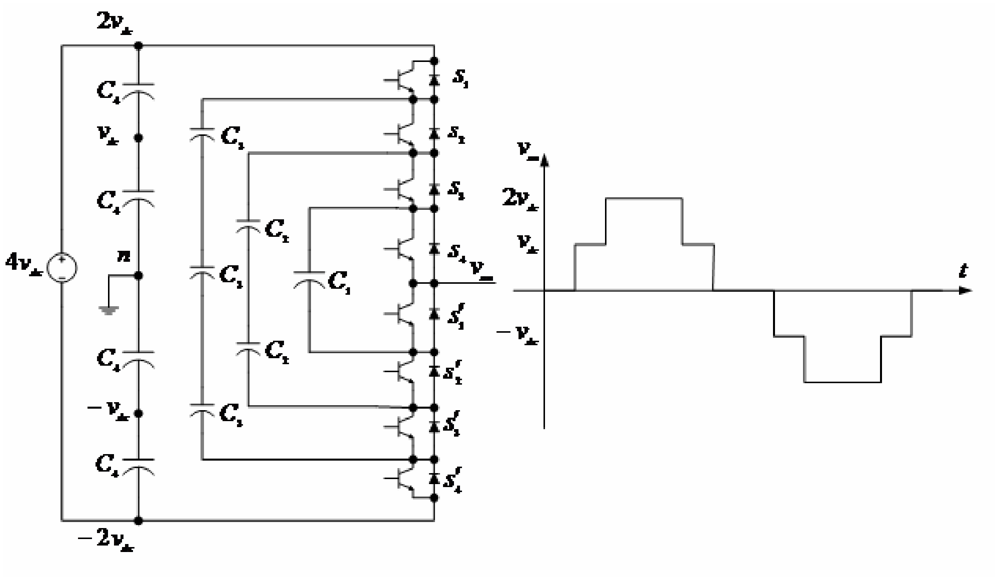

Figure 2.3 Five-level flying capacitor inverter

Table 2 Switch combinations of five-level flying capacitor inverter

Voltage	S_1	S_2	S_3	S_4	$S_1^{'}$	$S_2^{'}$	$S_3^{'}$	$S_4^{'}$
$2V_{dc}$	1	1	1	1	0	0	0	0
V_{dc}	1	1	1	0	1	0	0	0
	0	1	1	1	0	0	0	1
	1	0	1	1	0	0	1	0
0	1	1	0	0	1	1	0	0
	0	0	1	1	0	0	1	1
	1	0	1	0	1	0	1	0
	1	0	0	1	0	1	1	0
	0	1	0	1	0	1	0	1
	0	1	1	0	1	0	0	1
$-V_{dc}$	1	0	0	0	1	1	1	0
	0	0	0	1	0	1	1	1
	0	0	1	0	1	0	1	1
$-2V_{dc}$	0	0	0	0	1	1	1	1

This inverter requires a large number of bulky capacitors to clamp the voltages, similar to the diode-clamped inverter. An *n*-level inverter requires a total of *(n-1)(n-2)/2* clamping capacitors per phase leg.

The third type of the multi-level inverter is a cascaded full bridge or H-bridge inverter. The staircase waveform is synthesized by the full bridge converters connected in series. One full bridge converter produces three level voltages, which are *+Vdc, 0,* and *–Vdc.* Two cascaded full bridge converters generate five level voltages. Figure 2.4 shows seven-level voltages produced by three cascaded full bridge converters. Assume each converter has equal DC voltage.

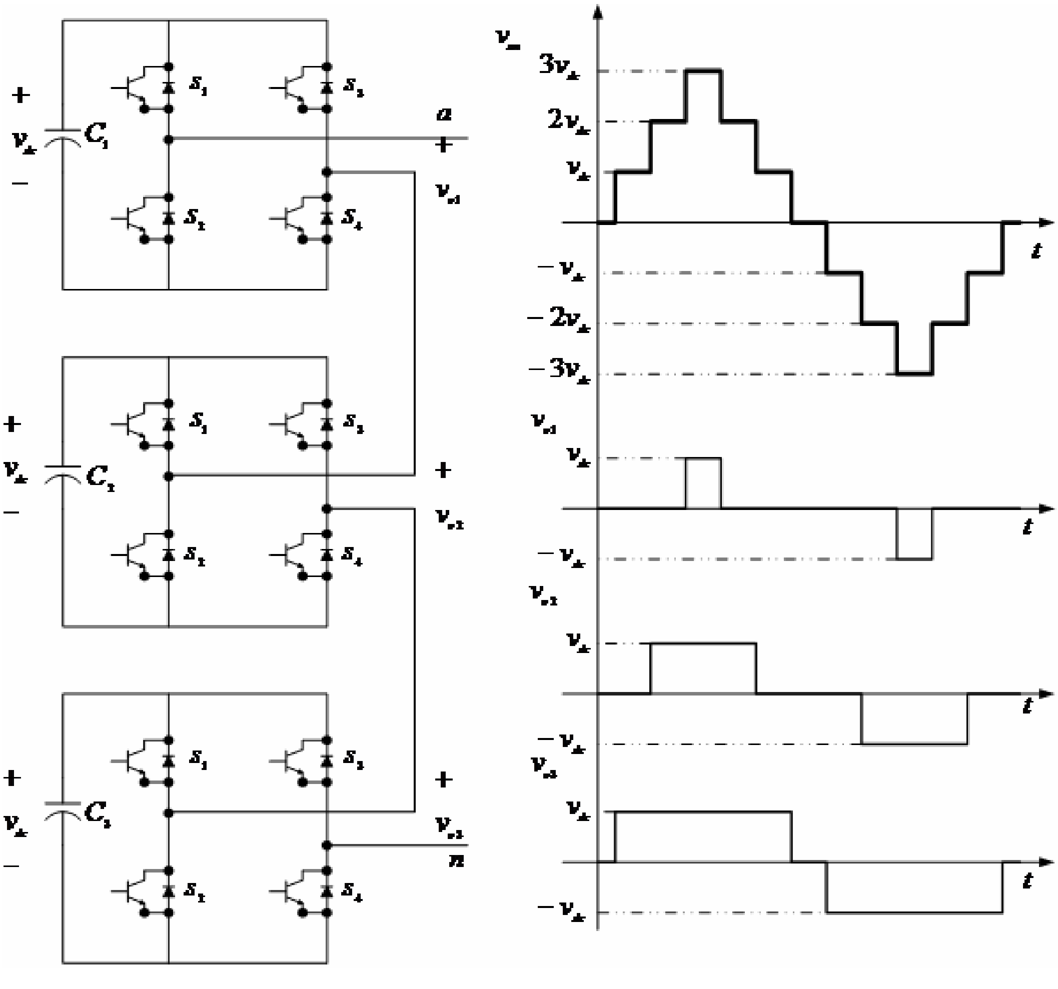

Figure 2.4 Seven-level cascaded full bridge inverter

To generalize, therefore, the cascaded full bridge inverter produces $2m+1$ level of voltages, where m is the number of cascaded full bridge converters per phase leg. The cascaded multi-level inverter requires the least numbers of components compared to the other types of the multi-level inverters. Another advantage of the cascaded multi-level inverter is its modular fashion since each unit has same structure. The disadvantage of this topology is the voltage unbalancing of the DC capacitors. [31] introduces the modification in the control scheme to balance the capacitor voltages for reactive power control with STATCOM.

The harmonic components of the synthesized stair case voltages from the multi-level inverter are comparatively low and occur at high frequencies. The stair case voltages can eliminate the low pass filter for a sufficient n-level of voltages. There are many energy storage elements in the power system. Those components can cause the resonance phenomena in the power system. This leads to an amplification of noises at a resonant frequency. Figure 2.5 shows two-level inverter and its harmonic components of the current of the utility grid with switching frequency 500Hz.

The two-level inverter has 3 phase legs for a three phase system. Each phase leg is comprised of two complimentary switches as shown in figure 2.5 (a). The two-level voltage produces voltage at 0V. and V_{dc}, which is the voltage of the capacitor. Each switching devices of the two-level inverter, therefore, has voltage stress equal to the V_{dc}. The first harmonic frequency is at the switching frequency or fs. The second harmonic frequency is at $2fs$ or two times of the switching frequency as shown in figure 2.5 (c). The current THD (Total Harmonic Distortion) is 22.57%. IEEE 519 standard [32] recommends requirements of the harmonic distortions for the electrical power system. The harmonic distortions can cause severe problems to the power system such as reduction of the current carrying capabilities of protective devices, saturations of transformers due to harmonic voltages, reduction in efficiencies of motors and generators, etc.

The switching frequency, nonetheless, can be increased resulting in reduction of harmonic distortions with higher harmonic frequencies. Consequently, the size of the low pass filter is reduced. This comes with expenses of low efficiency of the wind energy caused from the high switching losses of the power semiconductor devices.

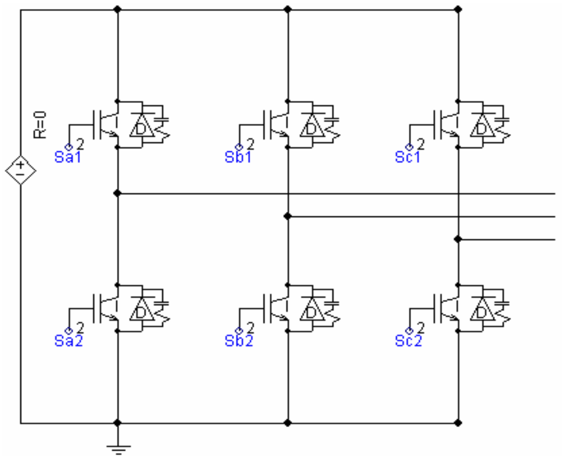

Figure2.5 (a) Two-level inverter

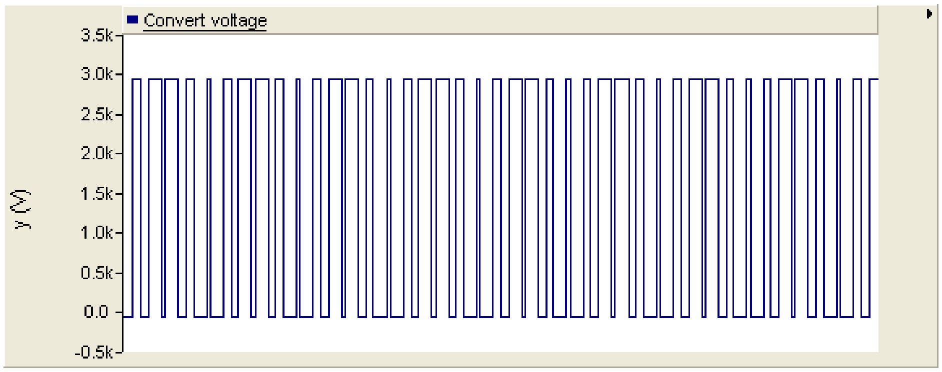

Figure 2.5 (b) Voltage waveform of two-level inverter

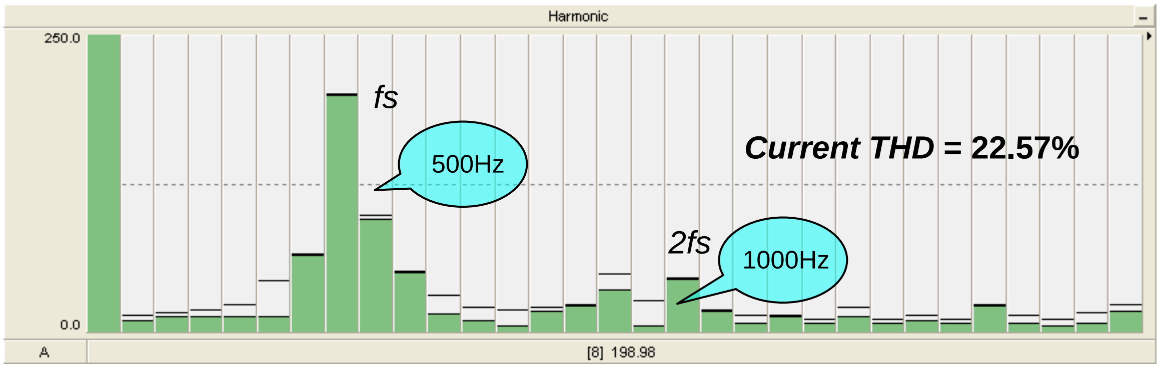

Figure 2.5 (c) Harmonic frequencies of two-level voltages

The multi-level inverter is the promising solution of the harmonic problems. Its first harmonic component is at frequency *2mfs*. The *m*-level inverter operating with switching frequency *fs* produces the first harmonic distortion at *2mfs*. Therefore, the multi-level inverter provides low total harmonic distortion with comparatively low switching loss and requires small low pass filter. Figure 2.6 and 2.7 show the voltage waveforms and harmonic distortions of the three-level and seven-level voltages, respectively. The three-level voltages are generated with one full bridge converter. The five and seven-level voltages are generated with two and three cascaded full bridge converter, respectively.

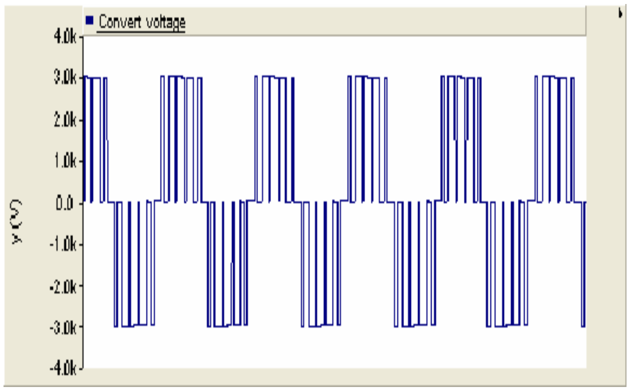

Figure 2.6 (a) Voltage waveform of three-level inverter

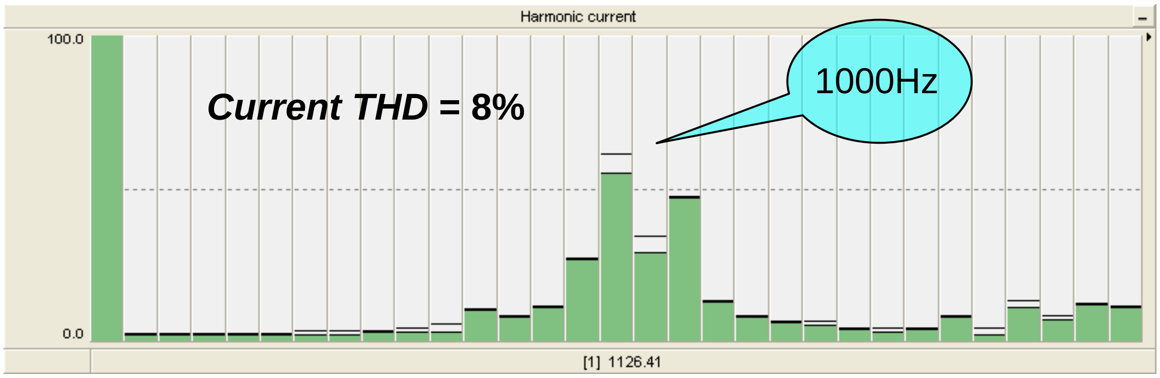

Current THD = 8%

1000Hz

Figure 2.6 (b) Harmonic frequencies of three-level voltages

As described previously, the three-level voltages are synthesized by one full bridge converter or *m* is 1. Therefore, the first harmonic component is at 1000Hz. or 2*fs*. the current THD is around 8% or 3 times lower than the two-level inverter. The harmonic distortion of the seven-level voltages is reduced to around 1.4% as shown in figure 2.7.

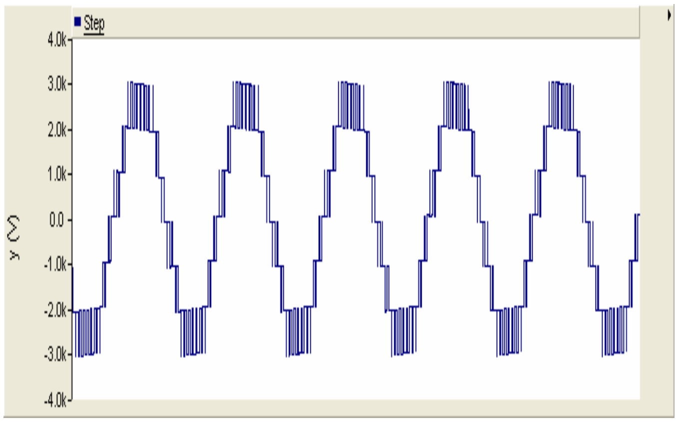

Figure 2.7 (a) Voltage waveform of seven-level inverter

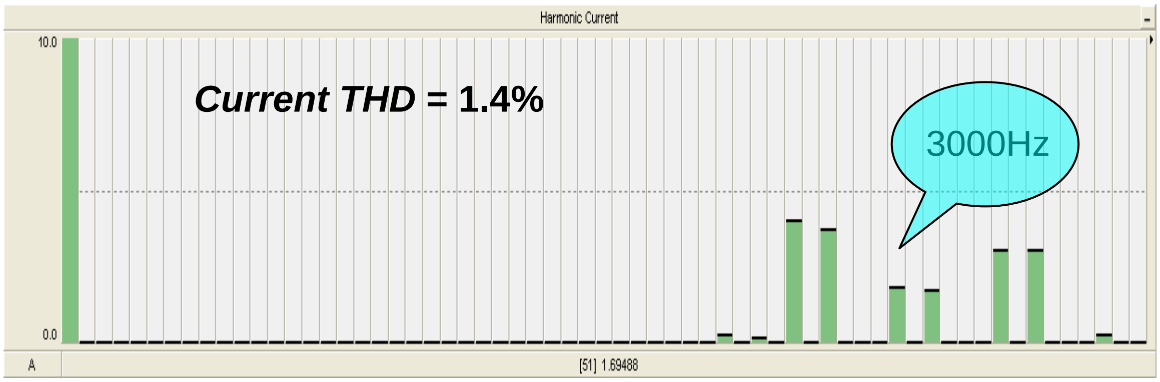

Figure 2.7 (b) Harmonic frequencies of seven-level voltages

2.2 Proposed grid interconnection

The technologies of the grid interconnection have gained a high interest in the wind industry. The grid interfaces presented in [33], [34] utilized the two-level inverter. This conventional DC-AC inverter produces high harmonic distortions at the switching frequency of the converter. The harmonic distortions exceed the limitation recommended by IEEE standard 519. The high harmonic distortions require an additional low pass filter, which is bulky. The proposed grid interconnection, as illustrated in figure 2.8, is consisted of 2 types of converters. The generator side is AC-DC converters that rectify the AC voltages from the wind turbines to the DC voltages. The grid side is the DC-AC inverter that converts the DC voltages to the AC voltages with the synchronous frequency to the utility grid. This configuration supports the concept of variable speed wind turbines by decoupling the AC voltages of generators and the grid. Therefore, the wind turbines can generate variable frequency and magnitude output voltages according to the speed of the wind. In this research, three wind turbines are used as a sample of multiple wind turbine system.

The AC-DC converter, in figure 2.8, is comprised of a three phase diode bridge rectifier as the wind turbine interface and a fly-back converter. Since the three phase diode bridge rectifier is a passive rectifier, it converts the variable AC voltages from the wind turbines without a control system. Consequently, the outputs of the three phase diode bridge rectifier are not constant but varied with fluctuations in the wind. The fly-back converters regulate and supply constant DC voltages to the multi-level inverter. There are tens to few hundreds of wind turbines connected in parallel and series in a wind farm. With isolation transformers of the fly-back converters, the wind generation system is electrically separated from the power system for safety purposes in case of the current circulation of the parallel wind turbines. The grid interface converter is the multi-level inverter, which provides low harmonic distortion currents to the utility grid to meet the IEEE 519 standard with low switching loss and voltage stress.

Figure 2.9 shows the configuration of one level of the proposed grid interconnection. The topology of the multi-level inverter is slightly different from the previous topic shown in figure 2.4. The cascaded multi-level inverter requires isolation on the DC or AC side to maintain modularity. In the previous topic, the isolation is on the DC side with separate DC capacitors. . The isolation on the DC side requires separate DC voltages for each full bridge converter. Hence it requires the increasing numbers of three phase diode bridge rectifiers and fly-back converters for high *n*-level voltages. For the proposed grid interconnection, the isolation is on the AC side with contribution of single phase transformers. The leakage inductors of the transformers behave like coupling inductors, which filter harmonic distortions. With this topology, the numbers of components can be reduced as shown in table 3 based on the seven-level cascaded full bridge inverter.

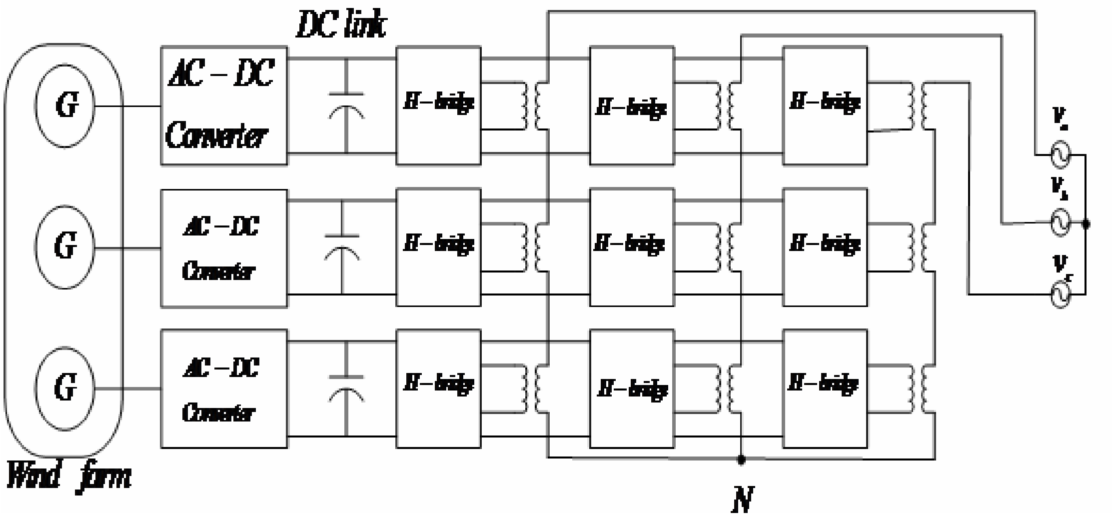

Figure 2.8 Proposed grid interconnection

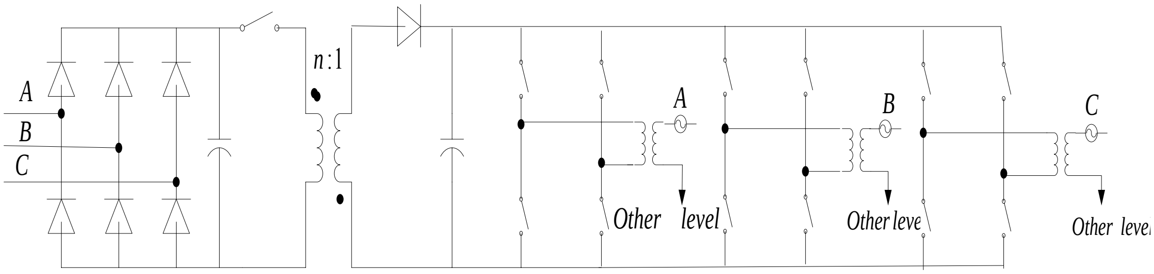

Figure 2.9 One level of proposed grid interconnection

Table 3 Components of seven-level inverter

Topology	switches	diodes	capacitors	transformers
DC isolation	45	9	9	3
AC isolation	39	3	3	12

2.3 Real and reactive power control

The proposed grid interconnection has capability to control real and reactive powers. The real power control is achieved by the phase shift between the output voltages of the grid interconnection and the voltages of the utility grid. When the voltages of the grid interconnection lead the utility grid voltages, the real power flows from the grid interconnection to the supply grid. The current and voltage of the grid are in phase as shown in figure 2.10 (a). V_c is the voltage of the grid interconnection. V_s and I_s are the voltage and current of the supply gird. When the voltages of the utility grid lead the grid interconnection voltages, the grid interconnection absorbs the real power flowing from the utility grid. The current and voltage of the grid are out of phase as shown in figure 2.10 (b).

The reactive power is controlled by the magnitude of the grid interconnection voltage. In the capacitive mode or leading current (+*Q*), output voltage of the grid interconnection is adjusted to be higher than the utility grid. The wind turbines supply the reactive power to the utility grid. In the inductive mode or lagging current (-*Q*), on the contrary, the grid interconnection absorbs the reactive power from the grid. The output voltage of the grid interconnection is less than the supply grid. Figure 2.10 c) and d) show the voltage and current waveforms of the utility grid when the pure reactive powers are transferred in the capacitive and inductive modes respectively.

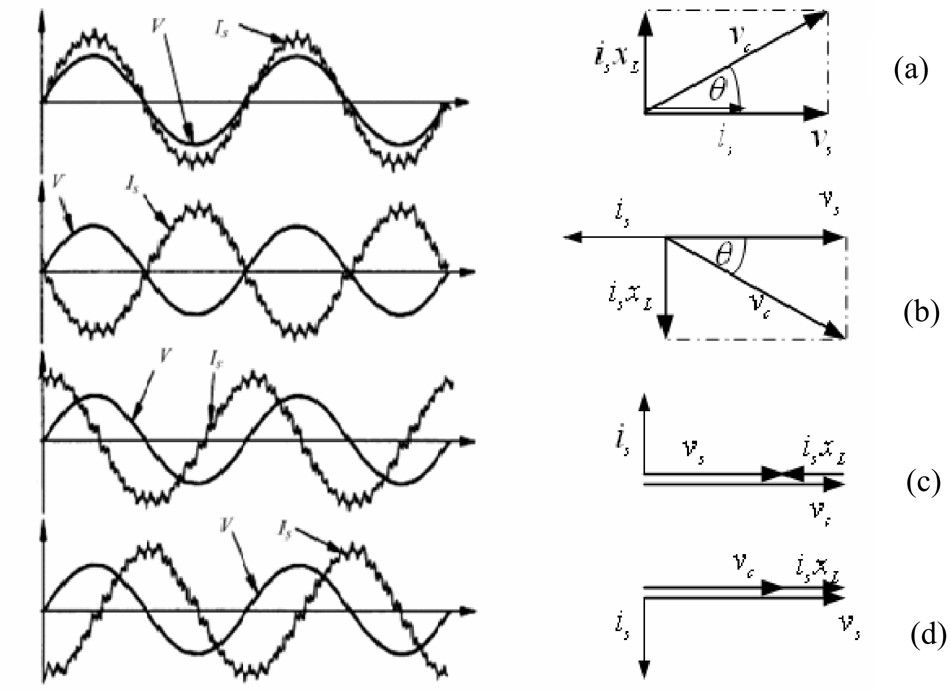

Figure 2.10 Real and reactive power transfer

In reality, the power electronic grid interconnection is not ideal and consumes real power although the wind turbines transfer only the reactive power to the power system. This results in the decay of the capacitor voltages. The fly-back converters regulate the DC link voltages enabling the real and reactive power control of the wind generation.

2.4 Configuration of the AC-DC converter in the proposed grid interconnection

A. Three phase diode bridge rectifier

The three phase diode bridge rectifier is comprised of six rectifier diodes as shown in figure 2.11. The variable frequency output voltages from wind turbines are rectified to unregulated DC voltages. One pair of diodes, one from the top group and the other one from the bottom group, conduct for one third of the input cycle for three phase system. The conduction of the diodes depends on the voltage magnitude of each phase that connects to the diodes. For example, during time interval $\left[\frac{\pi}{6},\frac{\pi}{2}\right]$, the voltage magnitude of phase A is maximum and the voltage magnitude of phase B is minimum. Therefore, diode D_1 and D_5 conduct. During time interval $\left[\frac{\pi}{2},\frac{2\pi}{3}\right]$, the voltage magnitude of phase A is maximum and the voltage magnitude of phase C is minimum. Therefore, diode D_1 and D_6 conduct. In one cycle there are six combinations of conduction of diodes, which are (D_1,D_5), (D_1,D_6), (D_2,D_6), (D_2,D_4), (D_3,D_4), (D_3,D_5), (D_3,D_5). Figure 2.12 shows the input voltages and output voltages of the three phase diode bridge rectifier. The green dashed line and blue dashed line are the positive output voltage and negative output voltage respect to the neutral point *n*. The magnitude of the output voltage respect to the neutral point is slightly less than the input voltage because of the voltage across diodes during conduction. The output voltage has six pulses in one cycle of the input voltage. Hence the three phase diode bridge rectifier is so called a six-pulse rectifier. Typically, a filter capacitor is used to smooth the output voltage.

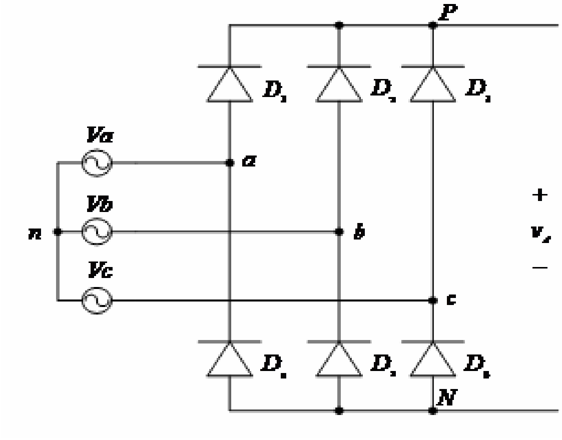

Figure 2.11 Three phase diode bridge rectifier

It is convenient to find the averaged voltage of V_d by considering only one cycle of the six-pulse voltage, during $\left[\frac{\pi}{6},\frac{\pi}{2}\right]$. Assume the three phase input voltages are sinusoidal voltages.

$$\begin{aligned} v_a &= V_m \sin(\omega t) \\ v_b &= V_m \sin(\omega t - 120^\circ) \\ v_c &= V_m \sin(\omega t - 240^\circ) \end{aligned}$$

The voltage of V_d during the time interval is

$$\sqrt{2}(V_m - 2V_{on})\sin \omega t \qquad \text{(equ.2.1)}$$

where V_m is the amplitude of the input voltage in rms.

V_{on} is the voltage drop across diode.

Therefore, the averaged voltage of V_d is [35]

$$\frac{1}{\pi/3}\int_{\pi/2}^{\pi/6} \sqrt{2}(V_m - 2V_{on})\sin \omega t \, d(\omega t) = \frac{3}{\pi}\sqrt{2}\cdot V_m \qquad \text{(equ.2.2)}$$

where V_{dm} is the peak voltage of V_d or $V_m - 2V_{on}$.

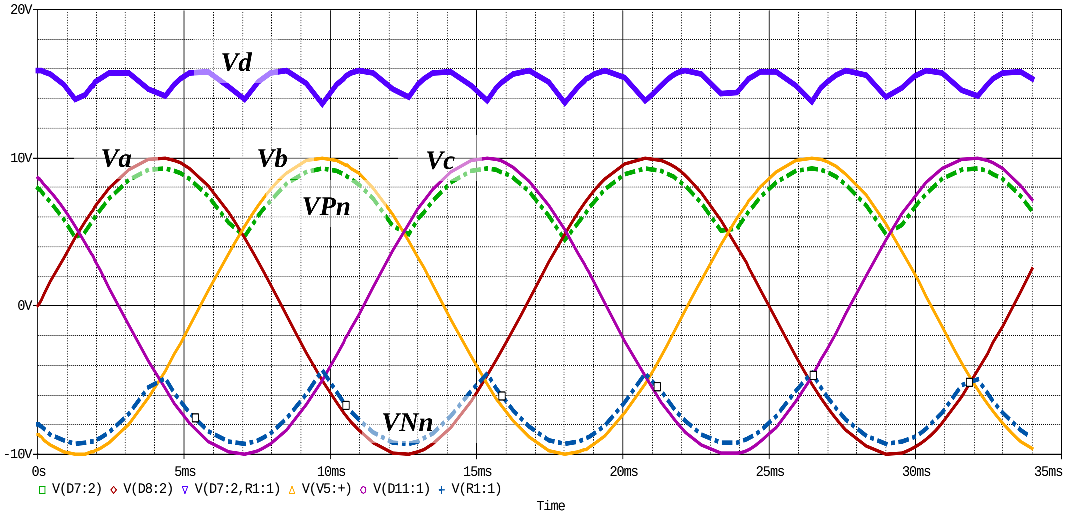

Figure 2.12 Input and output voltages of diode bridge rectifier

The unregulated output voltage of the three phase diode bridge rectifier is not sufficiently stable to supply to the multi-level inverter. Therefore, there must be an intermediate converter to supply constant DC voltages to the multi-level inverter.

B. *Fly-back converter*

The fly-back converter is used as an intermediate converter to regulate the DC voltages of the DC links. This topology eliminates the problems of unbalanced DC voltages and makes the system possible for the real power flow. The fly-back converters use single phase transformers to isolate the input and output. As a result, wind turbines and the utility grid are electronically isolated to avoid the current circulation because of the parallel connection of the wind turbines. Figure 2.13 a) shows the topology of the fly-back converter with a transformer equivalent circuit.

The single phase transformer has magnetizing inductance L_m. When transistor Q_1 turns on, magnetizing inductance is charged by the input voltage. The output voltage is regulated by the output capacitor C. Diode D_1 is reversed bias. When transistor Q_1 turns off, the current of the magnetizing inductor still flows through the primary winding of the transformer since the current of an inductor cannot change abruptly. This results in conduction of diode D_1. During this time interval, the magnetizing inductor discharges energy to the load and output capacitor. It is important to note that the DC voltage applied to the transformer must be zero in each switching period. The excessive DC voltage of transformer leads to a net increase of magnetizing current in each switching cycle and finally transformer saturation [36].

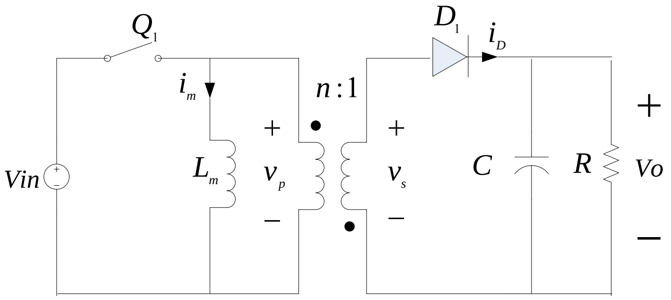

Figure 2.13 a) Fly-back converter

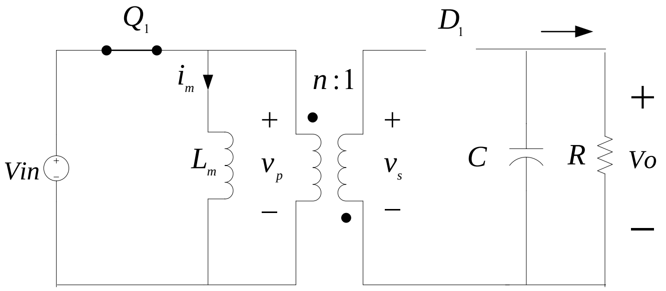

Figure 2.13 b) Fly-back converter during sub-interval 1

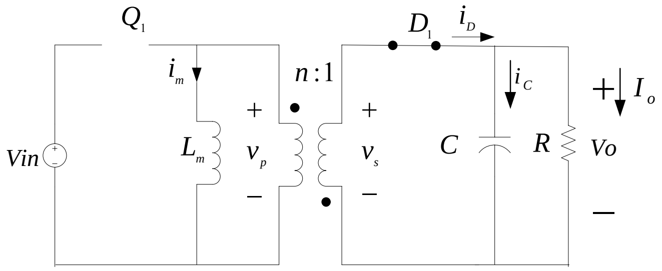

Figure 2.13 c) Fly-back converter during sub-interval 2

Figure 2.14 illustrates waveforms of the fly-back converter in continuous conduction mode. In this mode, the minimum magnetizing current of transformer is more than zero. The voltage of the primary side of the transformer (v_p) is V_{in} when transistor Q_1 turns on. When transistor Q_1 turns off, the voltage of the primary winding is nV_o, which is the output voltage transferred to the primary side.

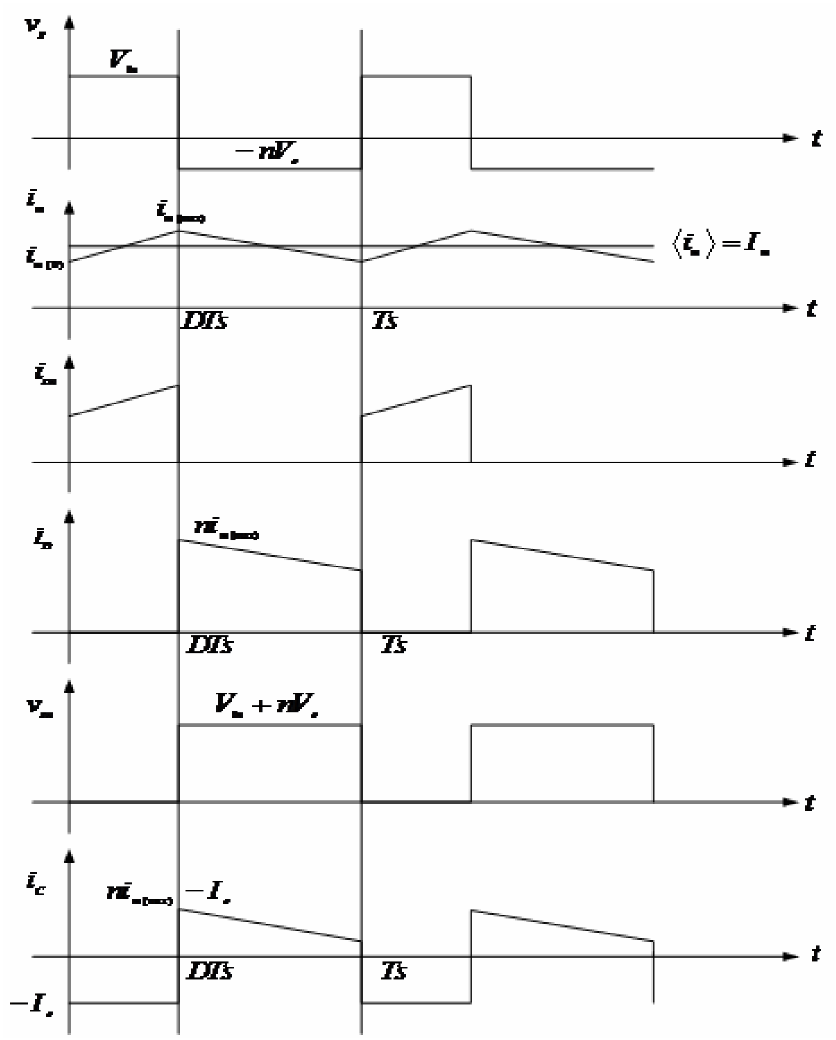

Figure 2.14 Voltage and current waveforms of fly-back converter

During the on time of the transistor Q_1, the current of the transistor Q_1 or i_{sw} is equal to the magnetizing current. The input source supplies energy to the transformer. Diode D_1 is reversed bias with voltage $-\frac{V_{in}}{n}-V_o$. The output capacitor regulates the output voltage by discharging its stored energy to the load. Therefore, during sub-interval 1, the output capacitor current is equal to the output current, $-I_o$. When transistor Q_1 turns off, the magnetizing current flows to the secondary side with transformer turn ratio n. As a result, the diode conducts. The voltage stress of the transistor Q_1 during the off-time is high. The transistor has to withstand the output voltage transferred by the transformer turn ratio n and the input voltage. When diode is forwarded bias, the transformer regulates the output voltage and transfers energy to the output capacitor. The current ripples of the magnetizing inductor depend on the input voltage, magnetizing inductance, duty cycle, and frequency as shown in equation 2.3.

$$\Delta i_L = \frac{V_{in} \cdot D}{L_m \cdot F_s} \qquad \text{(equ.2.3)}$$

where V_{in} is the averaged output voltage of generators expressed in equation 2.2

F_s is the switching frequency

T_s is the switching period = $\frac{1}{F_s}$

L_m is the magnetizing inductance

D is calculated from the volt-second balance of the magnetizing inductor

$$DT_s \cdot V_{in} + (1-D)T_s(-n \cdot V_o) = 0 \qquad \text{(equ.2.4)}$$

$$D = \frac{n \cdot V_o}{n \cdot V_o + V_{in}} \qquad \text{(equ.2.5)}$$

The voltage stress of switch Q_1 can be reduced with appropriate selection of the transformer turn ratio and duty cycle. From the volt-second balance introduced in equation 2.4, the voltage stress of Q_1 is alternatively equal to

$$V_{sw} = \frac{V_{in}}{1-D} \qquad \text{(equ.2.6)}$$

The voltage stress of Q_1 is obviously reduced with duty cycle less than 0.5. Nonetheless, the fly-back converter operates in step-down mode, which output voltage is less than input voltage, for duty cycle less than 0.5. Alternatively, the transformer turn ratio can be selected to increase the output voltage according to the equation 2.5.

2.5 Component selection of fly-back converter

The fly-back converter is based on the buck-boost converter [36] with transformer turn ratio affected on input voltage and magnetizing inductance as shown in figure 2.15. The magnetizing inductor acts as a low pass filter and energy storage element. Since the energy from the source is stored in the transformer and then passed on to the load. There are several criteria to choose the magnetizing inductance. The first criterion is the frequency of the low pass filter. The second criterion is the size of the transformer. The third criterion is the current ripples. In this dissertation, the magnetizing inductance of the transformer is chosen based on the current ripples of the transformer.

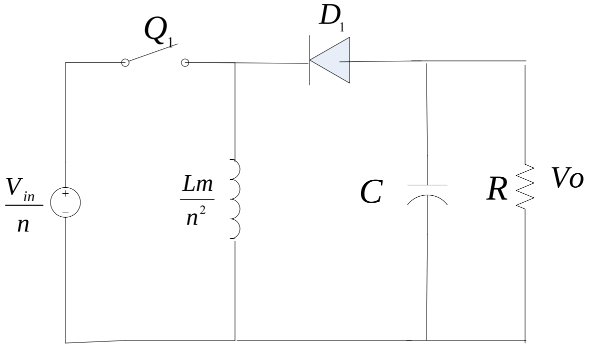

Figure 2.15 Derived buck-boost converter

Typically, the ripple current is in the range of 10-20% of the averaged current of the transformer. As illustrated in the figure 2.14, voltage across of the transformer during sub-interval 1 is the input voltage V_{in}. The averaged magnetizing current in term of the output current is found by the charge balance of output capacitor

$$-I_o \cdot DT_s + (nI_{Lm} - I_o)(1-D)T_s = 0 \qquad \text{(equ.2.7)}$$

where I_{Lm} is the magnetizing current

V_o is the output voltage of the fly-back converter

that yields

$$I_{Lm} = \frac{I_o}{n(1-D)} \qquad \text{(equ.2.8)}$$

Therefore, the magnetizing inductance that gives 10% ripple current is

$$L_m = \frac{V_{in} D T_s n}{0.1 I_{Lm}} \qquad \text{(equ2.9)}$$

The output capacitor is chosen based on the desired output voltage ripple. The output voltage ripple is in the range of 2-5% for high power quality. Since the capacitor current during the on-time of transistor Q_1 is I_o, the output capacitor is

$$C = \frac{I_o D T_s}{0.05 V_o} \qquad \text{(equ.2.10)}$$

The output current of the fly-back converter is calculated based on the assumption of ideal lossless multi-level inverter. Let P be the real power supplied or absorbed to the utility grid. This real power is the power at the output of the fly-back converter for a lossless inverter. Substituting the transformer current with the real power and eliminating the input voltage yields

$$L_m = \frac{\{V_o n(1-D)\}^2 T_s}{0.1 P} \qquad \text{(equ.2.11)}$$

$$C = \frac{P D T_s}{0.05 V_o^2} \qquad \text{(equ.2.12)}$$

2.6 Modulation scheme of multi-level inverter

It is necessary to understand the modulation scheme of a full bridge converter. Each phase leg of a full bridge converter is controlled by SPWM with separate sinusoidal control signals. The control signals are out of phase. The complimentary switches in each phase leg of a full bridge converter shown in figure 2.4 are controlled by comparing one control signal to a triangular carrier signal. The unipolar switching scheme for a full bridge converter can be summarized as follows.

Switch S_1 is on when $v_a > v_c$

Switch S_3 is on when $v_b > v_c$

Where v_a, v_b, and v_c are the control signals of phase leg a, b and the carrier signal

Figure 2.16 a) shows the unipolar switching scheme for a full bridge converter. Figure 2.16 b) and c) show the switching function of switch S_1 and S_3, respectively. The switches S_2 and S_4 are controlled complimentarily to switch S_1 and S_3. The frequency of the carrier signal determines the switching frequency of the inverter.

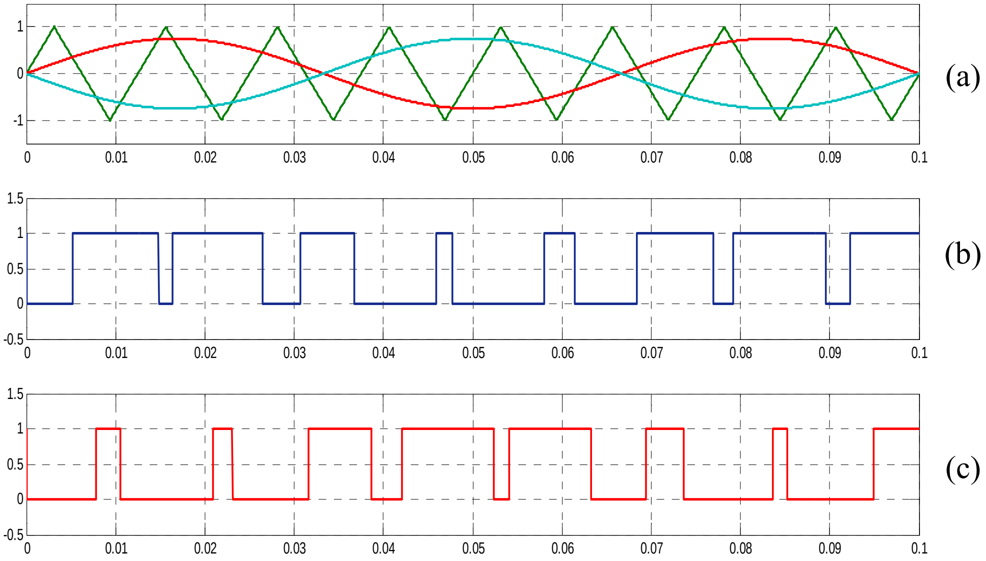

Figure 2.16 Unipolar switching scheme

There are several modulation schemes for a multi-level inverter. In this dissertation, the modulation scheme of the multi-level inverter is the PS-SPWM (Phase-shifted Sinusoidal Pulse Width Modulation) scheme [37]. For *2m+1* level of voltages with *m* numbers of cascaded full bridge converters, there are *m* number of triangular carrier waveforms with phase shift $\frac{2\pi}{m}$. Figure 2.17 a) shows a PS-SPWM of phase A for a seven-level voltage inverter with three cascaded full bridge converters. There are three triangular carrier signals for each cascaded full bridge converter. Each triangular carrier signal has phase shift 120°. Figure 2.7 b), c) and d) shows the switching function of each cascaded full bridge converters in phase A. The switching function control only switches in phase leg a. To obtain the switching function of phase leg b, there must be the other control signal, which is out of phase to that of phase leg a, as illustrated in figure 2.16.

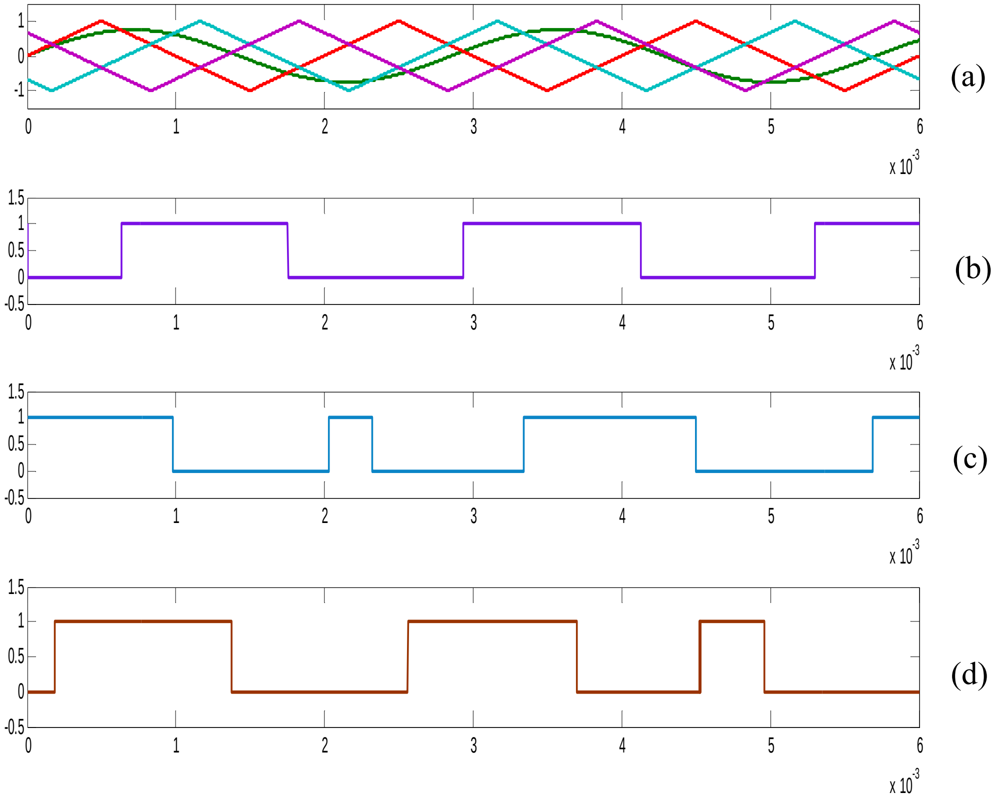

Figure 2.17 Phase-shifted sinusoidal pulse width modulation

2.7 Modeling of the power electronic grid interconnection

The purpose of modeling the grid interconnection is to design the compensator in the control system. Hence the modeling of the three phase diode bridge rectifier is avoided. The power electronic grid interconnection is considered as a SISO (Single-Input-Single-Output) system. To design the compensator, it is necessary to obtain the transfer functions of the system. The fly-back converter and the multi-level inverter are modeled separately. The modeling procedure starts with averaging the switching models of a converter with a switching operator as shown in figure 2.18. After obtaining the averaged model, the small signal model can be attained by linearizing the averaged model about its quiescent operating points. Then, apply Laplace transformation to the small signal model to obtain the transfer function.

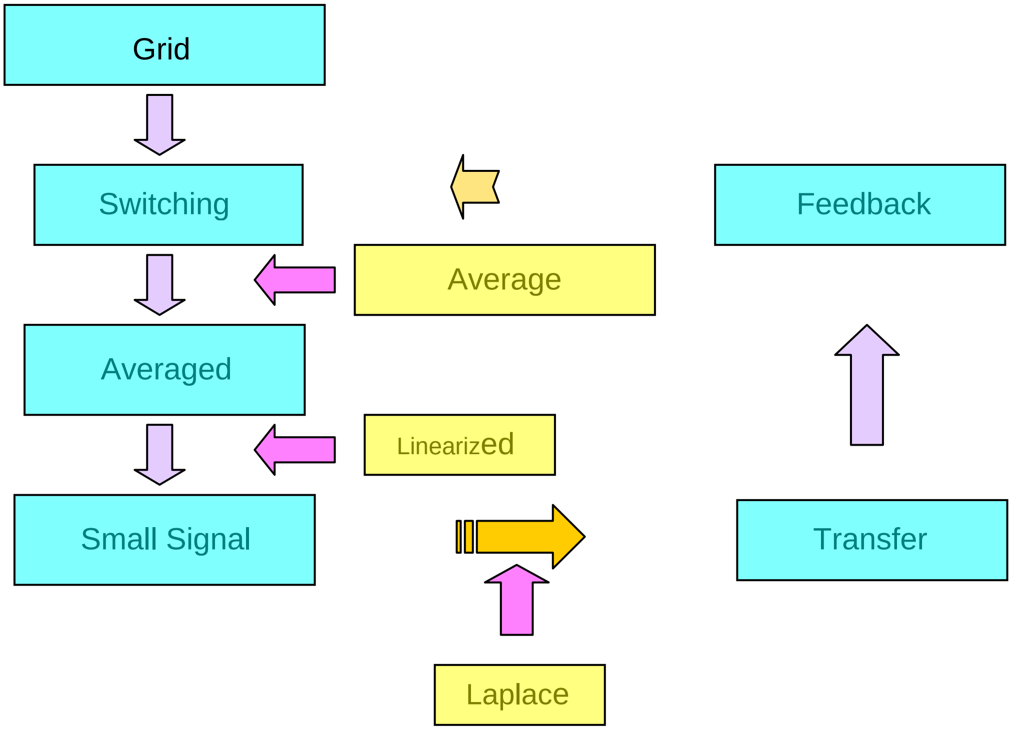

Figure 2.18 Linearized procedure

A. Fly-back converter

The non-linear switching components of the fly-back converter is averaged and modeled by the PWM switch model as introduced by Vorperian,V. [38]. The PWM switch model is a three terminal element defining the non-linear actions of power switch and diode. The terminal *c* or *common* is connected to the inductor. The terminal *a* or *active* is connected to the active or the switching device. The terminal *p* or *passive* is connected to the passive device or diode. The fly-back converter is based on a buck-boost converter as shown in figure 2.19 a).

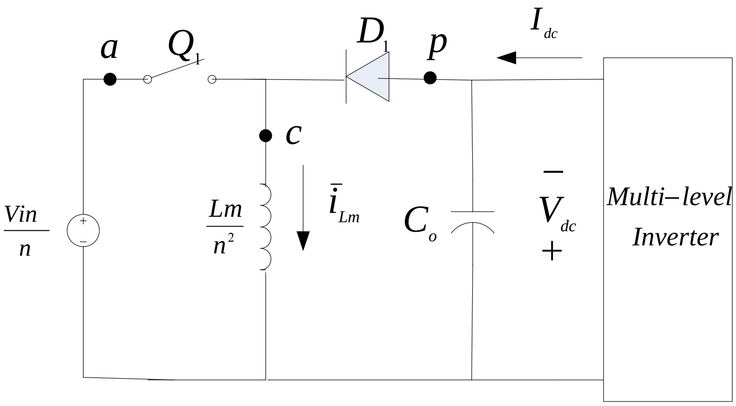

Figure 2.19 a) Derived buck-boost converter

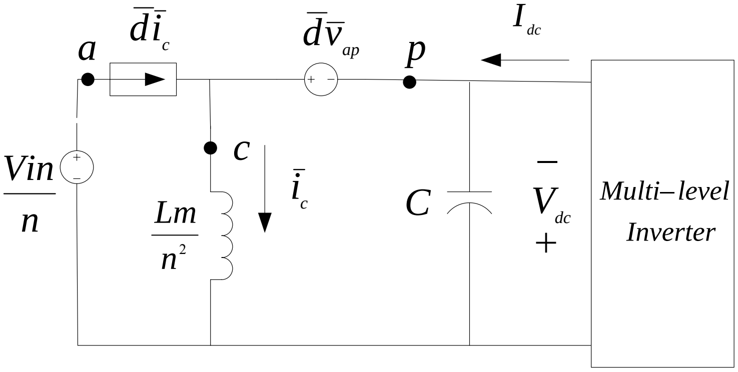

Figure 2.19 b) Averaged model

The input voltage and magnetizing inductor are transferred to the secondary side with transformer turn ratio *n*. The relationship of voltages and currents of the PWM switch can be expressed as

$$\bar{i}_a = \bar{d}\bar{i}_c \qquad \text{(equ.2.13)}$$

$$\bar{v}_{cp} = \bar{d}\bar{v}_{ap} \qquad \text{(equ.2.14)}$$

where *d* is the duty cycle. The symbol (-) denotes averaged variables.

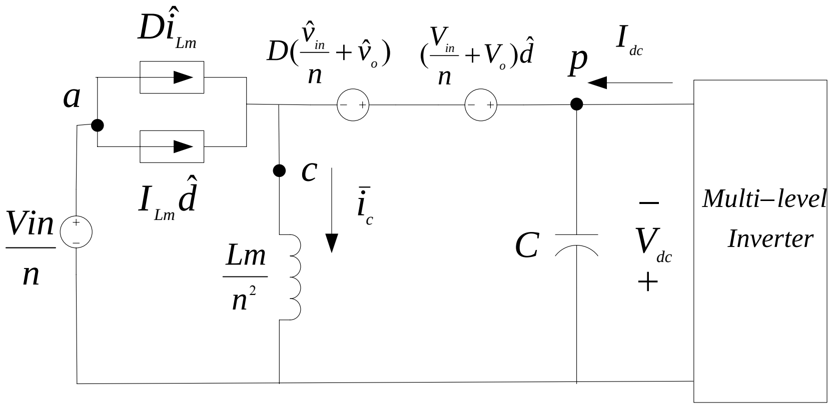

Figure 2.19 c) Small signal model

With the PWM switch model, the power switch and diode are substituted with a dependent voltage and current source as shown in figure 2.19 (b). For the fly-back converter, the variable $\bar{i}_c$ and $\bar{v}_{ap}$ are magnetizing inductor current $\bar{i}_{Lm}$ and $\bar{v}_{in}-\bar{v}_o$, respectively. Therefore, the averaged equations of the fly-back converter are

$$\frac{d\bar{i}_{Lm}}{dt}=\frac{1}{L_m}\left[\bar{d}\,\frac{\bar{v}_{in}}{n}-\bar{v}_{dc}+\bar{d}\bar{v}_{dc}\right] \qquad \text{(equ.2.15)}$$

$$\frac{d\bar{v}_{dc}}{dt}=\frac{1}{C}\left[\bar{i}_{Lm}-\bar{d}\bar{i}_{Lm}-\frac{\bar{v}_{dc}}{R_{dc}}\right] \qquad \text{(equ.2.16)}$$

where R_{dc} is the DC resistance obtained by dividing the DC output voltage with the DC output current. For an ideal lossless converter, the real power at the utility grid is equivalent to the real power at the DC link voltage. Therefore, the R_{dc} can be calculated as

$$V_dI_d=\frac{V_{dc}^2}{R_{dc}} \qquad \text{(equ.2.17)}$$

$$R_{dc}=\frac{V_{dc}^2}{V_dI_d} \qquad \text{(equ.2.18)}$$

where V_d and I_d are voltage and current of the utility grid in *D*-axis, which will be described in the next topic.

An averaged variable have two components, DC operating point and small signal variable, which can be defined as $\bar{x} = X + \hat{x}$. The capital letter represents the DC operating point of that variable. The symbol (^) denotes the small signal variable. By linearizing the averaged variables about the quiescent operating points, the small signal equations of the fly-back converter are expressed as

$$\frac{d\hat{i}_{Lm}}{dt} = \frac{n^2}{L_m}\left[\frac{1}{n}\left(V_{in}\hat{d} + D\hat{v}_{in}\right) + D\hat{v}_{dc} + V_{dc}\hat{d} - \hat{v}_{dc}\right] \qquad \text{(equ.2.19)}$$

$$\frac{d\hat{v}_{dc}}{dt} = \frac{1}{C}\left[\bar{i}_{Lm} - D\hat{i}_{Lm} - I_{Lm}\hat{d} - \frac{\hat{v}_{dc}}{R_{dc}}\right] \qquad \text{(equ.2.20)}$$

Figure 2.20 shows the averaged model of the fly-back converter in Simulink. The output voltages of the switching model and averaged model are plotted in figure 2.21. The blue line represents the output voltage from the switching model whereas the red line represents the output voltage from the averaged model. It is apparent that the output voltage of the switching model has voltage ripples due to the switching devices. The fly-back converter is simulated without a control system. The input voltage is perturbed with an increase of 5% from the operating point, which is 480Vpeak.

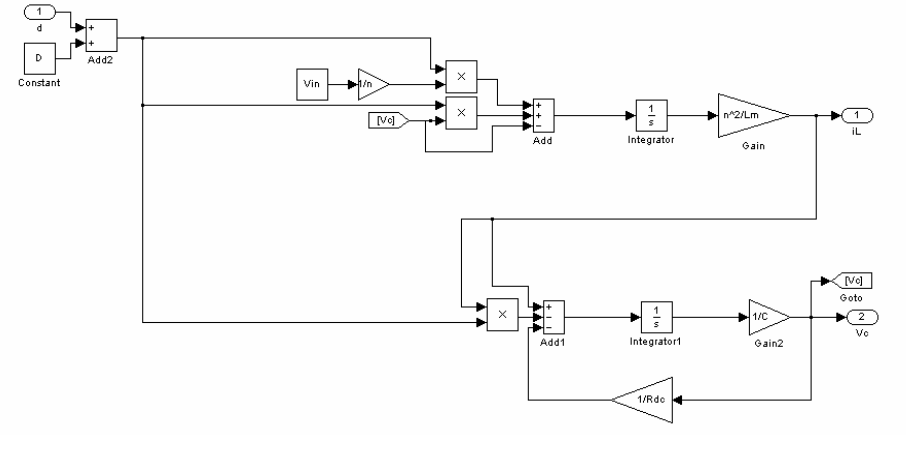

Figure 2.20 Averaged model of fly-back converter in Simulink

This results in an increase of the output voltage from 1000Volts, the nominal voltage of the DC link, to around 1020V. From figure 2.21, the averaged model provides good approximation of the fly-back converter.

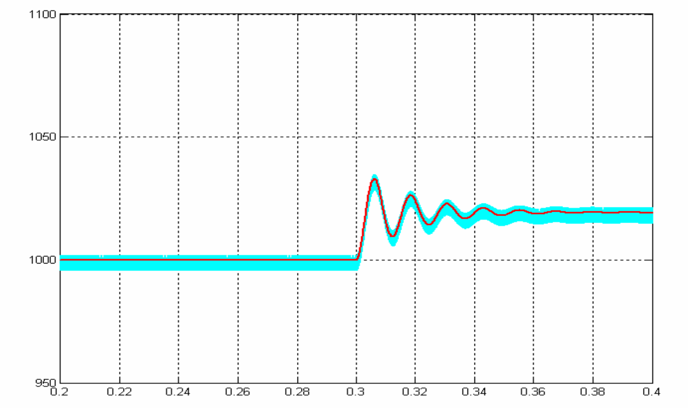

Figure 2.21 Output voltages from switching and averaged model

B. *Multi-level inverter*

The multi-level inverter in this dissertation is based on the cascaded H-bridge or full bridge converters. The complimentary switches in each phase leg of the H-bridge converter can be substituted by a SPDT (single-pole-double-throw) switch as shown in figure 2.22. The SPDT switch has two switching states. One represents the turn on of the top switch and turn off of the bottom switch. Zero represents the turn on of the bottom switch and turn off of the top switch. When the top switch turns on, the output voltage of the full bridge converter is connected to the positive polarity of the DC voltage source. When the bottom switch turns on, the output voltage of the full bridge converter is connected to the negative polarity of the DC voltage source. There are four switching combinations of a full bridge converter. Table 4 summarizes the combination of the switching functions demonstrating the relationship of voltages and currents of a full bridge converter.

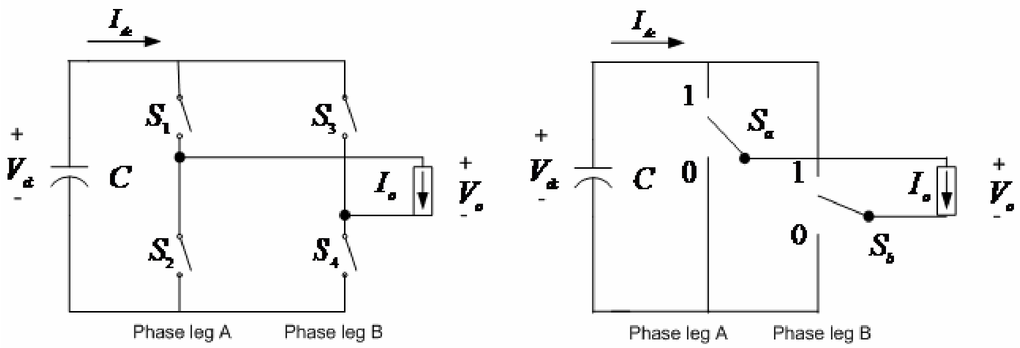

Figure 2.22 Equivalent circuit of full bridge converter

Let define the switching function S

$$S = S_a - S_b \qquad \text{(equ.2.21)}$$

Therefore, the relationship of AC and DC variables of a full bridge converter can be defined by means of the switching function as follows [31]:

$$v_0 = S \cdot V_{dc} \qquad \text{(equ.2.22)}$$

$$I_{dc} = S \cdot I_o \qquad \text{(equ.2.23)}$$

Table 4 Switching combinations of full bridge converter

S_1	S_2	S_3	S_4	S	v_o	i_{dc}
0	1	0	1	***0***	0	0
1	0	0	1	***1***	V_{dc}	I_o
0	1	1	0	***-1***	$-V_{dc}$	$-I_o$
1	0	1	0	***0***	0	0

The averaged model of the multi-level inverter is obtained by averaging the switching function in one switching period. The switching operator is

$$d = \frac{1}{T}\int_{t}^{t+T} S(\tau)\,d\tau \qquad \text{(equ.2.24)}$$

The DC voltage and the output current of a full bridge converter are assumed to be constant during a switching period. Therefore, the averaged equations of switching equations are

$$\bar{v}_0 = \frac{1}{T}\int_{t}^{t+T} S(\tau)d\tau \cdot V_{dc} = d \cdot V_{dc} \qquad \text{(equ.2.25)}$$

$$\bar{i}_{dc} = d \cdot I_o \qquad \text{(equ.2.26)}$$

Assume the DC voltages of each DC link are equal. For *2m+1* multi-level inverter with the AC isolation, the averaged equations are expressed as

$$\frac{d\bar{\vec{i}}_{abc}}{dt} = \frac{1}{3L_s}\left(\bar{\vec{D}}_{abc} \cdot \bar{V}_{dc}\right) - \frac{1}{3L_s}\bar{\vec{v}}_{abc} - \frac{R_s}{L_s}\bar{\vec{i}}_{abc} \qquad \text{(equ.2.27)}$$

$$\frac{d\bar{V}_{dc-j}}{dt} = -\frac{1}{C}\left(\bar{\vec{d}}_{abe-j} \cdot \bar{\vec{i}}_{abc}\right) - \frac{1}{C}\frac{\bar{V}_{dc-j}}{R_C} \qquad \text{(equ.2.28)}$$

Where R_C is the internal loss of the full bridge converter.

j represents the level of the full bridge converters, from 1 to *m*

i and v are the current and voltage vectors of the utility grid in phase a, b, and c as demonstrated by the equation 2.29

d_j is the duty cycle of each level of the full bridge converter

D is the summation of the duty cycles of all levels

$$\vec{i}_{abc} = \begin{bmatrix} i_a \\ i_b \\ i_c \end{bmatrix}, \vec{D}_{abc} = \begin{bmatrix} D_a \\ D_b \\ D_c \end{bmatrix}, \vec{d}_{abc-j} = \begin{bmatrix} d_{a-j} \\ d_{b-j} \\ d_{c-j} \end{bmatrix}, \vec{v}_{abc} = \begin{bmatrix} v_a \\ v_b \\ v_c \end{bmatrix}, D = d_1 + d_2 + d_3 \qquad \text{(equ.2.29)}$$

Figure 2.23 shows the averaged model of the multi-level inverter with the isolation on the AC side. The averaged model is in an ABC-coordinate. The PLL (Phase-locked loop) in the control system detects the frequency and phase of the utility grid to synchronize the control system of the multi-level inverter to the frequency of the utility grid. The detail of the control system will be fully described in the next section.

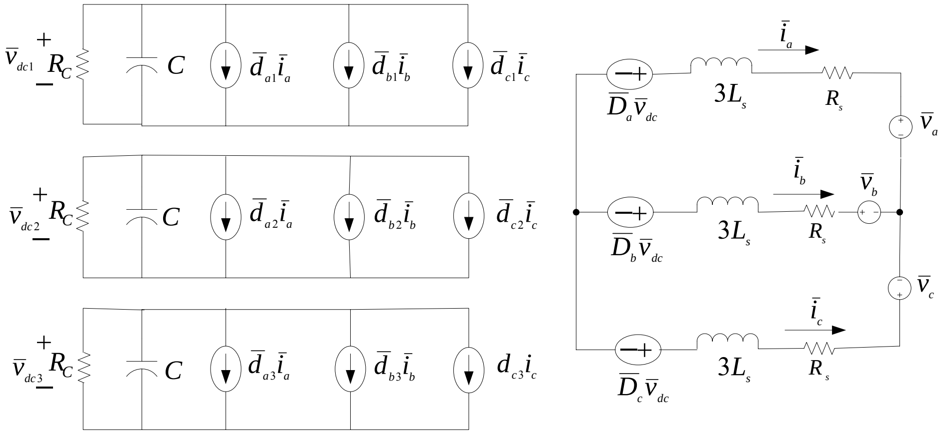

Figure 2.23 Averaged model of multi-level inverter in ABC-coordinate

Instead of the zero crossing technique that can detect the frequency two times in one period, the PLL can work faster with the technique using the quadrature of the input waveform shifted by 90° [39] as shown in figure 2.24. With this technique, voltages and currents of the utility grid are transformed from ABC-coordinate to DQ0-coordinate The DQ0-coordinate has phase shift δ to the ABC-coordinate. The advantage of transformation is that the AC variables in ABC-coordinate or so called static reference frame are changed to DC variables in DQ0-coordinate or rotating reference frame. This is because the DQ0-coordinate rotates synchronously with the frequency of the utility grid. This results in the simplicity of the real and reactive power control.

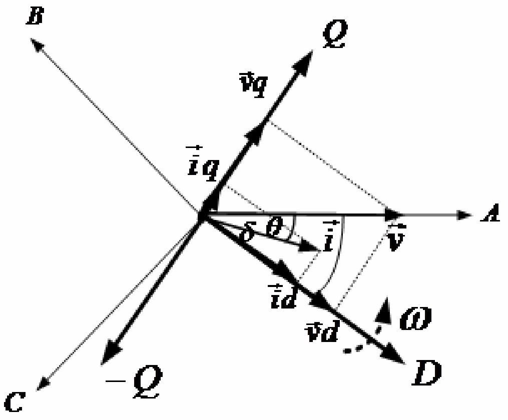

Figure 2.24 Static and rotating reference frame

The averaged model is transformed to DQ0-coordinate by Park's transformation matrix.

$$X_{dqo} = T_{dqo/abc} \cdot X_{abc} \qquad \text{(equ.2.30)}$$

$$where \quad T_{dqo/abc} = \sqrt{\frac{2}{3}} \begin{bmatrix} \cos\theta & \cos(\theta - \frac{2\pi}{3}) & \cos(\theta + \frac{2\pi}{3}) \\ -\sin\theta & -\sin(\theta - \frac{2\pi}{3}) & -\sin(\theta + \frac{2\pi}{3}) \\ \frac{1}{\sqrt{2}} & \frac{1}{\sqrt{2}} & \frac{1}{\sqrt{2}} \end{bmatrix}$$

Figure 2.25 illustrates the averaged model of the multi-level inverter in the DQ-coordinate. The 0-axis variables are neglected because of the balanced three phase system. All variables in 0-axis are zero. The averaged equations in the DQ-coordinate are described in equation 2.31 and 2.32. Matrix [W] is the coupling matrix of the currents in d- and q-axis. The coupling matrix is the byproduct of transformation from ABC-coordinate to DQ-coordinate.

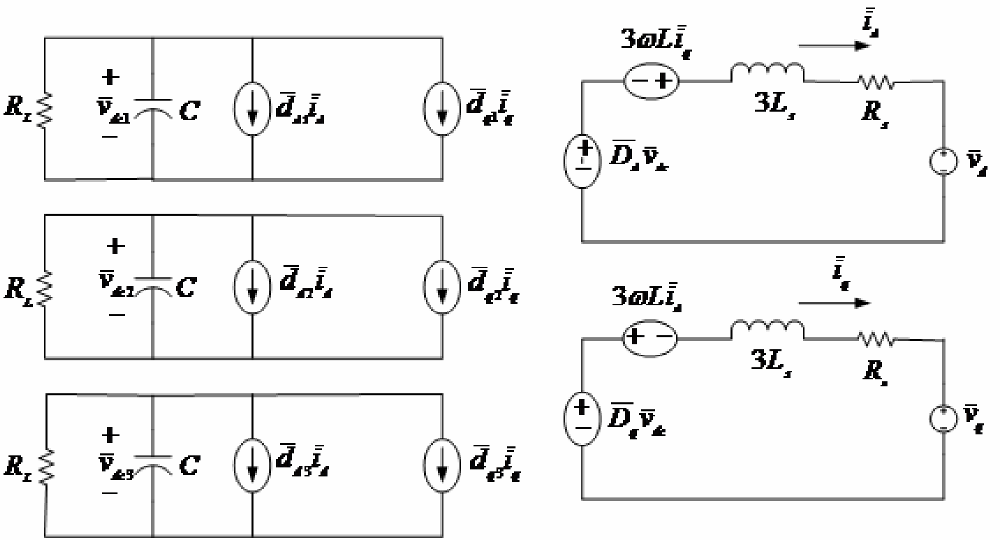

Figure 2.25 Averaged model of multi-level inverter in DQ0-coordinate

$$\frac{d\bar{\vec{i}}_{dq}}{dt} = -[W]\bar{\vec{i}}_{dq} + \frac{1}{3L_s}\left(\bar{\vec{D}}_{dq} \cdot \bar{V}_{dc}\right) - \frac{1}{3L_s}\bar{\vec{V}}_{dq} \qquad \text{(equ.2.31)}$$

$$\frac{d\overline{V}_{dc-j}}{dt} = -\frac{1}{C}\left(\overline{\vec{d}}^{T}{}_{dq-j} \cdot \overline{\vec{i}}_{dq}\right) - \frac{1}{C}\frac{\overline{V}_{dc-j}}{R_L} \qquad \text{(equ.2.32)}$$

Where $\vec{i}_{dq} = \begin{bmatrix} i_d \\ i_q \end{bmatrix}$ is the vector of currents of the utility grid in d- and q-axis

$\vec{D}_{dq} = \begin{bmatrix} D_q \\ D_q \end{bmatrix}$ is the vector of summation of duty cycles in d- and q-axis

$\vec{d}_{dq-j} = \begin{bmatrix} d_{q-j} \\ d_{q-j} \end{bmatrix}$ is the vector of duty cycles level *j* of the multi-level inverter

$\vec{v}_{dq} = \begin{bmatrix} v_d \\ v_q \end{bmatrix}$ is the voltages of the utility grid in d- and q-axis

$[W] = \begin{bmatrix} \frac{R_s}{L_s} & -\omega \\ \omega & \frac{R_s}{L_s} \end{bmatrix}$ is the coupling matrix, by product of the transformation

The small signal models of the multi-level inverter from linearizing techniques are described in the equation 2.33 and 2.34, which can be illustrated in the figure 2.26.

$$\frac{d\hat{i}_{dq}}{dt} = -[W]\hat{\vec{i}}_{dq} + \frac{V_{dc}}{3L_s}\begin{bmatrix} \hat{D}_d \\ \hat{D}_q \end{bmatrix} + \frac{1}{3L_s}\begin{bmatrix} D_d \\ D_q \end{bmatrix}\hat{V}_{dc} - \frac{1}{3L_s}\hat{\vec{V}}_{dq} \qquad \text{(equ.2.33)}$$

$$\frac{d\hat{V}_{dc-j}}{dt} = -\frac{1}{C}\begin{bmatrix} I_d & I_q \end{bmatrix}\begin{bmatrix} \hat{d}_{d-j} \\ \hat{d}_{q-j} \end{bmatrix} - \frac{1}{C}\begin{bmatrix} D_{d-j} & D_{q-j} \end{bmatrix}\begin{bmatrix} \hat{i}_d \\ \hat{i}_q \end{bmatrix} - \frac{1}{C}\frac{\hat{V}_{dc-j}}{R_L} \qquad \text{(equ.2.34)}$$

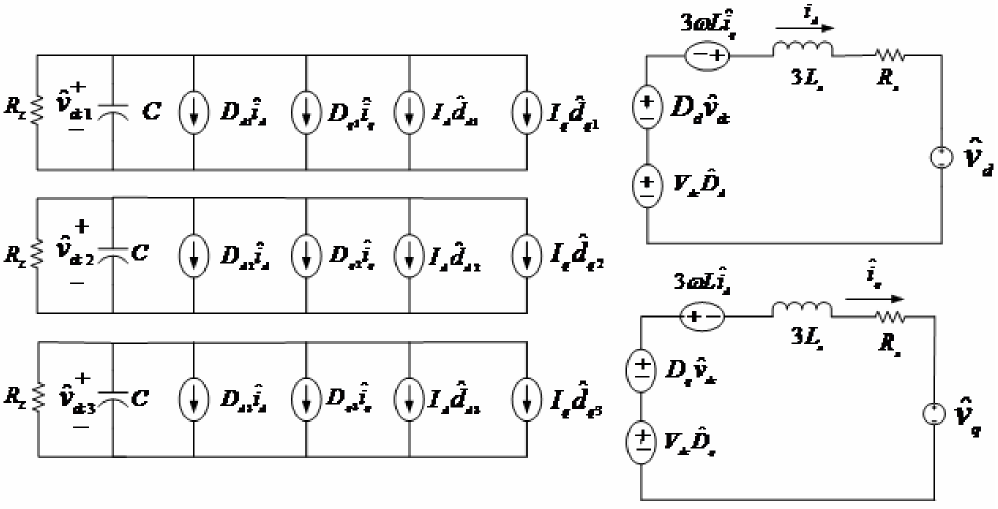

Figure 2.26 Small signal model of multi-level inverter in DQ0-coordinate

The capital letters in equation 2.33 and 2.34 denote the operating points of the multi-level inverter. V_{dc} is the voltage of the DC link. The voltages of the utility grid in phase A is expressed as

$$V_a = V_m \sin \omega t \qquad \text{(equ.2.35)}$$

For a balanced three phase system, the voltage of the utility grid in d-axis can be expressed as

$$V_d = \sqrt{1.5} \cdot V_m \qquad \text{(equ.2.36)}$$

The duty cycle in d-axis of a level *j* of the multi-level inverter is

$$d_{d-j} = \frac{V_d}{V_{dc}} \qquad \text{(equ.2.37)}$$

D_d and D_q are the summation of all levels of duty cycles in d- and q-axis. For the seven-level voltage inverter, the duty cycles can be written as

$$D_{dq} = d_{dq1} + d_{dq2} + d_{dq3} \qquad \text{(equ.2.38)}$$

I_d is the current of the utility grid in d-axis expressed as follow

$$I_d = \frac{V_{dc}}{3R \cdot d_{d-j}} \qquad \text{(equ.2.39)}$$

The transformation from ABC-coordinate to DQ-coordinate can be achieved with 0 degree phase shift (δ). This results in the alignment of the A and d-axis and perpendicular of the q-axis. Consequently, the current and voltage in q-axis are zero. The duty cycle in q-axis of a level *j* of the multi-level inverter can be expressed as

$$d_{q-j} = \frac{-3\omega L_s I_d}{V_{dc}} \qquad \text{(equ.2.40)}$$

Figure 2.27 illustrates the averaged model of the multi-level inverter with isolation on the AC side in Simulink. The duty cycle or control signal is perturbed around 5% of its operating point at 0.3 seconds. Without the control system, the real power has oscillations with a change of the steady state value from 110KWatts to 100KWatts. The reactive power experiences a high change from 0KVar to -235KVars as shown in figure 2.28. The simulation results of the switching model are illustrated in chapter 4.

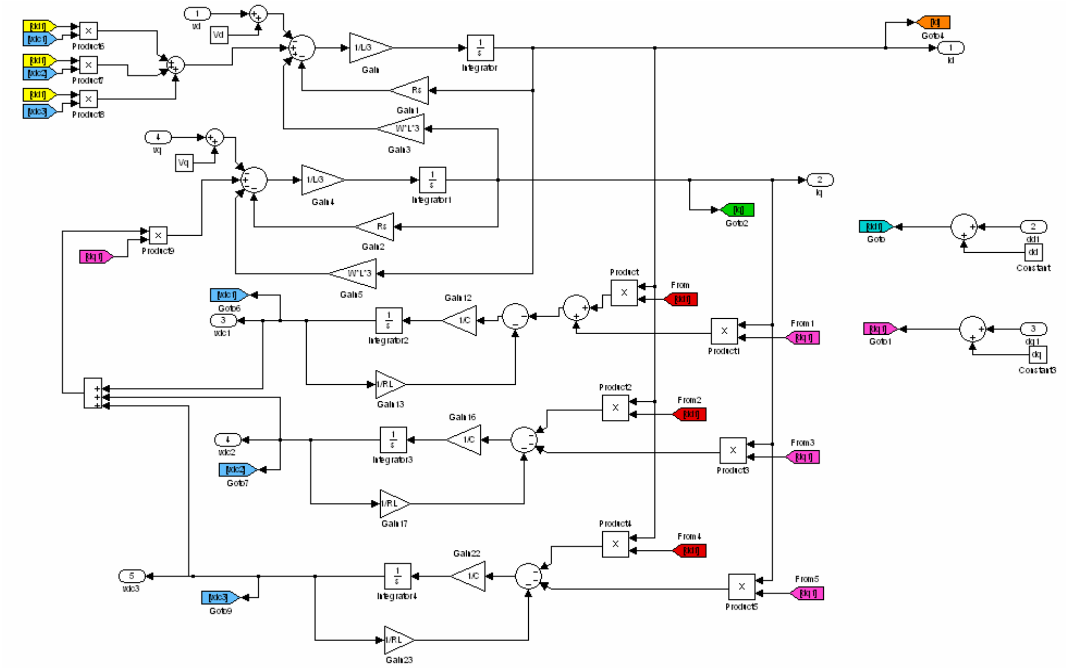

Figure 2.27 Small signal of multi-level inverter in Simulink

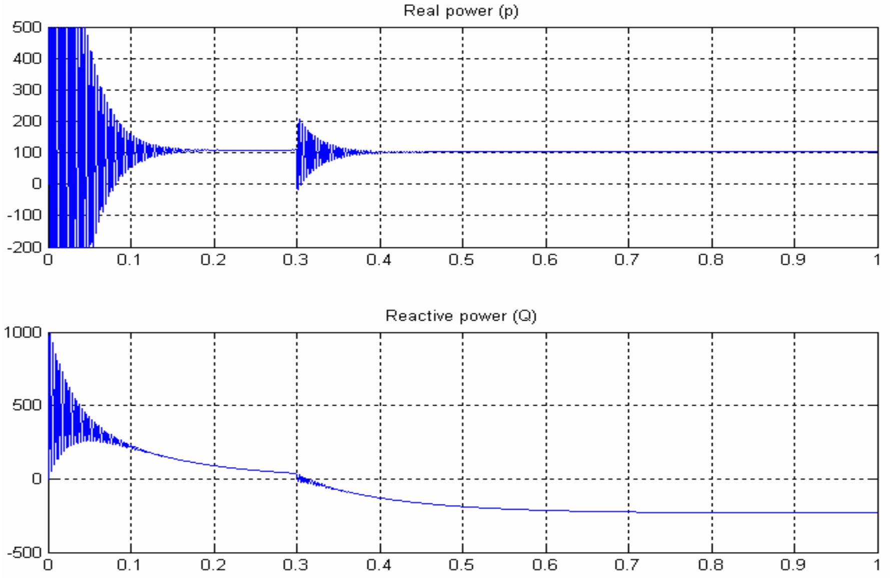

Figure 2.28 Real and reactive powers with perturbation at control signal

2.8 Control system of the grid interconnection

The control system of the grid interconnection is separated from the wind generation system. As previously described in section 1.3, the wind turbines use the pitch angle control to prevent destruction due to excess rotation speed of the rotor blades. Figure 2.29 introduces the wind generation utilized in this research. The system is simulated in PSCAD (Power Systems Computer Aided Design). The wind generation system is comprised of a wind source, wind turbine, wind governor, and wound-rotor synchronous generator. The wind source has disturbance components, which are gust, ramp, and noise components and takes external wind input. The wind turbine uses kinetic energy from the wind to turn the rotor shaft of the synchronous generator. The pitch angle of the rotor blades is controlled by the wind governor. The wind governor uses the output power from the synchronous generator as a control signal to adjust the blade angle. The wound-rotor synchronous generator with multi poles converts the mechanical energy to the electrical energy. The synchronous generator is excited by an AC exciter [40]. The AC exciter provides additional control to the generator rotor speed with the power system stabilizer (PSS) by controlling the field winding voltage.

The control systems of the fly-back converter and the multi-level inverter in the grid interconnection are separated. The purpose of the control system of the fly-back converters is to supply the constant voltages of the DC links to the multi-level inverter. The control system has two loops, voltage and current loops. Figure 2.30 shows block diagram of the control system of the fly-back converter. The voltage of the DC link is measured and compared with the desired value. The error is fed to the compensator H_v. The output of the voltage loop is acted as a reference current of the current loop. The current loop is controlled in the same manner with the compensator, H_i. Block G_v and G_i represent the open-loop transfer functions of the DC link voltage and magnetizing current.

To design the compensator, it is necessary to plot the loop gains of the voltage and current. The loop gain characteristics such as gain margin, phase margin, and cross over frequency determine the stability and transient response of the fly-back converter. The system is considered as a SISO system. The system is modeled in frequency domain with transfer functions of the relevant input and output. The gain margin, cross over frequency, and phase margin of the current loop are chosen to be 10.2 DB, 1.55KHz., and 61 degree, respectively, as shown in figure 2.31 whereas figure 2.32 shows the voltage loop gain. The gain margin, cross over frequency, and phase margin of the voltage loop are chosen to be 8 DB, 35Hz, and 97 degree, respectively.

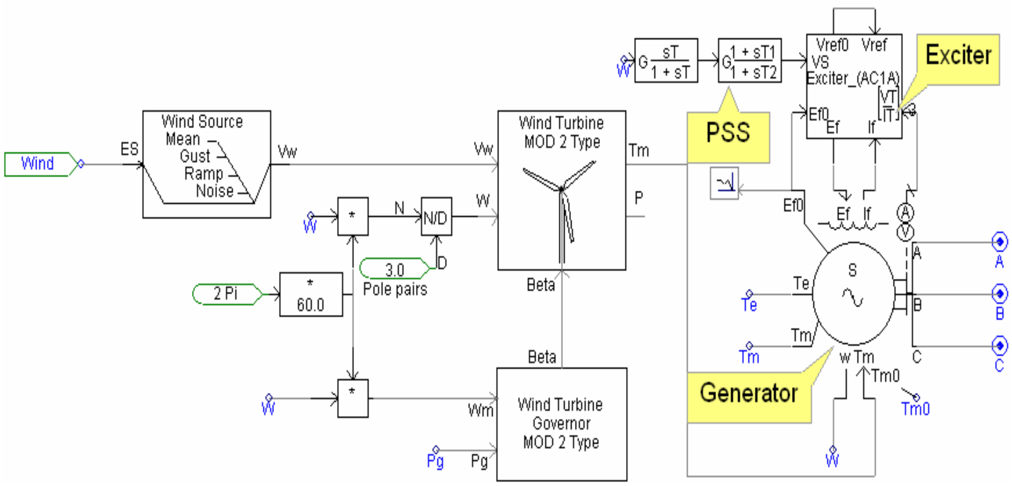

Figure 2.29 Wind generation system

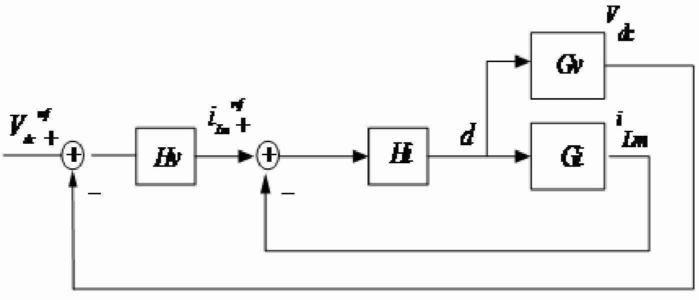

Figure 2.30 Feedback loop of fly-back converter

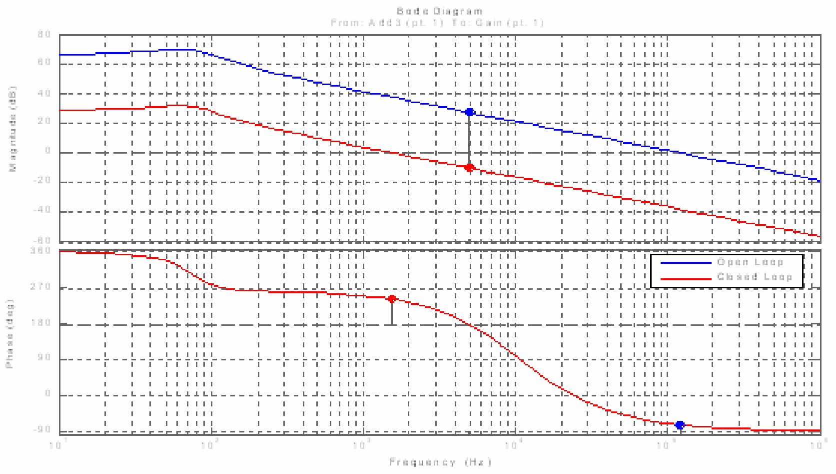

Figure 2.31 Current loop gain of fly-back converter

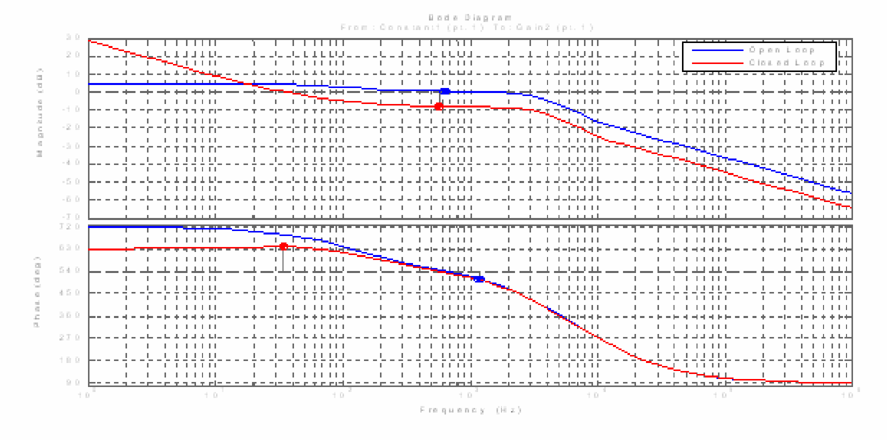

Figure 2.32 Voltage loop gain of fly-back converter

The crossover frequency of the current loop must be larger than that of the voltage loop in order to obtain full benefit of the current mode control [41]. The crossover frequency determines the bandwidth of the converter. The system that has high bandwidth responds faster than the system with low bandwidth. The current loop contributes to fast control system. The compensator of the current loop is a proportional gain, which is sufficient to compensate the error of the magnetizing current. For the voltage loop, the compensator is PI (Proportional-Integrator). Both compensators are shown below in equation 2.41 and 2.42.

$$H_i = 0.00571 \qquad \text{(equ.2.41)}$$

$$H_v = 0.5164 + \frac{153}{s} \qquad \text{(equ.2.42)}$$

Figure 2.33 shows the small signal model of the fly-back converter in Simulink. The input voltage is perturbed for 5% of its operating point at 0.3 seconds as simulated in the previous topic with the averaged model. Without the control system the voltage of the DC link increases to 1020V. The control system regulates the voltage to the nominal value at1KV as shown in figure 2.34.

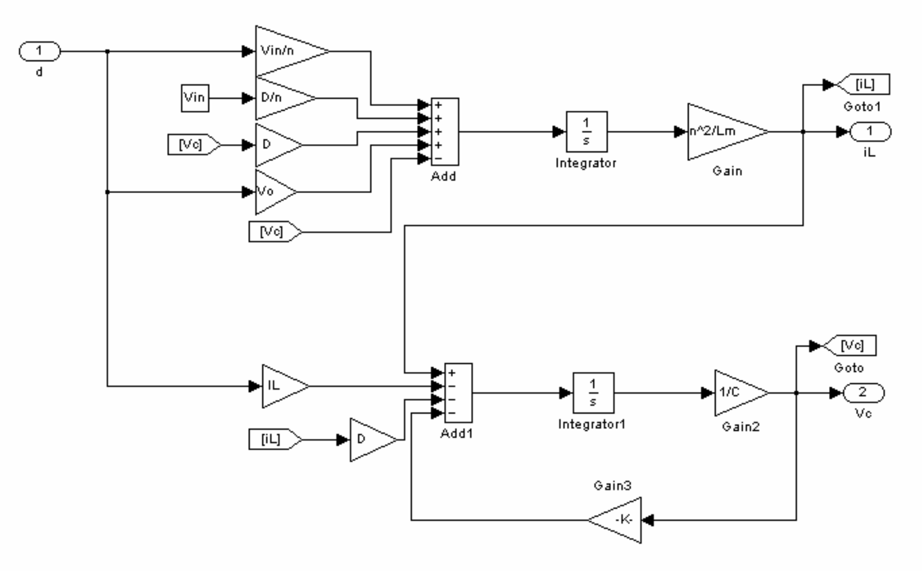

Figure 2.33 Small signal of fly-back converter in Simulink

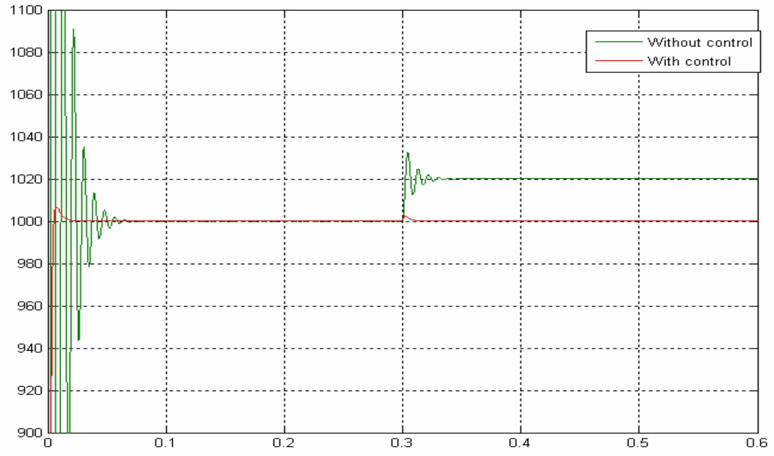

Figure 2.34 Simulation results from small signal model

The grid interconnection has two converters, the fly-back converter and multi-level inverter, connected together. The output impedance of the fly-back converter needs to be concerned. The input impedance of the multi-level inverter must be more than the output impedance of the fly-back converter to ensure stability throughout the range of the operating frequency. As seen from figure 2.35, the output impedance of the fly-back converter has low gain from 0 Hz to cross over frequency 35 Hz.

In addition to the fast transient response, the control system of the multi-level inverter in DQ-coordinate can supply or absorb real and reactive powers to the utility grid independently. The instantaneous real *(P)* and reactive powers *(Q)* in the DQ-coordinate or the synchronous rotating reference frame can be determined in equation 2.43, where V_d, I_d, and I_q are utility grid voltage and currents in the DQ-coordinate [42]. For a stable system, the real and reactive powers, therefore, can be controlled by controlling currents I_d and I_q.

$$\begin{aligned} P &= V_d \cdot I_d \\ Q &= V_d \cdot I_q \end{aligned} \qquad \text{(equ.2.43)}$$

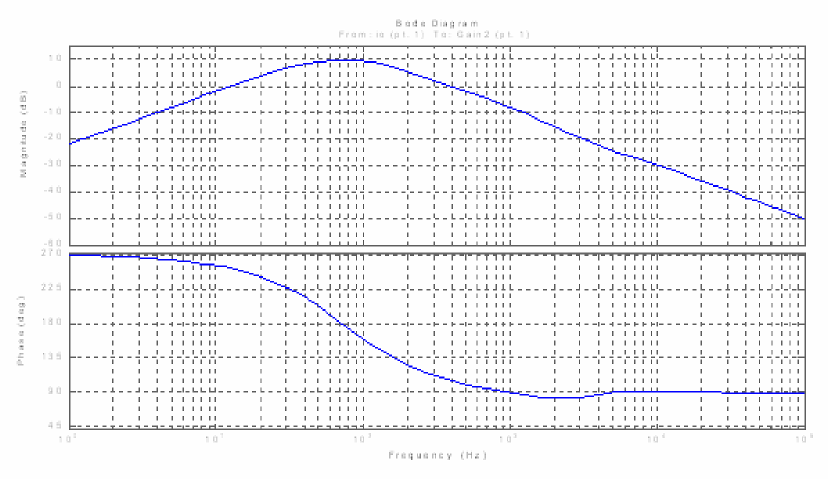

Figure 2.35 Output impedance of fly-back converter

As illustrated in figure 2.36, the voltage of the utility grid is fed to PLL (Phase-Locked Loop). The PLL provides synchronous frequency and phase to the control system. The currents of the utility grid are measured and transformed to the DQ-coordinate with Park's transformation. The grid currents are compared with the reference currents obtained from the desired real and reactive powers. The compensator H_{iq} and H_{id} keep the error close to zero. To achieve independent control of the real and reactive powers, there must be a decoupling path between the d and q-axis currents due to the coupling matrix [W] described previously. The outputs are summed with voltage of the utility grid, which is the reference of the control signals, and divided with the voltage of the DC links. The outputs are transformed back to ABC-coordinate and fed to the PWM modulation. The variables in the DQ-coordinate are transformed back to the ABC-coordinate by multiplying with the inverse Parks' transformation matrix. As demonstrated in equation 2.44, the inverse of Park's transformation matrix can be obtained by the transpose of the Park's transformation matrix.

$$X_{abc} = T_{abc/dq0} \cdot X_{dq0} \qquad \text{(equ.2.44)}$$

$$where \quad T_{abc/dq0} = T_{dq0/abc}^{\ T}$$

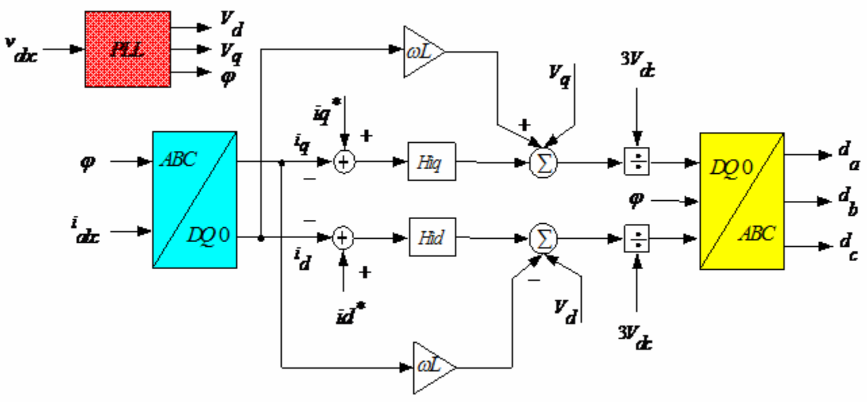

Figure 2.36 Control system of multi-level inverter

Similarly, the loop gain characteristic is used to design the current compensators, H_{iq} and H_{id}. Figure 2.37 and 2.38 show the bode plot of loop gain of the d- and q-axis currents. The cross over frequency is chosen to be around 1.5 KHz., gain margin around 10 DB, and phase margin around 60 degree for both current loops.

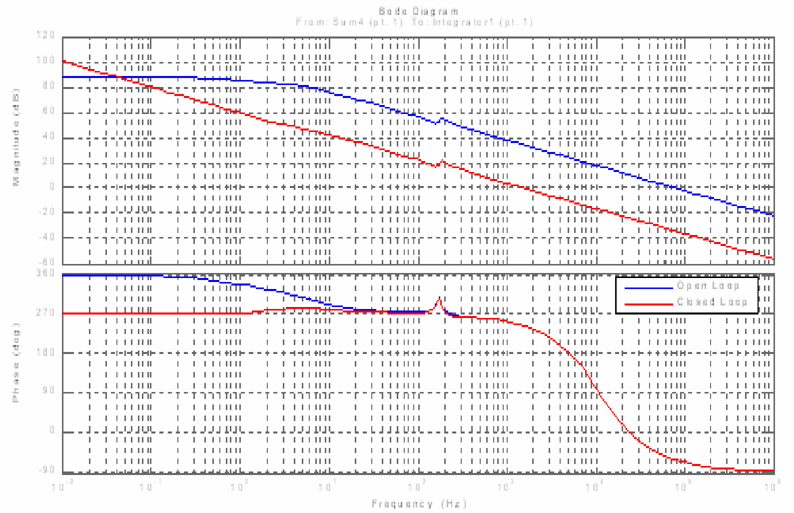

Figure 2.37 Loop gain of d-axis current

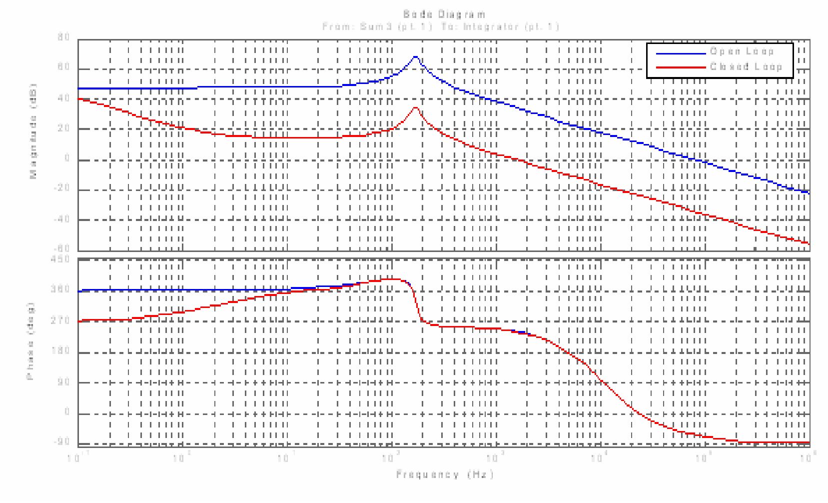

Figure 2.38 Loop gain of q-axis current

The compensator H_{iq} and H_{id} are the PI compensators. Both compensators are the same as shown in equation 2.45.

$$H_{id} = H_{iq} \quad 2+\frac{280}{s} \qquad \text{(equ.2.45)}$$

2.9 System integration

The proposed grid interconnection has two converters connected together with individual design of the control systems. Hence the interaction of the fly-back converter and the multi-level inverter must be examined to ensure the stability of integrated systems as shown in figure 2.39. The interaction between the integrated systems is analyzed by the nyquist criteria and classical control theory [43] to confirm stability of the grid interconnection.

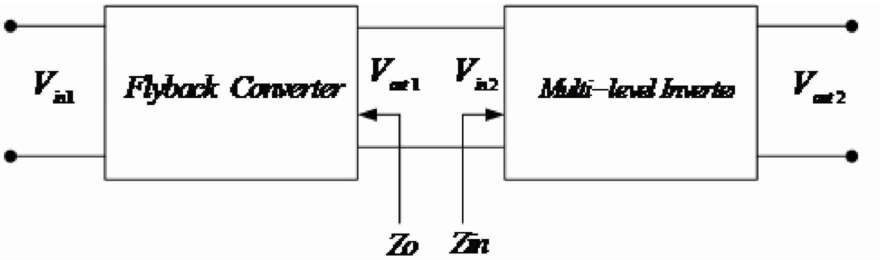

Figure 2.39 Block diagram of the grid interconnection

The overall transfer function (F) of the integrated systems can be expressed in equation 2.46 [44]-[46]. It is defined by the transfer functions of the input and output voltages of the integrated system. The overall transfer function (F) can be expressed in equation 2.46. The loading effect (T_m)is defined by the ratio of output impedance of the first converter or the fly-back converter and the input impedance of the second converter or the multi-level inverter as shown in equation 2.47.

$$F = \frac{V_{out\,2}}{V_{in\,1}} = \frac{G \cdot H}{1 + T_m} \qquad \text{(equ.2.46)}$$

$$where\ G = \frac{V_{out1}}{V_{in1}},\ H = \frac{V_{out2}}{V_{in2}}$$

$$T_m = \frac{Z_o}{Z_{in}} \qquad \text{(equ.2.47)}$$

If $Z_o<Z_{in}$ for all frequencies, there is no interaction between the subsystems. The stability of the integrated system depends on the individual subsystems. In this case, T_m is less than 1. The overall transfer function, therefore, is the product of the transfer function of each subsystem.

$$F = G \cdot H \ ; T_m << 1 \qquad \text{(equ.2.48)}$$

If $Z_o>Z_{in}$ at some frequencies, there is interaction between the subsystems. In this case, the loading effect T_m is larger than1. The overall transfer function is weighted with the loading effect, which can be expressed as

$$F = \frac{G \cdot H}{T_m} ; T_m >> 1 \qquad \text{(equ.2.49)}$$

Figure 2.40 shows the frequency response of the output impedance of the fly-back converter and the input impedance of the multi-level inverter. Between point A and B, Z_o is larger than Z_{in}. The fly-back converter and the multi-level inverter have interactions between point A and B. Hence there must be further examination of the integrated system to ensure stability.

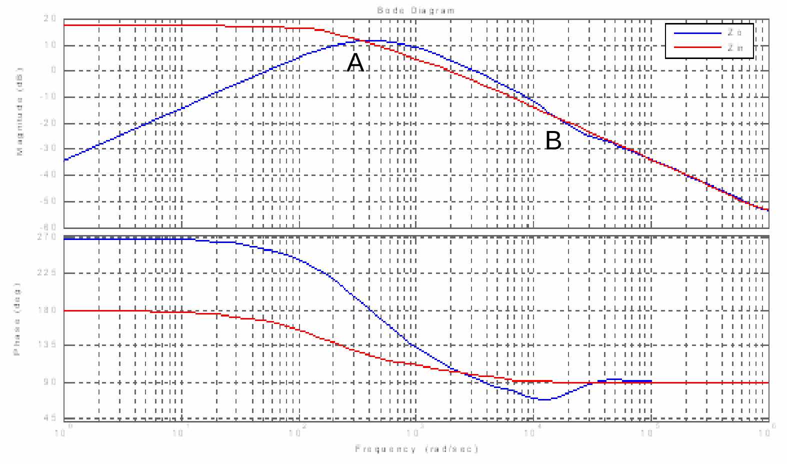

Figure 2.40 Output impedance of fly-back converter and input impedance of multi-level inverter

There are three methods to determine the stability as shown in figure 2.41, figure 2.42 and figure 2.43:

- The bode plot of T_m
- The nyquist plot of T_m
- Roots of the denominator of equation 2.45, $1+T_m$

The bode plot of T_m is shown in figure 2.41. At points A and B where the magnitude of T_m is 0DB, the phase margins of T_m are 118deg. and 162 deg., respectively. These characteristics show stability for the integrated subsystems.

The addition graphs can be plotted to guarantee the stability. Figure 2.42 shows the nyquist diagram of T_m and the pole-zero location of $1+T_m$, which has same pole location as T_m. The nyquist diagram does not encircle the (-1,0) point, with no pole and zero location on the right half plane, as shown figure 2.43. The phase margin and the nyquist diagram confirm the stability of the integrated subsystems.

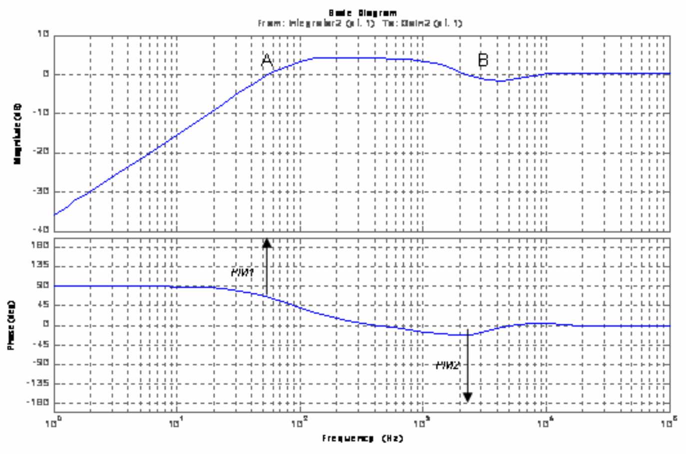

Figure 2.41 Bode plot of the loading effect T_m

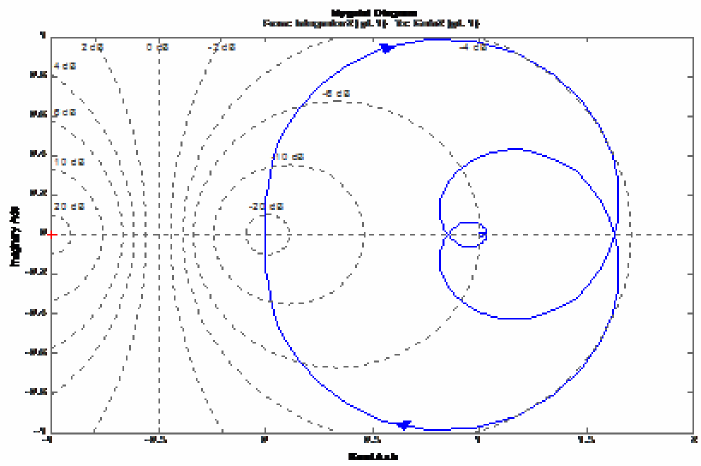

Figure 2.42 Nyquist diagram of T_m

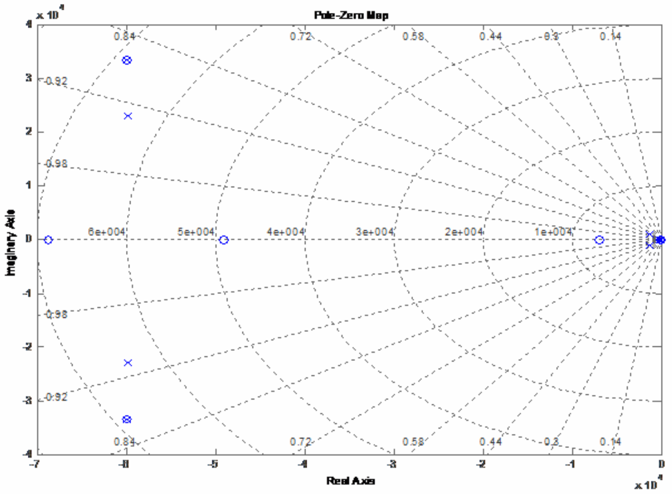

Figure 2.43 Pole-zero location of $1+T_m$

Chapter3 Dynamic modeling of a multi-machine system

3.1 Wind power

The USA was the number one in installation of the wind power in the world for three years in a row since 2006. The total capacity was around 21,017 MW in September 2008. The large capacity of the wind energy affects the power system in the context of power system stability. This chapter focuses on the dynamic modeling of an aggregated wind farm in a multi-machine system. The fluctuations in the wind have impacts on the dynamic stability of the power system. A perturbation at one machine influences the system stability.

3.2 Aggregated wind farm

Typically, a wind farm is consisted of twenty or up to a few hundreds of wind turbines. The simulation of a fully detailed model is time-consuming. The primary method is to reduce orders of the system. One method introduced in [47] is Singular Perturbation Theory involving the time scale of variables in the system. The separation of slow and fast variables contributes to fast simulation times. [48] presents the reduction technique using pole locations of variables. The high frequency poles tending to fast decay are neglected. [49] introduces a reduction method by the controllability and observability of variables in the system. The weak variables in the controllability and observability fashion are truncated. The reduced order system is then aggregated to obtain a single unit model.

The aggregation methodologies of a wind farm are different for the fixed speed and variable speed wind turbines. The input of an aggregated single unit of a constant speed wind farm is the summation of the mechanical power of each individual wind turbine. The calculation of the mechanical power is based on the different wind speed and the rotor characteristics of each wind turbine as shown in equation 1.2. For the variable speed wind farm, the electrical power of each wind turbine is summed to attain the total generated power of the wind farm [50]. [51] presents graphs of the bus voltage, active and reactive powers at the point of common connection of the fully detailed and aggregated models. The graphs show that the aggregated model is sufficient to represent the model of the variable speed wind farm.

3.3 Test system

As shown in figure 3.1, the test system has three generators, ten buses, and three loads. This system is modified from the nine-bus system introduced in [52]. Generator one and three are hydro and steam turbines, respectively. Generator two is an aggregated wind farm connected to a power electronic grid interconnection. The grid interconnection is similar to the proposed one presented in chapter 2. The difference is that the grid interconnection of the aggregated wind farm has only one level of the three phase diode bridge rectifier, fly-back converter and full bridge converter. The full detail will be described in the next section. There are three loads at bus 5, 6, and 8. Bus one is the slack bus. The detail of generators is described in table 3.1. The output of the grid interconnection, which is around 2.7KV, is stepped up by a pad-mounted transformer to the distribution level at 18KV. To interconnect the wind energy to the utility grid, a station transformer steps up the voltage to the transmission level at 230KV.

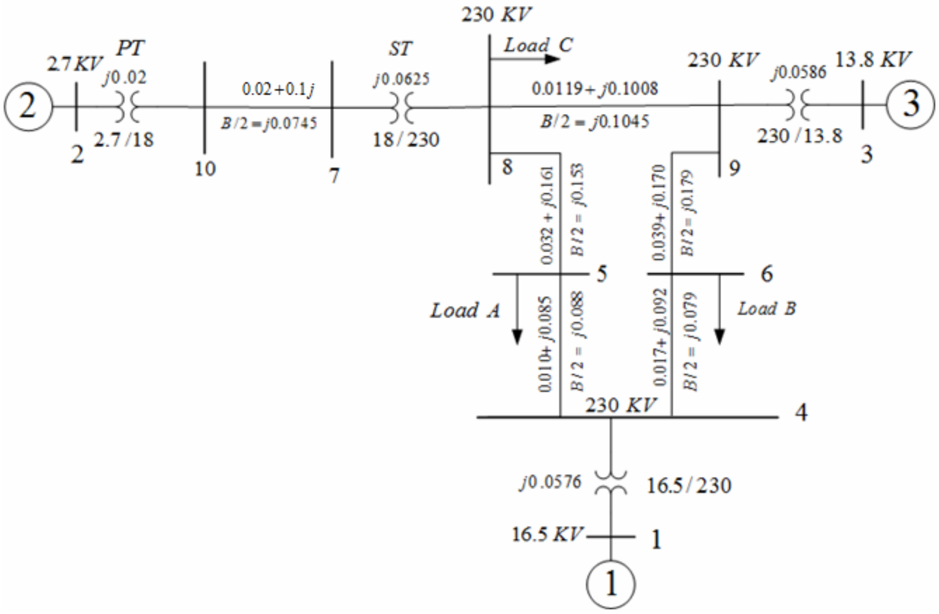

Figure 3.1 Test system

Table 3.1 Generator Data

Generator	**1**	**2**	**3**
Rated MVA	247.5	160.0	180.0
Rated KV	16.5	18.0	13.8
Power factor	1.0	0.85	0.85
Type	Hydro	Wind	Steam
$X_d^{'}$ **[pu]**	0.0608	0.1198	0.1813
$X_d - X_d^{'}$ **[pu]**	1.2852	1.27	1.1312
$T_{do}^{'}$ **[s]**	8.96	6	5.89
H(MW.s/100MVA)	6.4	H_T=2.52 H_G=18.74	6.8
K_s ***in pu***	-	0.888	-
K_D ***in pu***	1.5	0.883	2

3.4 Small signal modeling of the test system

The programming is comprised of two parts. The operating points such as voltages and powers at buses are determined by the load flow calculation. The dynamic behaviors of the system are observed by small signal modeling. The differential equations of wind turbines, generators, and power converters are linearized and arranged in the state space form. The dynamic modeling of the system is programmed in MATLAB and simulated in Simulink to ensure stability.

A. Wind turbine

The small signal of wind turbines can be categorized based on the types of generators and wind turbines [53]. As described in chapter 2, wind turbines with induction generators, both squirrel cage induction generators and doubly-fed induction generators, require a gear box to increase the low speed of the rotor blade shaft. Contrarily, the synchronous generators regardless with an excitation field circuit or a permanent magnet is a gearless system. The variable speed concept is supported by multiple poles of the generator. [54]-[56] introduce a mechanical model of wind turbines by a lumped mass model. This model uses one inertia constant (*H*) for modeling a wind turbine, gear box, and generator rotor as shown in figure 3.2. [57]-[63] utilize a two-mass model to represent wind turbines. The two-mass model separate the inertia constant of a wind turbine and generator rotor with same stiffness and damping coefficients as shown in figure 3.3. [64] and [65] introduce a three mass model. This model has three masses, which are a wind turbine, hub, and generator rotor with different stiffness and damping coefficients of low speed and high speed shafts as shown in figure 3.4.

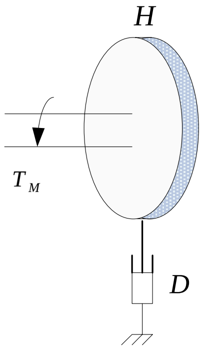

Figure 3.2 One-mass model

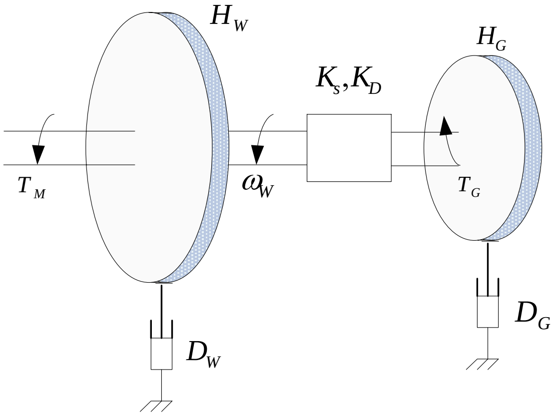

Figure 3.3 Two-mass model

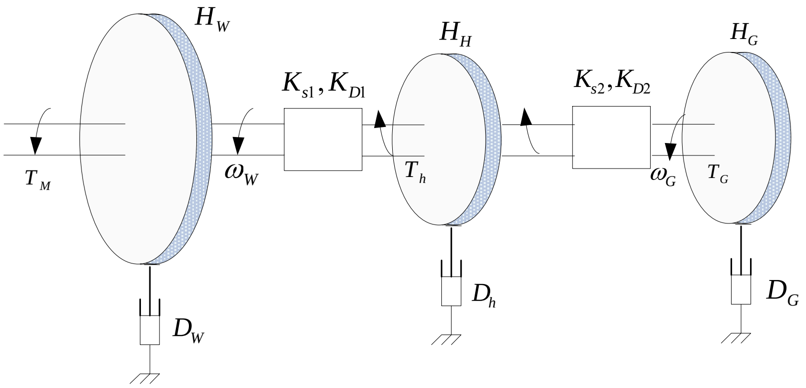

Figure 3.4 Three-mass model

This dissertation concentrates on the dynamic stability of an aggregated wind farm in the electrical power system. The two-mass model is sufficient to observe the interaction of a multi-machine system. The two mass model illustrated in figure 3.3 does not include a gear box. Figure 3.5 shows the two-mass model including a gear box. The system with a gear box is modeled in the same fashion as an equivalent circuit of a transformer. The rotational speed, torque, and moment of inertia of the rotor blade shaft and the generator rotor shaft are separated but linked with a gearbox turn ratio. Equation 3.1and 3.2 describe the relationship of those variables of the rotor blade shaft and generator rotor shaft [66].

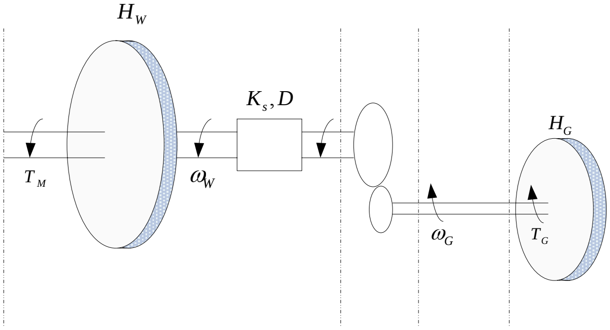

Figure 3.5 Two-mass model with gear box

$$\frac{T_W}{T_G} = \frac{\omega_G}{\omega_W} = N \qquad \text{(equa.3.1)}$$

$$\frac{H_W}{H_G} = N^2 \qquad \text{(equa3.2)}$$

In the light of the mechanical model of wind turbines, a swing equation describes the motion of rotating generator rotor. As described in 1.8, the inequality of the mechanical power and the electrical power results in acceleration or deceleration of the generator rotor. The relationship of power and torque is shown in equation 3.3

$$P = T \cdot \omega \qquad \text{(equa3.3)}$$

Where *P, T*, and ω are power, torque, and angular velocity

The power and torque can be used interchangeably since frequency variations are negligible. If the mechanical torque applied to a generator is greater than the electrical torque, the accelerating torque can be expressed as

$$J\frac{d\omega}{dt} = T_a = T_M - T_e \qquad \text{(equa.3.4)}$$

Where J is moment of inertia = $\frac{2H}{\omega_o^2} VA_{base}$

ω is the angular velocity of the machine in rad/s.

ω_o is the rated angular velocity of the machine in rad/s.

By substituting the moment of inertia, equation 3.4 can be expressed alternatively as

$$\frac{2H}{\omega_o} \cdot T_{base} \frac{d\omega}{dt} = T_M - T_e \qquad \text{(equa.3.5)}$$

Typically, the system is modeled in per unit. Therefore, equation 3.6 presents the swing equation in PU. Symbol (-) denotes per unit quantities.

$$2H\frac{d\overline{\omega}}{dt} = \overline{T}_M - \overline{T}_e \qquad \text{(equa3.6)}$$

$$\frac{d\delta}{dt} = \overline{\omega} \cdot \omega_o \qquad \text{(equa.3.7)}$$

Where δ is the rotor angle in rad

B. Synchronous generator

Figure 3.6 shows a three-phase synchronous generator [67], [68]. There are three armature windings on a-, b-, and c-axis. The rotor windings are comprised of field winding (*f*), three damper winding (*h*, *g*, and *k*). The modeling of synchronous generators can be classified based on the simplicity of the model. The differential equations of the synchronous generator depend on the number of the damper windings.

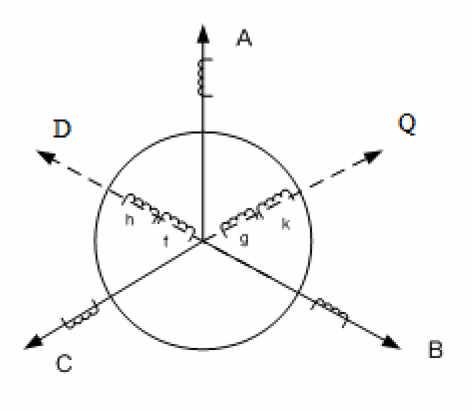

Figure 3.6 Synchronous generator

For the model with one damper winding (*g*), in addition to the swing equation described in equation 3.6 and 3.7, the system can be modeled as

$$\hat{E}_q^{'\bullet} = \frac{1}{T_{do}^{'}}\left[-\hat{E}_q^{'} + (x_d - x_d^{'})i_d + \hat{E}_{fd}^{'}\right] \qquad \text{(equa3.8)}$$

$$\hat{E}_d^{'\bullet} = \frac{1}{T_{qo}^{'}}\left[-\hat{E}_d^{'} + (x_q - x_q^{'})i_q\right] \qquad \text{(equa3.9)}$$

To simplify the model, we can neglect the damper winding *h* and *k*. By doing that, $x_q = x_q^{'}$ and $T_{qo}^{'} \neq 0$. The initial condition of equation 3.9 is $E_{do}^{'} = -(x_q - x_q^{'}) = 0$. Therefore, $E_d^{'}$ remains zero throughout the simulations as described in chapter 6 of [67]. Figure 3.7 illustrates the equivalent circuit of the synchronous generator. To include the wind turbine model, we will use the two mass model that separates the differential equations of the wind turbine and generator. The angular velocity is in per unit whereas the rotor angle is in radian. Equation 3.10 introduces small signal model of a wind turbine with synchronous generator. These equations include the gear box and multi-pole of the generator.

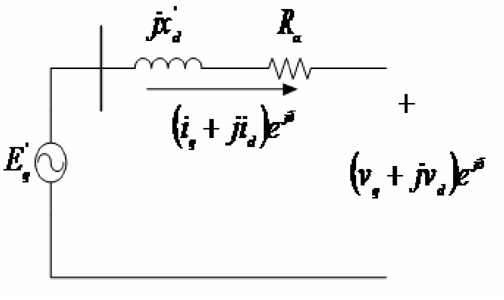

Figure 3.7 Equivalent circuit of synchronous generator

$$\hat{\bar{\omega}}_W^{\bullet} = \frac{1}{2H_W}[\hat{\bar{P}}_M - \bar{K}_s(\hat{\delta}_W^{*} - \hat{\delta}_G) - \bar{K}_D(\hat{\bar{\omega}}_W - \hat{\bar{\omega}}_G)]$$

$$\hat{\bar{\omega}}_G^{\bullet} = \frac{1}{2H_G}[\bar{K}_s(\hat{\delta}_W^{*} - \hat{\delta}_G) + \bar{K}_D(\hat{\bar{\omega}}_W - \hat{\bar{\omega}}_G) - \hat{\bar{P}}_e]$$

$$\hat{\delta}_W^{\bullet *} = \hat{\bar{\omega}}_W \cdot \frac{\omega_o}{p/2} \qquad \text{(equa.3.10)}$$

$$\hat{\delta}_G^{\bullet} = \hat{\bar{\omega}}_G \cdot \frac{\omega_o}{P/2}$$

$$\hat{E}_q^{'\bullet} = \frac{1}{T_{do}'}\left[-\hat{E}_q' + (x_d - x_d')i_d + \hat{E}_{fd}'\right]$$

Where E_q' is the internal voltage of a synchronous generator in pu

T_{do}' is the transient open-circuit time constant in pu

x_d is the synchronous reactance in pu

x_d' is the transient reactance in pu

E_{fd} is the exciter field voltage in pu

δ_W^* is the angular position of the wind turbine in electrical radian

δ_G is the angular position of the rotor in radian

ω_W is the angular velocity of wind turbine in pu

ω_G is the electrical angular velocity of the rotor in pu

P_m is the mechanical power of the rotor in pu

P_e is the electrical output power of the generator in pu

K_D is the damping coefficient in pu

K_S is the stiffness coefficient in pu

The inertia constant of the wind turbine and generator (H_W, H_G), stiffness and damping coefficients (K_S, K_D) can be defined as [66]

$$H_W = \frac{J_W \omega_o^2}{VA_{base}(P/2)^2 N^2}$$

$$H_G = \frac{J_G \omega_o^2}{VA_{base}(P/2)^2}$$

$$\overline{K}_S = \frac{K_S \omega_o}{VA_{base}(P/2)^2 N^2}$$

$$\overline{K}_D = \frac{K_D \omega_o}{VA_{base}(P/2)^2 N^2}$$

Where *P* and *N* are number of pole and gearbox ratio

With the two mass model, the angular frequency and rotor angle of the rotor blade and the generator rotor are separated as shown in equation 3.10. For the generator one and three, the rotor speed and rotor angle can be expressed as

$$\hat{\bar{\omega}}_G^{\bullet} = \frac{1}{2H_G}[\hat{\bar{P}}_m - \overline{K}_D \hat{\bar{\omega}}_G - \hat{\bar{P}}_e] \qquad \text{(equa.3.11)}$$

$$\hat{\delta}_G^{\bullet} = \hat{\bar{\omega}}_G \cdot \omega_o \qquad \text{(equa.3.12)}$$

C. Power electronic grid interconnection

The wind turbines are aggregated to an equivalent single unit as explained in section 3.2. The power electronic grid interconnection, thereby is reduced to one level. As shown in figure 3.8, the aggregated wind turbine is connected to a three-phase diode bridge rectifier, a fly-back converter, and a full bridge inverter. The multi-pole synchronous generator can operate without a gearbox.

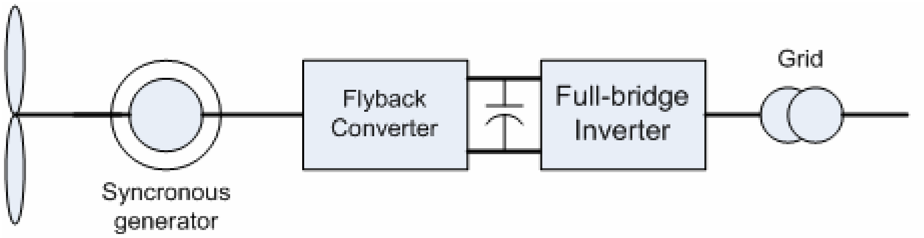

Figure 3.8 Grid interconnection

Refer to the equations of the grid interconnection in chapter two. The magnetizing current can be expressed as

$$\dot{\hat{i}}_{LM} = \frac{n^2}{L_m}\left[\frac{1}{n}\left(V_{in}\hat{d} + D\hat{v}_{in}\right) + D\hat{v}_{dc} + V_{dc}\hat{d} - \hat{v}_{dc}\right] \qquad \text{(equa3.13)}$$

Where v_{in} is the output voltage of the three phase diode bridge rectifier

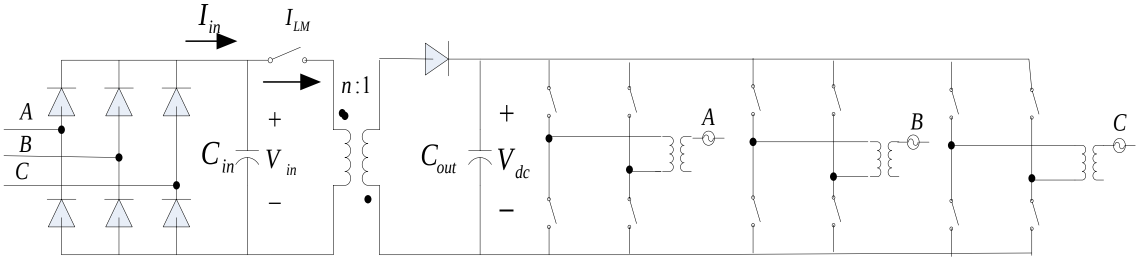

Figure 3.9 The grid interconnection of an aggregated wind farm

The relationship of the internal voltage, transient reactance, and terminal voltage of a synchronous generator, neglecting resistance R_a, can be expressed as

$$E_q^{'} = \frac{X_d^{'}}{\omega}\cdot\frac{di}{dt} + V \qquad \text{(equa.3.14)}$$

From equation 2.2, The deviation of the input voltage of the fly-back converter, $\hat{v}_{in}$, is equal to $\frac{3\sqrt{2}}{\pi}\hat{v}$. Based on the conduction of the diode, the deviation of the input current $\hat{I}_{in}$ is equal to $\sqrt{\frac{3}{2}}\hat{i}$. Assume v_{in} changes its values slowly in a short period of time, $\frac{dv_{in}}{dt} \approx 0$ . . Substitute V and I in equation 3.14 to obtain

$$\hat{E}_q^{'} \quad = \quad \sqrt{\frac{2}{3}}\frac{X_d^{'}}{\omega}\cdot\frac{d\hat{i}_{LM}}{dt}+\frac{\pi}{3\sqrt{2}}\hat{v}_{in}$$

Arranging the above equation yields

$$\hat{v}_{in} \quad = \quad \frac{3\sqrt{2}}{\pi}\left(\hat{E}_q^{'}-\sqrt{\frac{2}{3}}\frac{X_d^{'}}{\omega}\cdot\frac{d\hat{i}_{LM}}{dt}\right) \qquad \text{(equa.3.15)}$$

Substituting equation 3.15 into equation 3.13, the magnetizing current is expressed as

$$\hat{i}_{LM}^{\bullet} = K\cdot\frac{n^2}{L_m}\left[\frac{1}{n}V_{in}\hat{d}+\frac{3\sqrt{2}D}{n\pi}E_q^{'}+D\hat{v}_{dc}+V_{dc}\hat{d}-\hat{v}_{dc}\right] \qquad \text{(equa.3.16)}$$

Where $K = (1+\frac{2\sqrt{3}}{\pi}\frac{nD}{L_M}\cdot\frac{X_d^{'}}{\omega})$

The fly back converter is connected to a full bridge converter. The DC link voltage applied from equation 2.20 can be demonstrated as

$$\hat{v}_{dc}^{\bullet} = \frac{1}{C_o}\left[\bar{i}_{Lm}-D\hat{i}_{Lm}-I_{Lm}\hat{d}-D_d\hat{i}_d-I_d\hat{d}_d-D_q\hat{i}_q-I_q\hat{d}_q\right] \qquad \text{(equa.3.17)}$$

Where D_d, D_q are the control signals of the full bridge inverter in d- and q-axis at the steady state

The small signal model of the full bridge converter is similar to the multi-level inverter presented in chapter 2. Nonetheless, the factor 3 disappears because there is only one full bridge converter per phase.

$$\hat{i}_d^{\bullet} = -\frac{R_s}{L_s}\hat{i}_d+\omega\hat{i}_q+\frac{V_{dc}}{L_s}\hat{d}_d+\frac{D_d}{L_s}\hat{V}_{dc}-\frac{1}{L_s}\hat{V}_d \qquad \text{(equa.3.18)}$$

$$\hat{i}_q^{\bullet} = -\frac{R_s}{L_s}\hat{i}_q-\omega\hat{i}_d+\frac{V_{dc}}{L_s}\hat{d}_q+\frac{D_q}{L_s}\hat{V}_{dc}-\frac{1}{L_s}\hat{V}_q \qquad \text{(equa.3.19)}$$

Where R_s is the DC loss of the filter inductor

The grid interconnection is modeled by equation 3.16 - 3.19. The operating points of the grid interconnection are now different from the previous chapter. For a multi-machine system, the operating points are dependent on the power flow of the power system, which will be described in the next section.

3.5 Operating points

A. Test system

There are several methods to find the power flow. The method used in this dissertation is Newton-Raphson power flow [Appendix B]. Figure 3.10 shows the flow chart of the program. The right column is the programming files in MATLAB. The program starts from creating an admittance matrix of the test system. Table 3.2 gives the complex powers of generators and loads whereas the impedance and admittance of the system are summarized in table 3.3. The complex powers of bus one are skipped since bus one is the slack bus.

Program "Parameter_Test system1" creates the admittance matrix. The admittance matrix is symmetrical and has 10×10 elements for a 10 bus system. The diagonal elements *i* contain the summation of all admittances connected to bus *i* whereas the off-diagonal elements *j* of row *i* contain the admittance between bus *i* and bus *j* in the opposite polarity. The admittance can be expressed as

$$Y_{ii} = \sum_{k=1}^{m} y_{ik}$$

$$Y_{ij} = Y_{ji} = -y_{ij}$$

To include the grid interconnection in the power flow, we will use a regulating transformer to control the real and reactive powers of the wind park as shown in figure 3.11. We will develop one bus, bus 11, between bus 2 and the pad-mounted transformer to support the connection of the regulating transformer. The transformer turn ratio *t* is chosen to be 2% for good power control.

Table 3.2 Complex powers of generators and loads of the test system

	Gen 1	**Gen 2**	**Gen 3**	**Load A**	**Load B**	**Load C**
P [Mwatt]	-	140	100	125	90	80
Q [MVar]	-	57	20	-50	-30	-35

Table 3.3 Test system network

	No.	**Impedance R)**	**Reactance(X)**	**Conductance(G)**	**Susceptance(B)**
Generator	1	0	0.0608	-	-16.4473
	2	0	0.1198	-	-8.3472
	3	0	0.1813	-	-5.5157
Transmission Lines	4-5	0.0100	0.0850	1.3652	-11.6041
	4-6	0.0170	0.0920	1.9422	-10.5107
	5-8	0.0320	0.1610	1.1876	- 5.9751
	6-9	0.0390	0.1700	1.2820	- 5.5882
	7-10	0.0085	0.0720	1.6171	-13.6980
	8-9	0.0119	0.1008	1.1551	- 9.7843
Shunt admittance	4	-	-	-	0.1678
	5	-	-	-	0.241
	6	-	-	-	0.258
	7	-	-	-	0.0745
	8	-	-	-	0.2575
	9	-	-	-	0.2835
	10	-	-	-	0.0745
Transformer	1	-	0.0625	-	-17.3611
	2	-	0.02	-	-50.0000
	3	-	0.0586	-	-17.0648
	7	-	0.0625	-	-16.0000

The transformer can be illustrated as an ideal transformer with an admittance Y, which is the reciprocal of the impedance of the transformer. The voltage at bus *i* and *j* are V_i and V_j, respectively. The voltage at the secondary side of the transformer is $t v_i$. For an ideal transformer, the complex powers on the primary and secondary side are equal. Therefore, the relationship of the currents of the transformer is

$$I_i = -tI_j$$

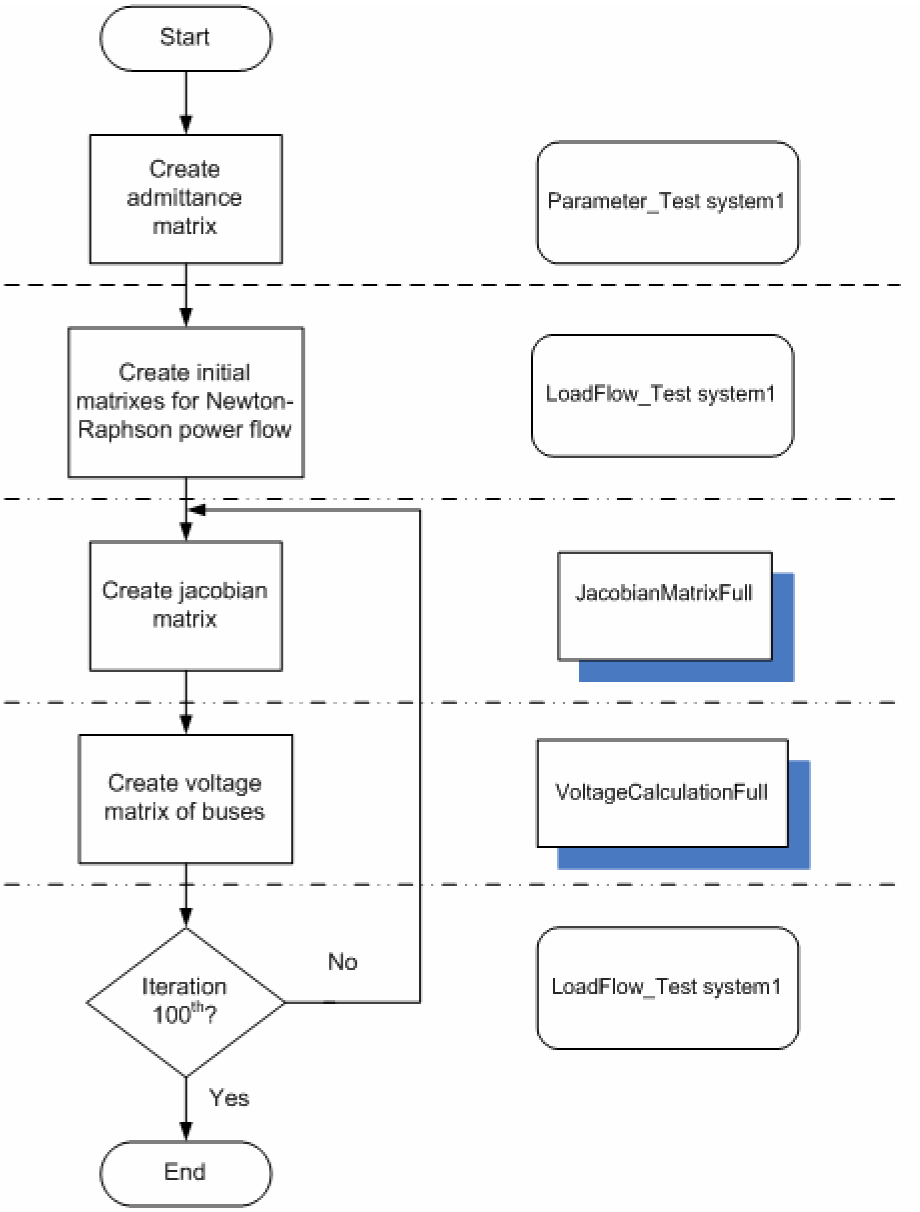

Figure 3.10 Flow chart of power flow programming

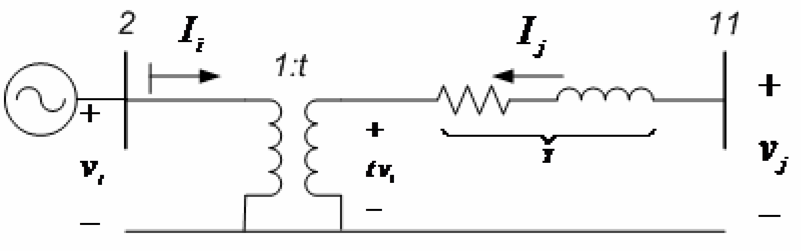

Figure 3.11 Regulating transformer

The current I_j and I_i can be expressed as [69]

$$\begin{aligned} I_j &= (V_j - tV_i)Y = -tYV_i + YV_j \\ I_i &= tt^*YV_i - t^*YV_j \end{aligned}$$

For a real value of transformer turn ratio *t*, the term tt^* is $|t|^2$. Therefore, the currents of the transformer can be expressed in matrix form as

$$\begin{bmatrix} I_i \\ I_j \end{bmatrix} = \begin{bmatrix} |t|^2 Y & -t^*Y \\ -tY & Y \end{bmatrix} \begin{bmatrix} V_i \\ V_j \end{bmatrix} \qquad \text{(equa.3.20)}$$

Figure 3.12 demonstrates the admittance matrix of the test system with the regulating transformer. Bus *i*, which is the generator bus, is bus 2 whereas bus *j* is bus 11. The complete matrix after substituting the impedance of transmission lines, transformers, and shunt admittances is demonstrated in appendix A. To validate the power flow with the regulating transformer, the voltage and complex power of the system at point of common coupling are summarized in table 3.5. The voltage and complex power of the system with the grid interconnection, which is 11-bus system, are very close to the voltage and complex power of the system without the grid interconnection. Figure 3.12 illustrates the distributed generation unit that is the aggregated wind farm and the grid interconnection. The DG-unit is connected to bus *j*, which is the point of common coupling.

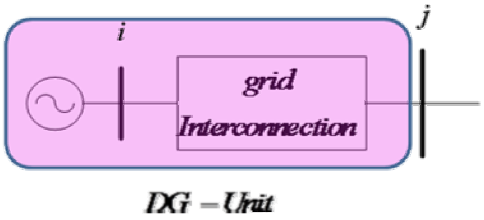

Figure 3.12 Distributed generation unit

Table 3.4 Voltage and power flow of the system with 10 and 11 buses

	10-bus system	**11-bus system**
Voltage at bus *j*	1.0487∠-0.2932	1.0374∠-0.2809
Complex power at bus *j*	1.2459∠2.8148	1.2234∠2.8085

File “LoadFlow_TestSystem1” obtains the power flow by firstly creating the vectors containing the initial voltages and complex powers of all buses tabulated in table 3.5. Only the generator buses and load buses have initial complex powers. The system is in 100-MVA base. Then, it starts an iteration procedure. It creates the jacobian matrix by calling function “JacobianMatrixFull”. The jacobian matrix relates to the partial derivatives of complex powers versus power angles and voltages of buses as described in appendix B. After obtaining the jacobian matrix, LoadFlow_TestSystem1 calls function “VoltageCalculationFull” to find the voltages of each bus. That is one iteration procedure. The LoadFlow_TestSystem1 repeats the iteration process for 100 times to find the convergence voltages and complex powers of all buses.

$$\begin{array}{cccccccccccc}
 & 1 & 2 & 3 & 4 & 5 & 6 & 7 & 8 & 9 & 10 & 11 \\
1 & Y1T & 0 & 0 & -Y1T & 0 & 0 & 0 & 0 & 0 & 0 & 0 \\
2 & 0 & t^2 \cdot Y & 0 & 0 & 0 & 0 & 0 & 0 & 0 & 0 & -t \cdot Y \\
3 & 0 & 0 & Y3T & 0 & 0 & 0 & 0 & 0 & -Y3T & 0 & 0 \\
4 & -Y1T & 0 & 0 & Y_{44} & -Y_{45} & -Y_{46} & 0 & 0 & 0 & 0 & 0 \\
5 & 0 & 0 & 0 & -Y_{54} & Y_{55} & 0 & 0 & -Y_{58} & 0 & 0 & 0 \\
6 & 0 & 0 & 0 & -Y_{64} & 0 & Y_{66} & 0 & 0 & -Y_{69} & 0 & 0 \\
7 & 0 & 0 & 0 & 0 & -Y_{75} & 0 & Y_{77} & -Y7T & 0 & -Y_{710} & 0 \\
8 & 0 & 0 & 0 & 0 & -Y_{85} & 0 & -Y7T & Y_{88} & -Y_{89} & 0 & 0 \\
9 & 0 & 0 & -Y3T & 0 & 0 & -Y_{96} & 0 & -Y_{98} & Y_{99} & 0 & 0 \\
10 & 0 & 0 & 0 & 0 & 0 & 0 & -Y_{107} & 0 & 0 & Y_{1010} & -Y2T \\
11 & 0 & -t \cdot Y & 0 & 0 & 0 & 0 & 0 & 0 & 0 & -Y2T & Y_{1111}
\end{array}$$

Figure 3.13 Admittance matrix

Table 3.5 Initial voltages and complex powers of buses in per unit

Bus	Voltage (pu)	Angle (rad)	Complex power (pu)	Load (pu)
1	1.04	0	-	-
2	1.025	-0.0015	-1.45+0.57*j*	-
3	1.025	-0.0026	-1.0+0.2*j*	-
4	1.026	-0.0027	0+0*j*	-
5	0.996	-0.0017	-	1.25-0.50*j*
6	1.013	-0.0017	-	0.90-0.30*j*
7	1.026	-0.0017	0+0*j*	-
8	1.016	-0.0017	-	0.8-0.35*j*
9	1.032	-0.002	0+0*j*	-
10	1.022	-0.0018	0+0*j*	-
11	1.012	-0.0016	0+0*j*	-

The programs are demonstrated in appendix C. The results of power flow are the operating points of the test system. Table 3.6 shows the voltages and complex powers of the buses obtained from the Newton-Raphson power flow

B. Grid interconnection

The operating points of the grid interconnection are similar to what presented in chapter 2. The duty cycle of the fly-back converter can be found by equation 2.5. V_{in} is the output voltage of the diode bridge rectifier obtained by equation 2.2. V_o is the output voltage of the fly-back converter, which is 3KV. The operating points of the multi-level inverter are demonstrated in equation 3.21.

$$d_d = \frac{V_d}{V_{dc}}$$

$$I_d = \frac{V_{dc}}{R_{dc} \cdot d_{d-j}} \qquad \text{(equa.3.21)}$$

$$d_q = \frac{-\omega L_s I_d}{V_{dc}}$$

Where $R_{dc} = \frac{P_{o2}}{V_{dc}^2}$, P_{o2} is the real power at bus 2

Table 3.6 Voltage and complex power of buses

Bus	**Voltage (pu)**	**Complex power (pu)**
1	1.0400	-0.5277 - 0.4014*j*
2	0.9011 - 0.4536*j*	-1.4552 + 0.5700*j*
3	1.0061 - 0.2750*j*	-1.0007 + 0.2090*j*
4	1.0408 + 0.0033*j*	-0.0010 + 0.0000*j*
5	1.0254 + 0.0240*j*	1.2497 - 0.5000*j*
6	1.0423 - 0.0125*j*	0.8995 - 0.3000*j*
7	0.9956 - 0.2307*j*	-0.0007 + 0.0000*j*
8	1.0035 - 0.1377*j*	0.7999 - 0.3500*j*
9	1.0116 - 0.1891*j*	-0.0009 - 0.0000*j*
10	0.9638 - 0.3536*j*	-0.0560 - 0.0000*j*
11	0.9511 - 0.4232*j*	-0.0064 + 0.0000*j*

3.6 Dynamic modeling

The dynamic stability means the capability of the system to regain to the original equilibrium points after small disturbances. The equilibrium points, therefore, remain constant throughout the simulations. The system is modeled based on assumptions that:

1. Loads are represented by constant impedances
2. The transient saliency is ignored by considering $x_q = x_d'$.

The voltage equation of a synchronous generator introduced in equation 3.10 depends on the current in d-axis. The real and reactive output powers of the generator is represented in the complex form as described in chapter 9 of [67]

$$P_e + jQ_e = E_q'\left(i_q - ji_d\right) \qquad \text{(equ.3.22)}$$

Therefore, i_d is expressed as

$$i_d = -\frac{Q_e}{E_q^{'}} \qquad \text{(equ.3.23)}$$

Obviously, the dynamic behavior of a synchronous generator is related to the real and reactive power flow of the power system. Linearizing the above equation obtains

$$\hat{i}_d = \frac{Q_{eo}}{\left(E_{qo}^{'}\right)^2}\hat{E}_q^{'} - \frac{\hat{Q}_e}{E_{qo}^{'}} \qquad \text{(equ.3.24)}$$

Where $E_{qo}^{'}$ is the voltage of generator two at steady state

Q_{eo} is the reactive power of generator two attained from the power flow

$\hat{Q}_e$ is the deviation of reactive power of generator two

To find the voltages of the generators, we will eliminate all nodes except the generator nodes. Finally, we will obtain the admittance matrix of the reduced network. Let's consider all nodes have zero current injection except the internal generator nodes [52]. The three virtual buses are added for three generator system. The virtual buses support the transient reactance of the generator as shown in figure 3.14. Let

$$I = Y \cdot V$$

Where $I = \begin{bmatrix} I_n \\ -- \\ 0 \end{bmatrix}$

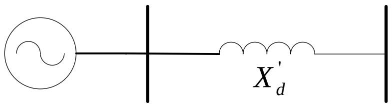

Figure 3.14 Generator with virtual bus

The admittance matrix (Y) becomes

$$\begin{bmatrix} I_n \\ -- \\ 0 \end{bmatrix} = \begin{bmatrix} Y_{nn} & | & Y_{nr} \\ -- & | & -- \\ Y_{rn} & | & Y_{rr} \end{bmatrix} \begin{bmatrix} V_n \\ -- \\ V_r \end{bmatrix}$$

Where Y_{nn} is the generator nodes added to the admittance matrix.

For the 3-generator system, the dimension of Y_{nn} is 3×3. The admittance matrix, therefore, has dimension 14×14. The order of the buses can be expressed as

$$[1' \quad 2' \quad 3' \quad 1 \quad 2 \quad 3 \quad 4 \quad 5 \quad 6 \quad 7 \quad 8 \quad 9 \quad 10 \quad 11]$$

where " $'$ " denotes the virtual generator buses

It is obvious that Y_{nr} has 3×11 elements, Y_{rn} has 11×3 elements, and Y_{rr} has 11×11 elements, which is the original admittance matrix. The admittance matrix with the virtual buses is demonstrated in appendix A. To find the reduced admittance,

$$I_n = Y_{nn} \cdot V_n + Y_{nr} \cdot V_r$$

$$Y_{rn} \cdot V_n + Y_{rr} \cdot V_r = 0$$

Eliminate V_r to obtain

$$I_n = \left(Y_{nn} - Y_{nr} \cdot Y_{rr}^{-1} \cdot Y_{rn}\right) \cdot V_n$$

The reduced admittance matrix $Y_{nn} - Y_{nr} \cdot Y_{rr}^{=1} \cdot Y_{rn}$ has 3×3 elements. We then find the complex powers, which are shown in equation 3.22, of the generators. These complex powers are the powers at the operating point of the generators

$$S = V_n \cdot I_n^* \qquad \text{(equa.3.25)}$$

Where V_n and I_n are the voltages and currents of generators

Substitute i_d from equation 3.24, the small signal equations of the internal voltage of the synchronous generator becomes

$$\hat{E}_q^{'\bullet} = \frac{1}{T_{do}^{'}}\left[-\hat{E}_q^{'} + (x_d - x_d^{'})\left(\frac{Q_{e0}}{\left(E_{qo}^{'}\right)^2}\hat{E}_q^{'} - \frac{\hat{Q}_e}{E_{qo}^{'}}\right) + \hat{E}_{fd}^{'} \right] \qquad \text{(equa.3.26)}$$

The real and reactive powers ($\hat{P}_e, \hat{Q}_e$) in equation 3.10 and 3.22 are the deviation of real and reactive powers of the generators. By the method to obtain the jacobian matrix, we can find $\hat{P}_e, \hat{Q}_e$. The system is a multi-input multi-output or MIMO system. It is convenient to model the system in the time-domain or the state space approach. Without the grid interconnection in this step, we can express the dynamic equations of the system as

$$\hat{X}^{\bullet} = [A]\hat{X} + [B]\hat{U} \qquad \text{(equa.3.27)}$$

where $\hat{X} = \left\lfloor \hat{\bar{\omega}}_{G1} \quad \hat{\bar{\omega}}_{G2} \quad \hat{\bar{\omega}}_{G3} \quad \hat{\bar{\omega}}_{W2} \quad \hat{\delta}_{G1} \quad \hat{\delta}_{G2} \quad \hat{\delta}_{G3} \quad \hat{\delta}_{W2} \quad \hat{\bar{E}}_{q2}^{'} \quad \hat{\bar{E}}_{q3}^{'} \right\rfloor$

$\hat{U} = [\hat{\bar{P}}_{m1} \quad \hat{\bar{P}}_{m2} \quad \hat{\bar{P}}_{m3} \quad \hat{\bar{E}}_{fd1} \quad \hat{\bar{E}}_{fd2}\ ]$

(-) denotes per unit quantities

The state matrix A of the state variables shown above is a singular matrix since its determinant is zero. As described in chapter 9 of [67], the deviation of the real and reactive powers in equation 3.10 and 3.22 depend only on the relative rotor angles of the generators. Since bus one is the slack bus, let's use the generator one as the reference generator. The state variables of the system become, including the grid interconnection

$$\hat{X} = [\hat{\bar{\omega}}_{G1} \quad \hat{\bar{\omega}}_{G2} \quad \hat{\bar{\omega}}_{G3} \quad \hat{\bar{\omega}}_{W2} \quad \hat{\delta}_{G2} \quad \hat{\delta}_{G3} \quad \hat{\delta}_{W2} \quad \hat{\bar{E}}_{q2}^{'} \quad \hat{\bar{E}}_{q3}^{'} \quad \hat{\bar{i}}_{LM} \quad \hat{\bar{V}}_{dc} \quad \hat{\bar{i}}_{d} \quad \hat{\bar{i}}_{q}]$$

$$\hat{U} = [\hat{\bar{P}}_{m1} \quad \hat{\bar{P}}_{m2} \quad \hat{\bar{P}}_{m3} \quad \hat{\bar{E}}_{fd1} \quad \hat{\bar{E}}_{fd2} \quad \hat{d} \quad \hat{d}_d \quad \hat{d}_q \quad \hat{v}_d \quad \hat{v}_q]$$

Where $\hat{\delta}_{G2}$ and $\hat{\delta}_{G3}$ are the relative rotor angles respect to the angle of the generator one

The state matrix A containing complete differential equations of the system including the grid interconnection is demonstrated in appendix A. For generator one, the rotor speed is modeled by equation 3.11. The generator two is modeled by equation 3.10

with the modified internal voltage in equation 3.26 whereas the grid interconnection is modeled by equation 3.16-3.19. The generator three is modeled by equa.3.11, 3.12 and 3.26.

3.7 Control system

The system, which is consisted of multi-machines and power electronic grid interconnection, is vulnerable to perturbations of the inputs. Therefore, there must be a control system to minimize the effects of the perturbations. The purpose of the control system is to track the desired value of outputs and keep the error between the desired and the actual outputs close to zero. Figure 3.15 shows the state space system with feedback control to achieve the output tracking.

Now the input vector *U(t)* is the difference between the desired state variable vector *r(t)* and the actual state variable vector *x(t)* factored by feedback gain matrix *K* as described in[26].

$$u(t) \quad = \quad -Kx(t) + r(t) \qquad \text{(equa.3.28)}$$

The state space model becomes

$$\dot{x}(t) \quad = \quad (A - BK)\cdot x(t) + BK \cdot r(t)$$

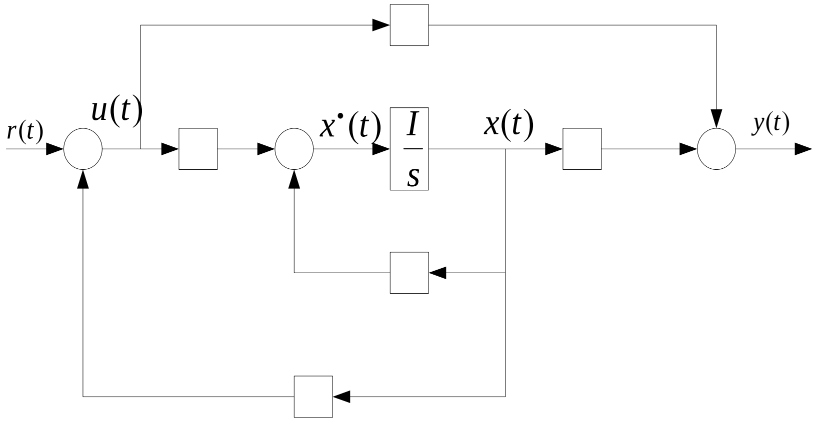

Figure 3.15 State feedback control

The state matrix A of the closed loop system becomes $A - BK$ and the input matrix B of the closed loop system becomes BK. The classical control focusing on the SISO (Single-Input-Single-Output) systems, which is characterized by transfer functions, is rather tedious for the MIMO (Multiple-Input-Multiple-Output) systems. The MIMO system is instead characterized by the state space matrixes. One of the control systems is pole-placement method. More detail relating to the pole placement by state feedback is described in chapter 4 of [26]. The pole or the eigenvalue locations of the system determine the system characteristics and stability. The system is internally stable when real parts of all eigenvalues are negative or locate in the left half plane of the s-plane. The system response decays with time. Oppositely, the system is unstable when one of the eigenvalues has positive real part. The system response grows with time. The system is neither converged nor diverged when some eigenvalues are pure imaginary [70]. The negative real part corresponds to the rate of decay of that mode. The further the negative poles or eigenvalues locates from the y-axis, the faster the system decays in that mode [71]. Hence, it is desirable that the poles locate far away from the y-axis. The system will oscillate about an equilibrium point. The pole-placement method is basically to find the feedback matrix *K* that relocates the closed loop poles of the system to the predetermined locations.

There are several optimal control theories for the MIMO system. One theory is Linear Quadratic Regulator (LQR). This technique relates to selecting the feedback gain matrix *K* that minimizes the quadratic cost function *(J)*[72].

$$J = \int_0^\infty x(t)^T Q \cdot x(t) + u(t)^T R \cdot u(t) dt \qquad \text{(equ.3.29)}$$

With this control technique, it is not necessary to specify the desired closed loop pole locations, which is difficult for the MIMO system. The typical goals are to keep the deviation of state variables from the desired values close to zero. Therefore, the high values of elements of matrix *Q* relative to elements of matrix *R* means the high penalty on the deviation of the state variable vector *x* from zero. On the other hand, the control effort will be more costly and the deviations of the state variables will not converge to zero quickly when the element of matrix *R* are high relative to the elements of the matrix *Q*.

The matrix *Q* and *R* must be positive semi-definite and positive definite, respectively, to obtain the positive cost function *J*. The term positive definite refers to following properties of a matrix *N* [73]:

1. $n_{ii} > 0$ for all i
2. $n_{ii} + n_{jj} > 2\,\Re[n_{ij}]$ for $i \neq j$
3. The element with largest modulus lies on the main diagonal
4. det (*N*) > 0
5. The matrix is symmetric

The properties of positive semi-definite are very similar to the positive definite except that eigenvalues can be zero or non-negative for the positive semi-definite. For zero deviations of the state variables, vector *r(t)* is zero. Then, substituting the input vector in equation 3.28 to the cost function *J* obtains

$$\begin{aligned} J &= \int_0^\infty x(t)^T Q \cdot x(t) + (-K\,x(t))^T R \cdot (-K\,x(t))dt \\ &= \int_0^\infty x(t)^T (Q + K^T RK) \cdot x(t)\,dt \end{aligned}$$

Solving the cost function *J* involves the Lyapunov equation. Let

$$Q + K^T RK = S$$

Assuming that the closed-loop system in internally stable. The cost function *J* becomes

$$J = \int_0^\infty x(t)^T \cdot S \cdot x(t)\,dt = x_o^T \cdot P \cdot x_o$$

Where $x_o = x(0)$ and $P = P^T$ is the positive definite (semi-definite) solution of the Lyapunov equation

$$\widetilde{A}^T P + P\widetilde{A} = -S$$

Where $\widetilde{A}$ is the closed-loop matrix $= A - BK$.

The solution of the cost function *J* can be evaluated by solving the linear equations without computing the quadratic integral equation directly. The gain matrix that solves the LQR problem is

$$K \quad = \quad -R^{-1}B^{T}P$$

To solve the feedback gain matrix *K*, the matrix *P* is the solution of the Algebraic Riccatic equation (ARE) [72]

$$A^{T}P + PA - PBR^{-1}B^{T}P + Q \quad = \quad 0$$

Matlab has function LQR that solves the gain matrix *K* and finds the eigenvalues of the closed-loop system. To achieve the output tracking, the elements of the matrix *Q* must be high relative to the elements of the matrix *R*. The system has open loop eigenvalues as followed

Table 3.7 Open-loop eigenvalues of the system

-0.0822 ± 10.9146i	-0.0647± 4.2405i	-0.1048 ± 1.6009i	-0.1296 ± 1.0061i
-0.5800	-0.3594	-0.0682 ± 0.2812i	-0.0040

The system is stable when the real parts of all eigenvalues are negative. The function “lqr” in Matlab finds the feedback gain matrix *K* according to the penalty matrixes *Q* and *R*. This function also returns the matrix *S* in the Riccati equation and the eigenvalues of the closed-loop system. The matrixes *Q* and *R* are selected to have same weighted with 500 and 5, respectively, for all diagonal elements. The closed-loop eigenvalues are demonstrated in table 3.7. With the optimal control, the closed loop eigenvalues are moved toward the negative real axis.

Table 3.8 Closed-loop eigenvalues of the system

-149.44	-12.304 ± 16.443i	-18.635	-3.5855 ± 3.62
-2.7523 ± 1.1833i	-1.6453 ± 2.0042i	-1.8191 ± 0.00363i	-0.10082

Chapter 4 Simulation Results

The simulation results are separated into two parts. The first part is the simulation of the grid interconnection of wind turbines without other machines. The utility grid is a strong network and represented by a three phase voltage source. The compensator obtained from the small signal models described in chapter 2 is used in the simulations with the switching model. The switching model simulated in PSCAD utilizes IGBTs (Insulated Gate bipolar Transistor) as power switches. The IGBT model in PSCAD is allowable to set characteristics such as resistance, forward voltage drop, breakdown voltage, and RC snubber. The second part is the simulations of the aggregated wind farm in a multi-machine system. The system is programmed in Matlab and simulated with perturbations and the optimal control in Simulink.

4.1 The grid interconnection

In the first part, the system is simulated in 2 operations, normal operation and short circuit fault operation. In the normal operation, the grid interconnection controls the real and reactive powers of the wind generation supplied to the utility grid. As described in equation 2.43, the real and reactive powers are controlled by controlling the currents of the utility grid in d- and q-axis.

A. Normal mode

The first simulation is to control the reactive power. The reactive power in the middle graph of figure 4.1 is changed from 0 to 1MVar and -1MVar whereas the real power in the top graph is regulated at 110KWatt. At 0.2 seconds, the wind generation absorbs the reactive power from the grid 1MVar. At 0.55 seconds, the wind generation injects the reactive power to the supply grid 1MVar. During the transformation, the voltages of the DC links in the bottom graph are maintained constant.

Figure 4.2 shows the transient response of the reactive power from -1MVar to 1MVar. The reactive power is changed from inductive mode (-Q) or leading current to capacitive mode (+Q) or lagging current. In accordance with the transformation, the current and voltage of the utility grid in phase A is shown in the top graph of figure 4.3. To show the voltage and current of the utility grid clearly, the voltage magnitude is reduced by factor 0.2. The voltage of the converter is the synthesized step voltages that reduce the harmonic distortions as shown in the middle graph of figure 4.3. With the feedback control design described in chapter 2, the voltages of the DC links in the bottom graph have low percent overshoot around 3%.

For the second simulation, system is simulated to control the real power whereas the reactive power is maintained constant at 1MVar as illustrated in the middle graph of figure 4.4. The real power in the top graph is changed from 110KWatt to 340KWatt. Similarly, the voltages of the DC links are maintained constant during the operation. As seen from figure 4.1-4.3, the grid interconnection with the control system can control real and reactive powers independently.

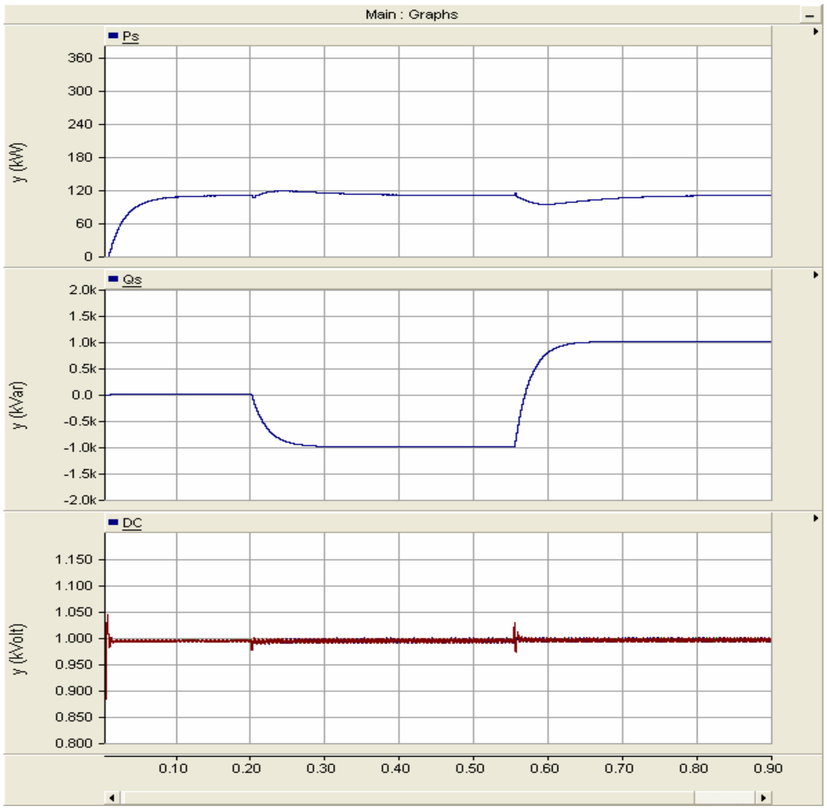

Figure 4.1 (Top) Real power (Middle) Reactive power (Bottom) DC link voltage

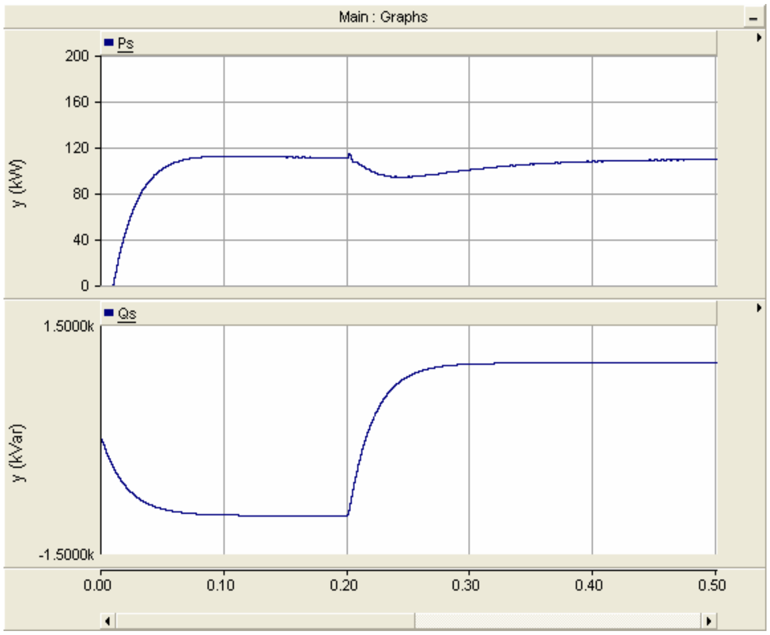

Figure 4.2 Transient response of (Top) Real power (Bottom) Reactive power

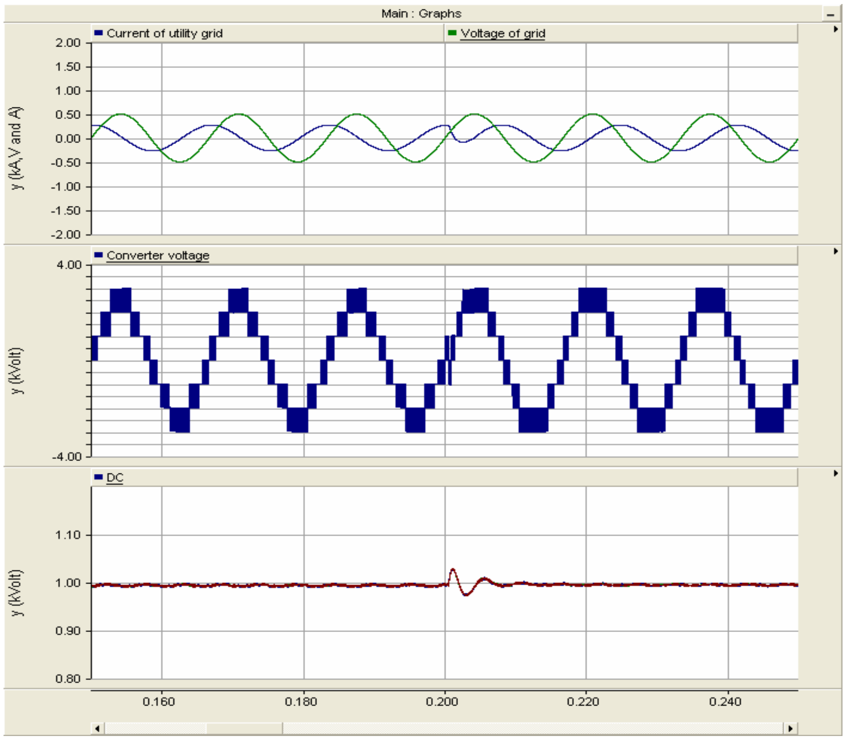

Figure 4.3 (Top) Voltage and current of the grid (Middle) Voltage of multi-level inverter (Bottom) DC link voltage

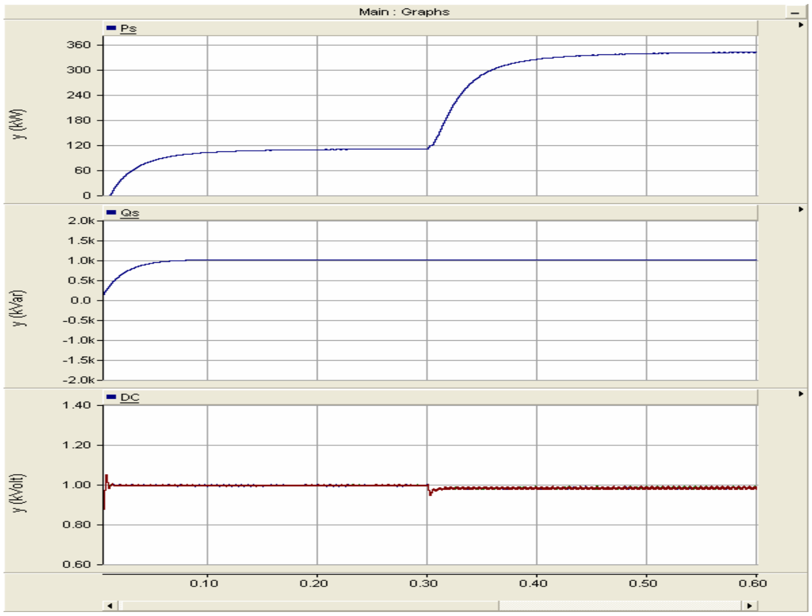

Figure 4.4 (Top) Real power (Middle) Reactive power (Bottom) DC link voltage

B. Fault mode

The system is also simulated in the short circuit fault operation. The faults are SLGF (Single-Line-Ground Fault) and three phase fault. The three phase fault is a balanced fault that all three lines are short to ground. The SLGF is the most common type caused by lightning or conductor making contacts with grounded objects such as trees. Typically, the asymmetrical fault happens much more often than the three phase fault. Figure 4.6 and 4.7 show the connection diagram of a SLFG and three phase fault through impedance Z_f, respectively. More detail of symmetrical and asymmetrical faults is described in chapter 10 and 12 of [69]. For SLGF, phase A is the phase at which the fault occurs.

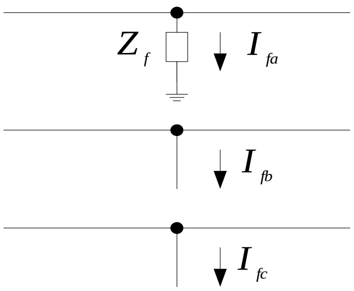

Figure 4.5 SLFG

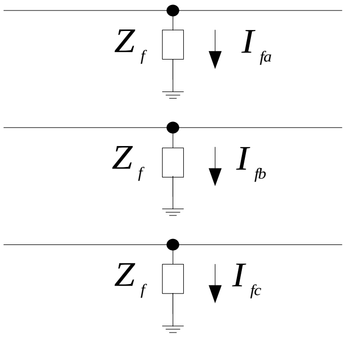

Figure 4.6 Three phase fault

Figure 4.7 shows the voltage and current of the utility grid during short circuit faults, as well as the voltage of the DC links. At 0.2 seconds and 0.5 seconds, the utility grid is shorted with single-line-ground-fault (SLGF) and 3-phase fault, respectively.

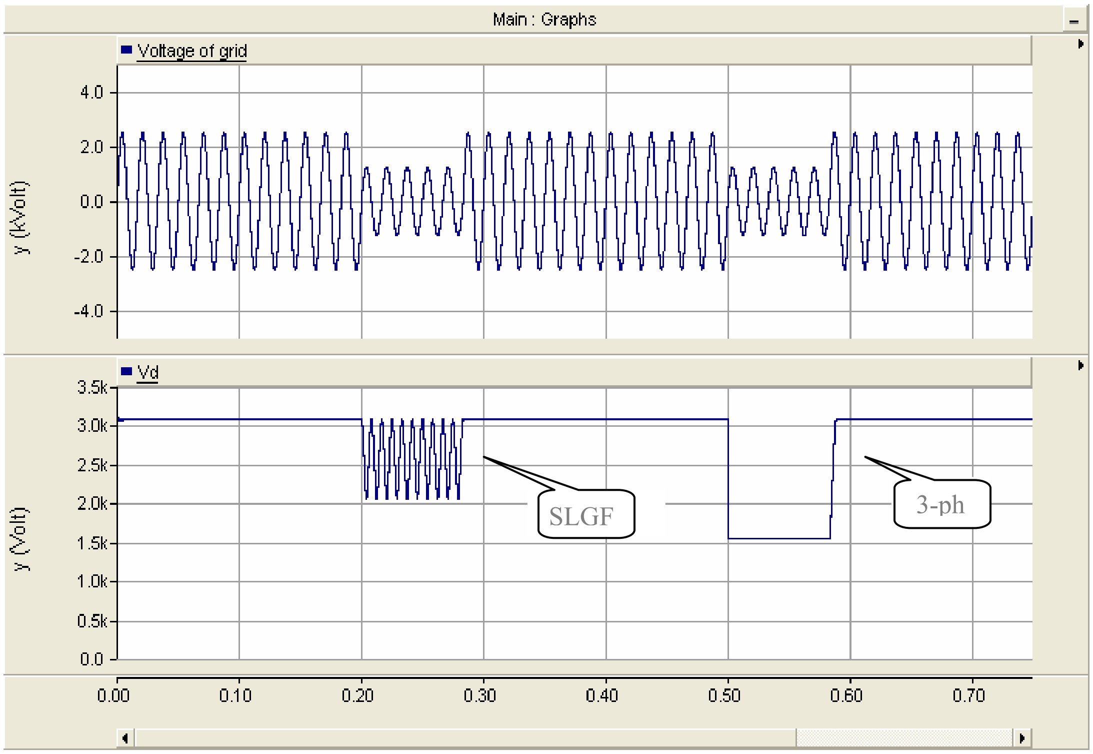

Figure 4.7 (Top) Voltage of the grid in phase A (Bottom) in d-axis

The voltage of the utility grid in the ABC coordinate, shown in the top graph of figure 4.8, has a voltage sag around 50% of its normal voltage for both faults. It is obvious that the SLGF, which is an asymmetrical fault, causes unbalanced conditions. This results in the oscillation of the voltage in d-axis, as shown in the bottom graph. This is because the transformation from the static reference frame to the rotating reference frame requires the balanced three phase system. Figure 4.8 shows the ripples of the DC link voltage and current of the utility grid during the faults. The clearing fault is in 5 cycles.

As the level of penetration of the wind energy increases, the wind farm is required to have LVRT (Low Voltage Ride Through) capability that the wind generators must remain connected to the power system during grid disturbances. The proposed grid interconnection has the LVRT ability to maintain DC link voltage and recover the system after the faults.

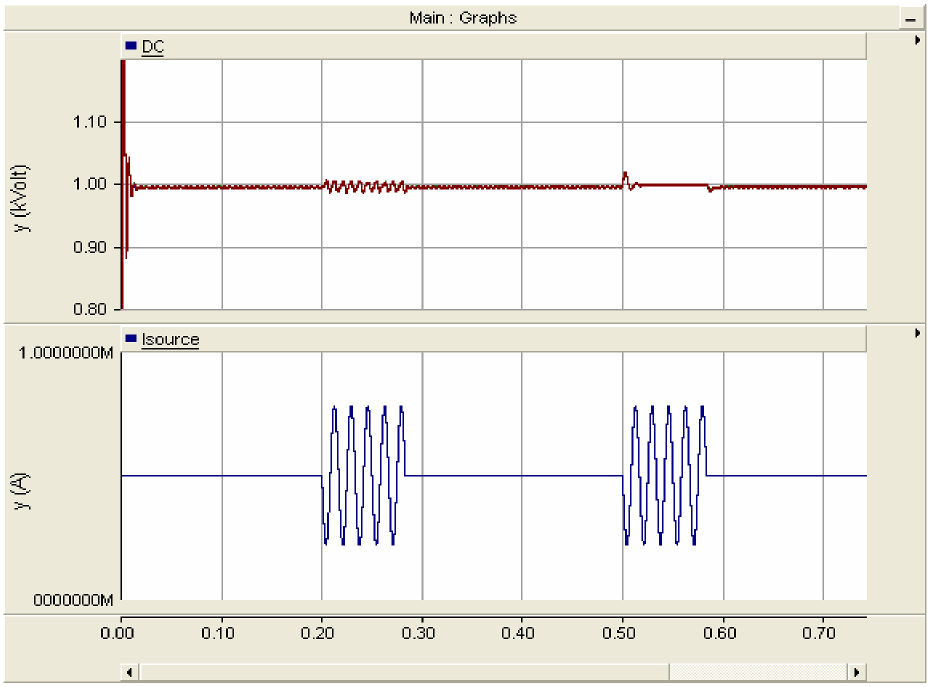

Figure 4.8 (Top) DC link voltage (Bottom) Current of the grid

4.2 Dynamic modeling of an aggregated wind farm

The multi-machine system is simulated in Simulink in time domain with a feedback control illustrated in figure 3.12. The differential equations of the system represent the deviation of the actual outputs from the desired values. Therefore, the inputs of the simulations are the deviation or perturbations from the steady state values.

The goal of modeling of an aggregated wind farm in a multi-machine system is to analyze the impacts of the wind energy to the power system and vice versa. There are several modes of oscillations. The most common type is local mode. In this mode, the machine oscillates against other machines in the system. The frequency of oscillation is in the range of 1-2 Hz. On the other hand, the inter-area mode is the oscillation of machines in one group against machines in the other groups. The frequency of oscillation is in the range of 0.1-1 Hz. More detail is described in chapter 9 of [10]. In the first simulation, we will perturb the mechanical power of generator three with a step input.

Fig.4.9 illustrates the angular speed of the generators when the mechanical power or mechanical torque of generator three is perturbed at 0.01 PU and generator two is perturbed at -0.01 PU. It is obvious that, at the beginning of the simulation, generator one and generator three oscillate against each other in the local mode with frequency around 1.73 Hz. Generator two oscillates against generator three and generator one in the inter-area mode with frequency around 0.16 Hz.

Figure 4.10 illustrates the angular velocity of generator three against generator two with and without the control system. The graph demonstrates oscillations in both local and inter-area modes. Apparently, the optimal control reduces the effects of the perturbation rapidly and substantially.

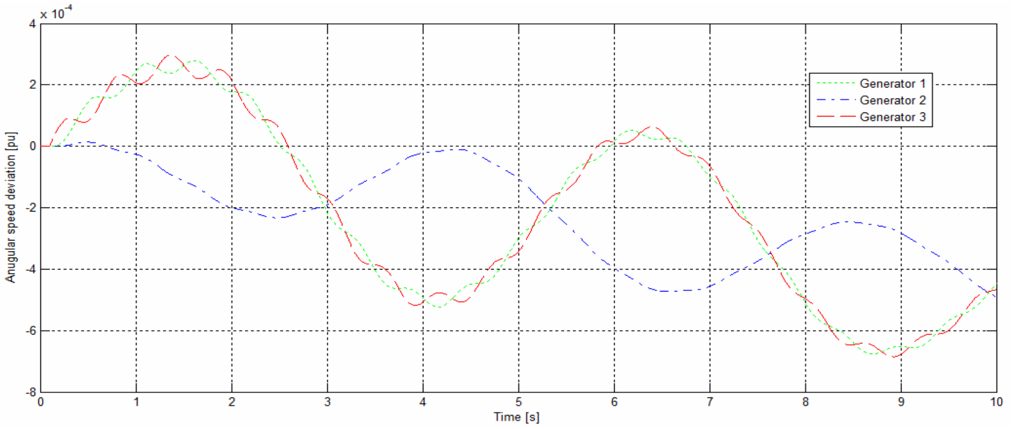

Figure 4.9 Angular speed deviations of generators when P_{m3} and P_{m2} are perturbed

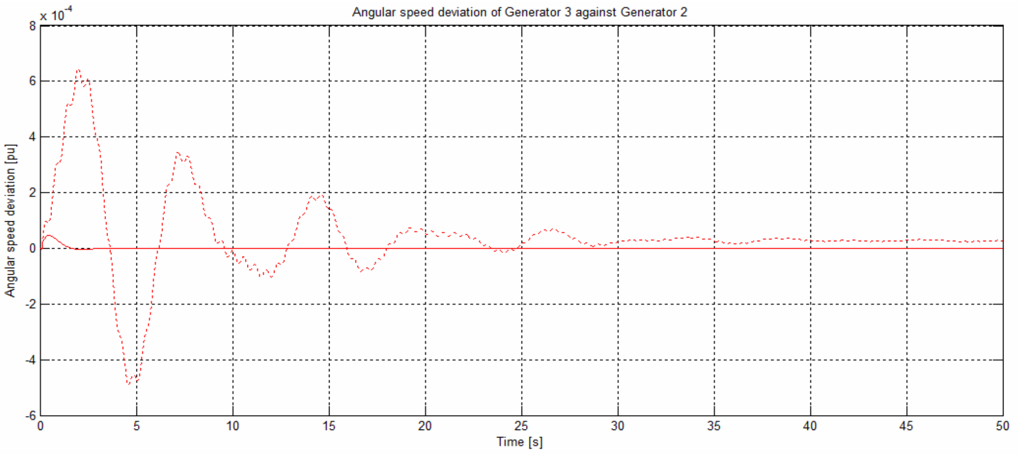

Figure 4.10 Angular speed deviations of generators 3 against generator 2

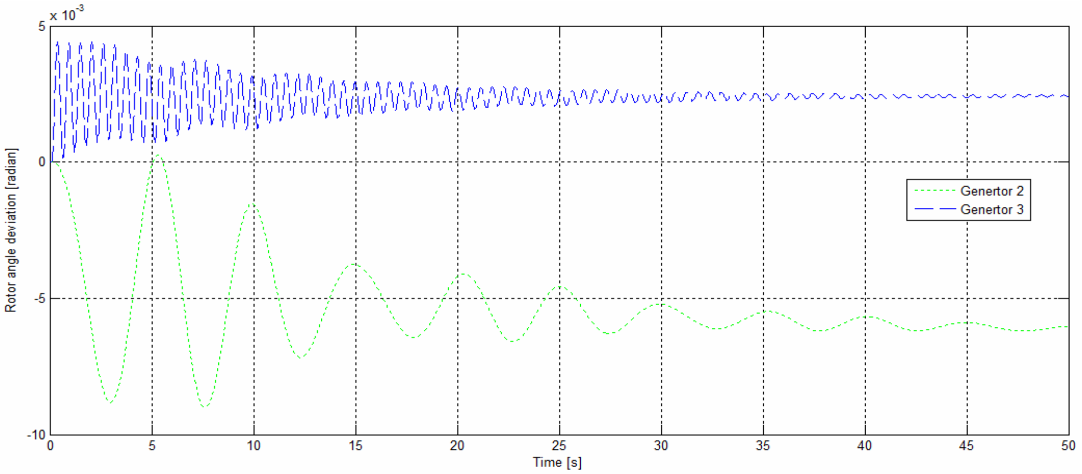

Figure 4.11 Rotor angle deviations of generators when P_{m3} and P_{m2} are perturbed

The perturbation has affects on the rotor angles of generator two and three as illustrated in figure 4.11. The rotor angle of generator two shows clearly the inter-area mode of oscillation whereas the rotor angle of generator three shows both local and inter-area modes. The rotor angle of generator two is influenced by the perturbation with step input more than generator 3 in the inter-area mode.

Figure 4.12 illustrates the rotor angle of generator 3 against generator 2. The dashed line represents the rotor angles without the control system whereas the solid lines represents the rotor angles with the control system. The dashed line shows obviously the local and inter-area modes of oscillation, which tends to increase with time. The control system reduces the deviation substantially in a very short time.

Figure 4.13 illustrates the transient internal voltages of generator 2 and 3 and the results of the optimal control. Without the control system, the internal voltages continue decreasing with time. Generator 2 receives more influences from the perturbation.

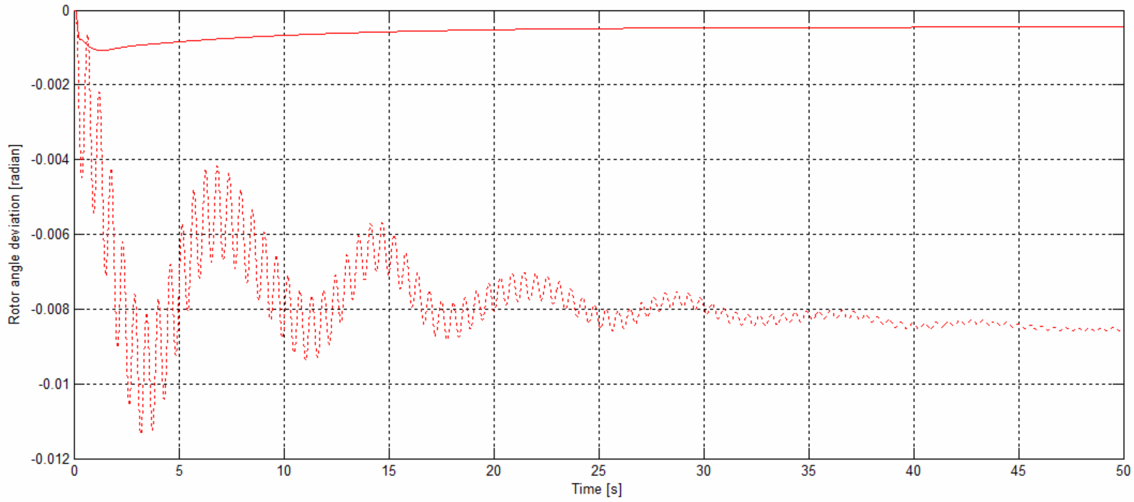

Figure 4.12 Rotor angle deviation of generator 3 against generator 2

The perturbation affects the real and reactive powers of the generator two as illustrated in figure 4.14. The dashed lines represent the powers without the control system whereas the solid lines represent the powers with the control system. Without the control system, the real and reactive powers are perturbed to -0.02 and 0.015 PU, respectively. The optimal control of the multi-machine system reduces the deviation of the real and reactive powers to infinitesimal values.

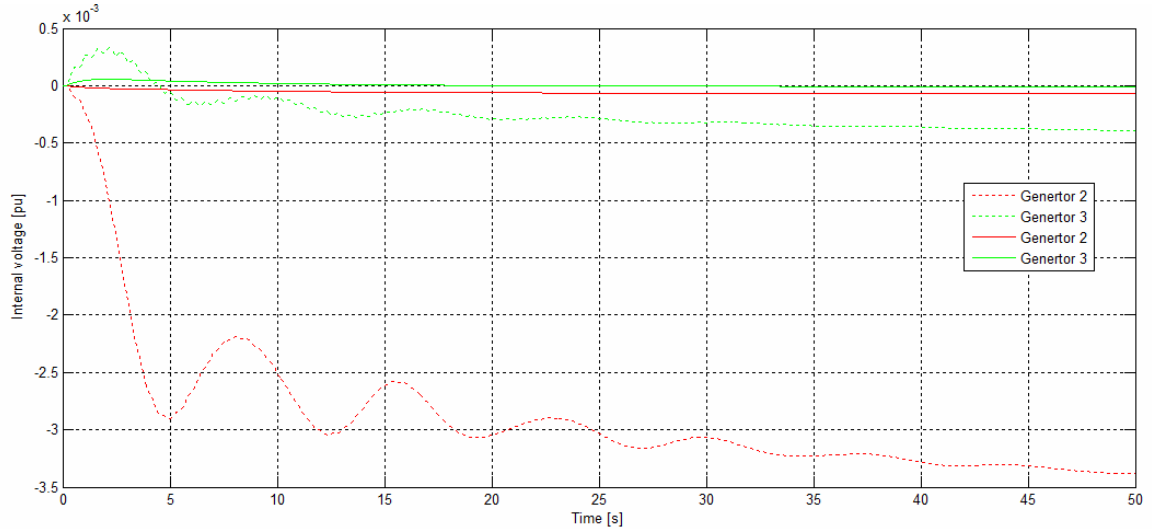

Figure 4.13 Internal voltage deviations of generators when P_{m3} and P_{m2} are perturbed

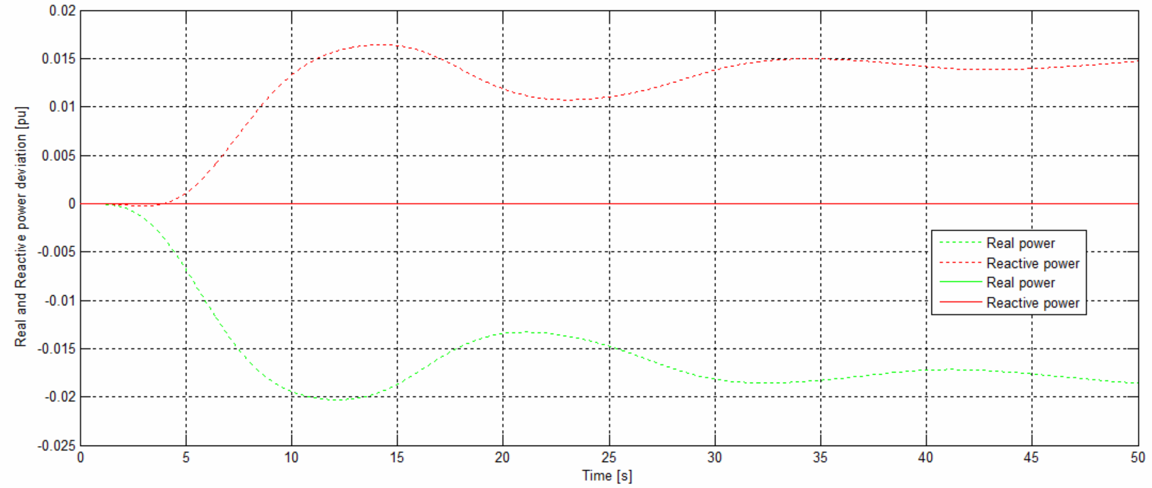

Figure 4.14 Real and reactive power deviations of generator 2

Chapter 5 Conclusion and future work

5.1 Conclusion and discussion

As the level of penetration of the wind power is increasing, it is necessary to analyze and evaluate the impacts of the wind power to the power system. Interconnecting wind power influences the performance of the power system in the light of stability, reliability, and quality. Generally, it is acceptable to aggregate a wind farm to one single unit depending on the location and configurations of the system. The dynamic modeling of the aggregated wind farm in a multi-machine system presented in this dissertation contributes to prediction of the system performance. It is beneficial to the operators and planners to acknowledge the system interactions after disturbances.

There are various models of wind turbines and synchronous generators dependent on the detail and applications of the models. Modeling the system by programming has an advantage to arbitrary selections and modifications of the models. Additionally, it is feasible to model the grid interconnection to the system. This is desirable for modeling the wind power with various types of generators and power electronic interface.

Typically, a wind farm locates in the remote area with a long cable to transmit powers to the grid. This leads to inter-area oscillations against machines in the other area. A disturbance at one machine affects the power stability and quality of the other machines. The rotor angle stabilities are perturbed after disturbances. The rotor angles of generators separate apart that initiate the synchronization problems. The power system has many elements leading to the complex control system. Fortunately, the optimal control is suitable for MIMO (Multi-Input-Multi-Output) system. This results in simplification of the control system design. The simulation results demonstrate the substantial reduction of the effects from disturbances with an optimal control system. Therefore, the control system enhances the stability and reliability of the power system.

It is beneficial to model the system with dynamic load modeling. The variety in load demand changes with time of day and night. The high load demand at day affects the power flow of the system. The static load model is time invariant and determined by the active and reactive powers at a certain time. Contrarily, the dynamic load model expresses this relation at any instant of time, as a function of the voltage and/or frequency at past instant of time, including normally the present moment [74]. It is more accurate the model the system with dynamic load modeling. Nonetheless, the modeling will be more complex and time-consuming. In some cases, static load model is sufficient to estimate the load demand.

The proposed grid interconnection fulfils the requirements for a variable speed wind farm. Wind turbines can operate with variable speed that reduces the mechanical stress and power fluctuation problems. The DC link voltages are regulated by fly-back converters, which separate the wind turbines and the utility grid. This avoids the problems of current circulations. The grid side inverter is multi-level inverter with cascaded full bridge converters. This type of inverter decreases the harmonic distortion of the currents and voltages of the utility grid at point of common coupling improving the power quality.

The selected power conversion system is suitable to the wind turbine with synchronous generator. The synchronous generators, unlike the induction generator, do not require the reactive power. The proposed grid interconnection can rectify the AC voltages with the reduced numbers of components. It is important that the wind power provides dynamic real and reactive power control. The power flow control impacts the frequency and voltage control of the power system. The grid interconnection with current control in rotating synchronous reference frame can control the real and reactive powers independently.

The proposed grid interconnection has LVRT (Low Voltage Ride Through) capability, which is recently recommended as the capacity of the wind power is increasing. The proposed grid interconnection is tested with both symmetrical and asymmetrical faults with 5 cycle clearing time. The simulations showed that the wind farm with the grid interconnection can tolerate the disturbances and recover to the normal operation after the faults.

The wind power can apply to several levels of powers from few tens of kilowatts to hundreds of megawatts. There are several standards and requirements of the wind power that researchers and manufacturers should be concerned of for different power levels. In addition to the IEEE519 that recommends limit of the harmonic distortion, IEEE1547 recommends the standard for interconnecting distributed resources with electric power systems. For distribution level, this standard recommends the requirements such as voltage regulation and synchronization at the point of common coupling, protection of electromagnetic interference, intentional and unintentional islanding. The criteria of FERC for voltage flicker and LVRT is a concern criterion for wind turbines. The requirements vary with the region. The LVRT requirements of Canada are stricter than the requirements of the USA.

In summary, the dynamic modeling and the proposed grid interconnection have advantages as followed:

1. The dynamic modeling predicts the system interactions of a wind farm after disturbances as the location and type of wind farm highly influences the impact of the wind farm on the power system.. This contributes to the power system planner and operator to control and prevent undesirable instability.
2. Modeling of the system by programming increases the degree of freedom in selecting the models of wind turbines, generators, loads, and control systems.
3. It is possible to model various types of the power electronic grid interface and other types of distributed generating units in the state space form.
4. The system modeled in state space form is suitable for the optimal control system. It is feasible to develop a novel control system.
5. The grid interconnection has individual interfaces of wind turbines. This supports the concept of the variable speed wind turbines.
6. The fly-back converter regulates the voltages of the capacitors or DC link voltages. This intermediate converter improves the power quality because low transients from fluctuations of the wind appear in the utility grid.
7. The fly-back converter eliminates problems of unbalancing voltages of the capacitors. This results in the feasibility of the real power control.
8. The wind turbines are connected individually. This system, therefore, provides reliability due to a fractional impact of each wind turbine on overall power production.
9. The multi-level inverter with isolation on the AC side utilizes fewer switching devices, diodes, and capacitors.

10. The multi-level inverter synthesizes the staircase voltages. These voltages have low harmonic distortions, thereby improving the power quality.

11. With the control system that will be described in the following topic, the grid interconnection provides an individual control of real and reactive powers. This enhances the voltage and frequency stability of the power system.

5.2 Future work

Power system deregulation is established in the demand of cost-efficient electricity. The traditional vertical monopoly system is restructured to horizontal integrated system. This leads to a competition in electricity market. The governmental generating units and transmission units, in some cases, are privatized to independent operators. Customers have freedom of selecting the electricity providers resulting in the lower prices and better qualities. The generating units tend to decrease in size and locate near customers. Consequently, the electricity is transferred to customers over short transmission lines with voltages in distribution level. The distributed generation avoids the cost of installing new transmission lines [75],[76].

The power system, both centralized and restructured system, should remain reliable through the operation. It is necessary that power supply meets the power demand. The system operators manage the transmission of electricity without power outages in some areas. This generates the need of WAM (Wide Area Measurement), which contributes to secured electric power system. The PMU (Phasor Measurement Unit) introduced by Virginia Tech measures the voltages and currents of buses around the system in real time. Phase angles of the buses can then be calculated. It is advantageous to the control system based on the actual values from the remote components.

The frequencies of oscillation determine the oscillation modes. The control system is designed to damp oscillations in specific modes. The system changes as time passes. Consequently, the control system is not effective. It is desirable that the control system can damp all oscillatory modes. The collocated control introduced in [77] is the solution to the problem. The paper assigns the eigenvalues of the LFSS (Large Flexible

Space Structure) system to the desired locations via DVFC (Direct Velocity Feedback Control). Assume the problem is in the following form

$$\ddot{\eta} + D\dot{\eta} + \Lambda^2\eta \quad = \quad Bu$$

Where $u \quad = \quad -Fy$, $y \quad = \quad B^T\dot{\eta}$

The η is the vector of modal coordinates. *u* is the vector of control inputs. *y* is the vector of measurement. The matrix Λ is the diagonal matrix of square of oscillation frequencies, Λ = diag $\{\omega_1^2, \omega_2^2, \ldots, \omega_n^2\}$, with $\omega_1 < \omega_2 < \ldots \omega_n$. The damping matrix D is proportional to frequencies, $D \; = \; 2\alpha\Lambda$ where α is the damping coefficient $= diag\ \{\alpha_1, \alpha_2, \ldots, \alpha_n\}$. *F* is feedback gain matrix, which is the non-negative definite. The basic idea is to determine the matrix *F* that gives closed-loop eigenvelues in the form of

$$\ddot{\eta} + D(F)\dot{\eta} + \Lambda^2\eta \quad = \quad 0 \quad ; \quad D(F) \quad = \quad 2\alpha\Lambda + BFB^T$$

The collocated control is challenging and attractive since it assures the oscillatory damping of the system without knowing the modes of oscillations. Furthermore, this methodology affirms the effective control with variation of modes as time passes.

Appendix A. Test system programming

A.1 Admittance matrix

The admittance matrix of the test system has 11×11 elements. Table A.1 demonstrates the admittance matrix for column 1 to 6 and table A.2 demonstrates column 7 to 11 as followed:

Table A.1 Admittance matrix column 1 to 6

-17.3611j	0	0	17.3611j	0	0
0	0.3376 - 12.7284j	0	0	0	0
0	0	-17.0648j	0	0	0
17.3611j	0	0	3.3074 - 39.3879j	-1.3652 + 11.6041j	-1.9422 + 10.5107j
0	0	0	-1.3652 + 11.6041j	2.5528 - 17.4262j	0
0	0	0	-1.9422 + 10.5107j	0	3.2242 - 15.9199j
0	0	0	0	0	0
0	0	0	0	-1.1876 + 5.9751j	0
0	0	17.0648j	0	0	-1.2820 + 5.5882j
0	0	0	0	0	0
0	- 0.3445 + 12.9882j	0	0	0	0

Table A.2 Admittance matrix column 7 to 11

0	0	0	0	0
0	0	0	0	- 0.3445 + 12.9882j
0	0	17.0648j	0	0
0	0	0	0	0
0	-1.1876 + 5.9751j	0	0	0
0	0	-1.2820 + 5.5882j	0	0
1.6171 - 29.6235j	16j	0	-1.6171 + 13.6980j	0
16j	2.3427 - 31.6549j	-1.1551 + 9.7843j	0	0
0	-1.1551 + 9.7843j	2.4371 - 32.2584j	0	0
-1.6171 + 13.6980j	0	0	1.6171 - 63.6235j	50j
0	0	0	50j	0.3515 - 63.2533j

The virtual buses are added to the admittance matrix to obtain the generator voltages and complex powers. Table A.3 shows the admittance matrix of the virtual buses, Y_{nn} , Y_{nr} , and $Y_{rn.}$ The virtual buses connect the generator to the original generator bus with transient reactance. The diagonal elements of Y_{nn}, the diagonal elements of first three columns of Y_{nr}, and the diagonal elements of first three rows of Y_{rn} are the transient reactance of the generators.

Table A.3 Admittance matrix of Y_{nn}

-16.4474j	0	0
0	-8.3472j	0
0	0	-5.5157j

Table A.4 Admittance matrix of Y_{nr}

16.4474j	0	0	0	0	0	0	0	0	0	0
0	8.372j	0	0	0	0	0	0	0	0	0
0	0	5.5157j	0	0	0	0	0	0	0	0

Table A.5 Admittance matrix of Y_{rn}

16.4474j	0	0
0	8.3472j	0
0	0	5.5157j
0	0	0
0	0	0
0	0	0
0	0	0
0	0	0
0	0	0
0	0	0
0	0	0

A.2 State matrix and input matrix

The state matrix has 13×13 elements. Table A.6 demonstrates the state matrix from column 1 to 7 whereas table A.7 demonstrates the state matrix from column 8 to 13. The input matrix is showed in table A.8. The partial differential terms of P and Q are the deviation of complex powers of the generators to the rotor angles and internal voltages of the generators. These terms can be obtained from the jacobian matrix of the generators.

Table A.6 State matrix from column 1 to 7

$-\frac{\overline{K}_{D1}}{2H_1}$	0	0	0	$-\frac{\partial\overline{P}_1}{2H_1\partial\delta_{G2}}$	$-\frac{\partial\overline{P}_1}{2H_1\partial\delta_{G3}}$	0
0	$-\frac{\overline{K}_{D2}}{2H_{G2}}$	0	$\frac{\overline{K}_{D2}}{2H_{G2}}$	$-\frac{\overline{K}_{S2}}{2H_{G2}}-\frac{\partial\overline{P}_2}{2H_{G2}\partial\delta_{G2}}$	$-\frac{\partial\overline{P}_2}{2H_{G2}\partial\delta_{G3}}$	$\frac{\overline{K}_{S2}}{2H_{G2}}$
0	0	$-\frac{\overline{K}_{D3}}{2H_3}$	0	$-\frac{\partial\overline{P}_3}{2H_3\partial\delta_{G2}}$	$-\frac{\partial\overline{P}_3}{2H_3\partial\delta_{G3}}$	0
0	$\frac{\overline{K}_{D2}}{2H_{W2}}$	0	$-\frac{\overline{K}_{D2}}{2H_{W2}}$	$\frac{\overline{K}_{S2}}{2H_{W2}}$	0	$-\frac{\overline{K}_{S2}}{2H_{W2}}$
$-\frac{\omega_o}{P/2}$	$\frac{\omega_o}{P/2}$	0	0	0	0	0
$-\omega_o$	0	ω_o	0	0	0	0
$-\frac{\omega_o}{P/2}$	0	0	$-\frac{\omega_o}{P/2}$	0	0	0
0	0	0	0	$-\frac{(\overline{x}_{d2}-\overline{x}'_{d2})\partial Q_{eo2}}{T_{do2}E'_{qo2}\partial\delta_{G2}}$	$-\frac{(\overline{x}_{d2}-\overline{x}'_{d2})\partial Q_{eo2}}{T_{do2}E'_{qo2}\partial\delta_{G3}}$	0
0	0	0	0	$-\frac{(\overline{x}_{d3}-\overline{x}'_{d3})\partial Q_{eo3}}{T_{do3}E'_{qo3}\partial\delta_{G2}}$	$-\frac{(\overline{x}_{d3}-\overline{x}'_{d3})\partial Q_{eo3}}{T_{do3}E'_{qo3}\partial\delta_{G3}}$	0
0	0	0	0	0	0	0
0	0	0	0	0	0	0
0	0	0	0	0	0	0
0	0	0	0	0	0	0

Table A.7 State matrix from column 8 to 13

$-\dfrac{\partial\overline{P}_1}{2H_1\partial E'_{q2}}$	$-\dfrac{\partial\overline{P}_1}{2H_1\partial E'_{q3}}$	0	0	0	0
$-\dfrac{\partial\overline{P}_2}{2H_{G2}\partial E'_{q2}}$	$-\dfrac{\partial\overline{P}_2}{2H_{G2}\partial E'_{32}}$	0	0	0	0
$-\dfrac{\partial\overline{P}_3}{2H_3\partial E'_{q2}}$	$-\dfrac{\partial\overline{P}_3}{2H_3\partial E'_{q3}}$	0	0	0	0
0	0	0	0	0	0
0	0	0	0	0	0
0	0	0	0	0	0
0	0	0	0	0	0
$a_j-\dfrac{(\overline{x}_{d2}-\overline{x}'_{d2})\partial Q_{eo2}}{T_{do2}E'_{qo2}\partial E'_{q2}}$	$-\dfrac{(\overline{x}_{d2}-\overline{x}'_{d2})\partial Q_{eo2}}{T_{do2}E'_{qo2}\partial E'_{q3}}$	0	0	0	0
$-\dfrac{(\overline{x}_{d3}-\overline{x}'_{d3})\partial Q_{eo3}}{T_{do3}E'_{qo3}\partial E'_{q2}}$	$a_j-\dfrac{(\overline{x}_{d3}-\overline{x}'_{d3})\partial Q_{eo3}}{T_{do3}E'_{qo3}\partial E'_{q3}}$	0	0	0	0
$\dfrac{3\sqrt{2}nD}{\pi L_m\cdot b}$	0	0	$\dfrac{n^2(D-1)}{L_m\cdot b}$	0	0
0	0	$\dfrac{(1-D)}{C_o}$	0	$-\dfrac{D_d}{C_o}$	$-\dfrac{D_q}{C_o}$
0	0	0	$-\dfrac{D_d}{L_s}$	$-\dfrac{R_s}{L_s}$	ω
0	0	0	$\dfrac{D_q}{L_s}$	$-\omega$	$-\dfrac{R_s}{L_s}$

Where a_j is $\dfrac{1}{T_{doj}}\left[-1+\dfrac{(\overline{x}_{dj}-\overline{x}'_{dj})Q_{eoj}}{\left(E'_{qoj}\right)^2}\right]$; j is the number of generator 2 and 3

b is $1+\dfrac{3\sqrt{3}\cdot nDx'_d}{\pi\omega L_m}$

Table A.8 Input matrix

$$
\begin{matrix}
\frac{1}{2H_1} & 0 & 0 & 0 & 0 & 0 & 0 & 0 & 0 & 0 \\
0 & 0 & 0 & 0 & 0 & 0 & 0 & 0 & 0 & 0 \\
0 & 0 & \frac{1}{2H_3} & 0 & 0 & 0 & 0 & 0 & 0 & 0 \\
0 & \frac{1}{2H_{W2}} & 0 & 0 & 0 & 0 & 0 & 0 & 0 & 0 \\
0 & 0 & 0 & 0 & 0 & 0 & 0 & 0 & 0 & 0 \\
0 & 0 & 0 & 0 & 0 & 0 & 0 & 0 & 0 & 0 \\
0 & 0 & 0 & 0 & 0 & 0 & 0 & 0 & 0 & 0 \\
0 & 0 & 0 & \frac{1}{T_{do2}} & 0 & 0 & 0 & 0 & 0 & 0 \\
0 & 0 & 0 & 0 & \frac{1}{T_{do3}} & 0 & 0 & 0 & 0 & 0 \\
0 & 0 & 0 & 0 & 0 & \frac{n^2}{b}\left(\frac{V_{in}}{n}+V_{dc}\right) & 0 & 0 & 0 & 0 \\
0 & 0 & 0 & 0 & 0 & -\frac{I_{Lm}}{C_o} & -\frac{I_d}{C_o} & -\frac{I_q}{C_o} & 0 & 0 \\
0 & 0 & 0 & 0 & 0 & 0 & \frac{V_{dc}}{L_s} & 0 & -\frac{1}{L_s} & 0 \\
0 & 0 & 0 & 0 & 0 & 0 & 0 & \frac{V_{dc}}{L_s} & 0 & -\frac{1}{L_s}
\end{matrix}
$$

Appendix B. Power flow

The full description of the Newton-Raphson power flow can be found from section 9.3 and 9.4 in [69]. To find the power flow, it is important to know the equations of voltage and current of buses. For a system that has *N* buses, the admittance of bus *i* and bus *j* can be expressed in polar coordinates as

$$Y_{ij} = |Y_{ij}|\angle\theta_{ij} = |Y_{ij}|\cos\theta_{ij} + j|Y_{ij}|\sin\theta_{ij} \qquad \text{(B.1)}$$

the voltage of bus *i* is

$$v_i = |V_i|\angle\delta_i = |V_i|(\cos\delta_i + j\sin\delta_i) \qquad \text{(B.2)}$$

The current of bus *i* is

$$I_i = Y_{i1}V_1 + Y_{i2}V_2 + \ldots + Y_{in}V_n = \sum_{n-1}^{N} Y_{in}V_n \qquad \text{(B.3)}$$

The complex conjugate power injected at bus *i* can be expressed as

$$P_i - jQ_i = V_i^* \sum_{n=1}^{N} Y_{in}V_n \qquad \text{(B.4)}$$

Substituting admittance in the equation gives

$$P_i - jQ_i = \sum_{n=1}^{N} |Y_{in}V_iV_n|\angle\theta_{in} + \delta_n - \delta_i \qquad \text{(B.5)}$$

Expand the above equation to obtain the real and reactive powers

$$P_i = |V_i|^2 G_{ii} + \sum_{\substack{n=1 \\ n\neq i}}^{N} |Y_{in}V_iV_n|\cos(\delta_i - \delta_n - \theta_{in}) \qquad \text{(B.6)}$$

$$Q_i = -|V_i|^2 B_{ii} + \sum_{\substack{n=1 \\ n\neq i}}^{N} |Y_{in}V_iV_n|\sin(\delta_i - \delta_n - \theta_{in}) \qquad \text{(B.7)}$$

Let introduce the simple power flow calculation. At each bus *i*, P_{gi}, Q_{gi}, P_{di}, *and* Q_{di} are the real and reactive powers generated and demanded at each bus, respectively. The net powers injected at bus *i* is

$$\begin{aligned} P_{net,i} &= P_{gi} - P_{di} \\ Q_{net,i} &= Q_{gi} - Q_{di} \end{aligned} \qquad \text{(B.8)}$$

The definition of mismatch power is the error of calculated and net injected powers

$$\begin{aligned}\Delta P &= P_{net,i} - P_{cal,i} \\ \Delta Q &= Q_{net,i} - Q_{cal,i}\end{aligned} \tag{B.9}$$

Newton-Raphson power flow and Jacobian matrix

Let consider two equations of two variables x_1 and x_2 with input u. For a specified input u, the solutions of the equations are x_1^*, x_2^*. Assume the initial estimation of the solutions to be x_1^0, x_2^0.

$$g_1(x_1^*, x_2^*, u) = g_1(x_1^0 + \Delta x_1^0, x_2^0 + \Delta x_2^0, u) = 0 \tag{B.10}$$

$$g_2(x_1^*, x_2^*, u) = g_2(x_1^0 + \Delta x_1^0, x_2^0 + \Delta x_2^0, u) = 0 \tag{B.11}$$

The value of Δx determines how far the estimation x^0 is from the actual solution x^*. For a small Δx, we can use approximation with Taylar's series expansion to conclude that

$$g_1(x_1^*, x_2^*, u) = g_1(x_1^0, x_2^0, u) + \Delta x_1^0 \left.\frac{\partial g_1}{\partial x_1}\right|^{(0)} + \Delta x_2^0 \left.\frac{\partial g_1}{\partial x_2}\right|^{(0)} + \ldots = 0 \tag{B.12}$$

$$g_2(x_1^*, x_2^*, u) = g_2(x_1^0, x_2^0, u) + \Delta x_1^0 \left.\frac{\partial g_2}{\partial x_1}\right|^{(0)} + \Delta x_2^0 \left.\frac{\partial g_2}{\partial x_2}\right|^{(0)} + \ldots = 0 \tag{B.13}$$

The above equations can be written in the matrix form as

$$\left.\begin{bmatrix} \frac{\partial g_1}{\partial x_1} & \frac{\partial g_1}{\partial x_2} \\ \frac{\partial g_2}{\partial x_1} & \frac{\partial g_2}{\partial x_2} \end{bmatrix}\right|_{x_1^0, x_2^0}^{(0)} \begin{bmatrix} \Delta x_1^0 \\ \Delta x_2^0 \end{bmatrix} = \begin{bmatrix} 0 - g_1(x_1^0, x_2^0, u) \\ 0 - g_2(x_1^0, x_2^0, u) \end{bmatrix} \tag{B.14}$$

To find the next estimation, x_1^1, x_2^1, we must solve the error $\Delta x_1^0, \Delta x_2^0$

$$\begin{bmatrix} \Delta x_1^0 \\ \Delta x_2^0 \end{bmatrix} = \left(\left.\begin{bmatrix} \frac{\partial g_1}{\partial x_1} & \frac{\partial g_1}{\partial x_2} \\ \frac{\partial g_2}{\partial x_1} & \frac{\partial g_2}{\partial x_2} \end{bmatrix}\right|^{(0)} \right)^{-1} \begin{bmatrix} 0 - g_1(x_1^0, x_2^0, u) \\ 0 - g_2(x_1^0, x_2^0, u) \end{bmatrix} \tag{B.15}$$

The next estimation is

$$\begin{bmatrix} x_1^1 \\ x_2^1 \end{bmatrix} = \begin{bmatrix} x_1^0 \\ x_2^0 \end{bmatrix} + \begin{bmatrix} \Delta x_1^0 \\ \Delta x_2^0 \end{bmatrix} \tag{B.16}$$

The partial derivatives of equation B.14 is called Jacobain matrix. The function g_1 and g_2 is equal to 0 based on the actual solutions x_1^*, x_2^*. Therefore, the right hand side of the equation B.15 is called the mismatch of function g_1 and g_2.

$$J^0 \begin{bmatrix} \Delta x_1^0 \\ \Delta x_2^0 \end{bmatrix} = \begin{bmatrix} \Delta g_1^0 \\ \Delta g_2^0 \end{bmatrix} \tag{B.17}$$

Then the next iteration starts with

$$\begin{bmatrix} \dfrac{\partial g_1}{\partial x_1} & \dfrac{\partial g_1}{\partial x_2} \\ \dfrac{\partial g_2}{\partial x_1} & \dfrac{\partial g_2}{\partial x_2} \end{bmatrix}^{(1)}_{x_1^1, x_2^1} \begin{bmatrix} \Delta x_1^1 \\ \Delta x_2^1 \end{bmatrix} = \begin{bmatrix} \Delta g_1^1 \\ \Delta g_2^1 \end{bmatrix} \tag{B.18}$$

The iteration can continue until the error is less than the acceptable value. Let us apply the Newton-Raphson method to the power system. At this moment, consider all buses to be load buses or *P*-*Q* buses. For any *N* bus system, the two unknown variables are $\delta_i, |V_i|$ for all non-slack buses since the slack bus has specified value of $\delta_i, |V_i|$. The function g_1 and g_2 can be considered as real and reactive powers, *P* and *Q* with two unknown variables $\delta_i, |V_i|$ as x_1 and x_2. We can define the power mismatches of any bus *i* as

$$\begin{aligned} \Delta P_i &= P_{net,i} - P_{cal.i} \\ \Delta Q_i &= Q_{net,i} - Q_{cal.i} \end{aligned} \tag{B.19}$$

From the equation, the power mismatch equations can be expanded as

$$\Delta P_i = \frac{\partial P_i}{\partial \delta_2}\Delta\delta_2 + \frac{\partial P_i}{\partial \delta_3}\Delta\delta_3 + \ldots + \frac{\partial P_i}{\partial \delta_n}\Delta\delta_n + \frac{\partial P_i}{\partial |V_2|}\Delta|V_2| + \frac{\partial P_i}{\partial |V_3|}\Delta|V_3| + \ldots + \frac{\partial P_i}{\partial |V_n|}\Delta|V_n| \quad \text{(B.20)}$$

$$\Delta Q_i = \frac{\partial Q_i}{\partial \delta_2}\Delta\delta_2 + \frac{\partial Q_i}{\partial \delta_3}\Delta\delta_3 + \ldots + \frac{\partial Q_i}{\partial \delta_n}\Delta\delta_n + \frac{\partial Q_i}{\partial |V_2|}\Delta|V_2| + \frac{\partial Q_i}{\partial |V_3|}\Delta|V_3| + \ldots + \frac{\partial Q_i}{\partial |V_n|}\Delta|V_n| \quad \text{(B.21)}$$

For *N* bus system, there are *2(N-1)* equations. The powers of the slack bus are calculated when the powers of all other buses are defined. Differentiate the power equations gives

$$\frac{\partial P_i}{\partial \delta_j} = |V_i V_j Y_{ij}|\sin(\delta_i - \theta_{ij} - \delta_j) \quad \text{(B.22)}$$

$$\frac{\partial P_i}{\partial \delta_i} = -\sum_{\substack{n=1\\ n\neq i}}^{N} |V_i V_n Y_{in}|\sin(\theta_{in} + \delta_n - \delta_i) \quad \text{(B.23)}$$

$$\frac{\partial Q_i}{\partial \delta_j} = -|V_i V_j Y_{ij}|\cos(\theta_{ij} + \delta_j - \delta_i) \quad \text{(B.24)}$$

$$\frac{\partial Q_i}{\partial \delta_i} = \sum_{\substack{n=1\\ n\neq i}}^{N} |V_i V_j Y_{ij}|\cos(\theta_{in} + \delta_n - \delta_i) \quad \text{(B.25)}$$

$$\frac{\partial P_i}{\partial |V_j|} = |V_i Y_{ij}|\cos(\theta_{ij} + \delta_j - \delta_i) \quad \text{(B.26)}$$

$$\frac{\partial P_i}{\partial |V_i|} = 2|V_i|G_{ii} + \sum_{\substack{n=1\\ n\neq i}}^{N} |V_n Y_{in}|\cos(\theta_{in} + \delta_n - \delta_i) \quad \text{(B.27)}$$

$$\frac{\partial Q_i}{\partial |V_i|} = -2|V_i|B_{ii} + \sum_{\substack{n=1\\ n\neq i}}^{N} |V_n Y_{in}|\sin(\theta_{in} + \delta_n - \delta_i) \quad \text{(B.28)}$$

$$\frac{\partial Q_i}{\partial |V_j|} = |V_i Y_{ij}|\sin(\theta_{ij} + \delta_j - \delta_i) \quad \text{(B.29)}$$

For *N* bus system, there are *2(N-1)* equations. The powers of the slack bus are calculated when the powers of all other buses are defined.The power mismatch can be written in the jacobian matrix form as

$$\begin{bmatrix} \frac{\partial P_2}{\partial \delta_2} & \cdots & \frac{\partial P_2}{\partial \delta_n} & | & \frac{\partial P_2}{\partial |V_2|} & \cdots & \frac{\partial P_2}{\partial |V_n|} \\ \vdots & J_{11} & \vdots & | & \vdots & J_{12} & \vdots \\ \frac{\partial P_n}{\partial \delta_2} & \cdots & \frac{\partial P_n}{\partial \delta_n} & | & \frac{\partial P_n}{\partial |V_2|} & \cdots & \frac{\partial P_n}{\partial |V_n|} \\ - & - & - & | & - & - & - \\ \frac{\partial Q_2}{\partial \delta_2} & \cdots & \frac{\partial Q_2}{\partial \delta_n} & | & \frac{\partial Q_2}{\partial |V_2|} & \cdots & \frac{\partial Q_2}{\partial |V_n|} \\ \vdots & J_{21} & \vdots & | & \vdots & J_{22} & \vdots \\ \frac{\partial Q_n}{\partial \delta_2} & \cdots & \frac{\partial Q_n}{\partial \delta_n} & | & \frac{\partial Q_n}{\partial |V_2|} & \cdots & \frac{\partial Q_n}{\partial |V_n|} \end{bmatrix} \cdot \begin{bmatrix} \Delta \delta_2 \\ \vdots \\ \Delta \delta_n \\ -- \\ \partial |V_2| \\ \vdots \\ \partial |V_n| \end{bmatrix} = \begin{bmatrix} \Delta P_2 \\ \vdots \\ \Delta P_n \\ -- \\ \Delta Q_2 \\ \vdots \\ \Delta Q_n \end{bmatrix} \tag{B.30}$$

Appendix C. Matlab program

C.1 File “Parameter_Testsystem1”

```
% The network consists of 10 nodes (230kV Network with 3 Generators and 3
% Loads)
% Base power is 100MVA and base voltage is 230kV)

% Transmission lines

R45=0.0100; X45=0.0850; Z45=R45+j*X45; Y45=1/Z45; Y54=Y45; % Bus 4-5;
R46=0.0170; X46=0.0920; Z46=R46+j*X46; Y46=1/Z46; Y64=Y46; % Bus 4-6;
R46=0.0170; X46=0.0920;
R58=0.0320; X58=0.1610; Z58=R58+j*X58; Y58=1/Z58; Y85=Y58; % Bus 5-7;
R69=0.0390; X69=0.1700; Z69=R69+j*X69; Y69=1/Z69; Y96=Y69; % Bus 6-9;
R710=0.02; X710=0.10; Z710=R710+j*X710; Y710=1/Z710; Y107=Y710; % Bus 7-9
R89=0.0119; X89=0.1008; Z89=R89+j*X89; Y89=1/Z89; Y98=Y89; % Bus 8-9;

%Shunt admittance

B7=0.0745; Y7=j*B7; % node 7;
B8=0.1045; Y8=j*B8; % node 8;
B9=0.179; Y9=j*B9; % node 9;
B6=0.179; Y6=j*B6; % node 6;
B4=0.088; Y4=j*B4; % node 4;
B5=0.153; Y5=j*B5; % node 5;
Y10=Y7; % node 10 and 7

%Regulating Transformer

R=0.0; X=0.03; Z=R+j*X; Y=1/Z; % Resistance is ignored
t=1.005;
```

```
% Transformator parameter

X7=0.0625; Z7T=j*X7; Y7T=1/Z7T; % Transformer in node 7;
X3=0.0586; Z3T=j*X3; Y3T=1/Z3T; % Transformer in node 3;
X1=0.0576; Z1T=j*X1; Y1T=1/Z1T; % Transformer in node 1;
X2=0.02; Z2T=j*X2; Y2T=1/Z2T; % Transformer in node 2

% Admittance matrix

Y_admin=zeros(11,11);
Y_admin(1,1)=Y1T; Y_admin(1,4)=-Y1T;
Y_admin(2,2)=t^2*Y; Y_admin(2,11)=-t*Y;
Y_admin(3,3)=Y3T; Y_admin(3,9)=-Y3T;
Y_admin(4,4)=Y1T+Y45+Y46+Y4; Y_admin(4,1)=-Y1T; Y_admin(4,5)=-Y45;
Y_admin(4,6)=-Y46;
Y_admin(5,5)=Y54+Y58+Y5; Y_admin(5,4)=-Y54; Y_admin(5,8)=-Y58;
Y_admin(6,6)=Y64+Y69+Y6; Y_admin(6,4)=-Y64; Y_admin(6,9)=-Y69;
Y_admin(7,7)=Y710+Y7T+Y7;  Y_admin(7,8)=-Y7T; Y_admin(7,10)=-Y710;
Y_admin(8,8)=Y7T+Y89+Y8+Y85; Y_admin(8,7)=-Y7T; Y_admin(8,9)=-Y89;
Y_admin(8,5)=-Y85;
Y_admin(9,9)=Y3T+Y96+Y98+Y9; Y_admin(9,3)=-Y3T; Y_admin(9,6)=-Y96;
Y_admin(9,8)=-Y98;
Y_admin(10,10)=Y2T+Y107+Y10; Y_admin(10,11)=-Y2T; Y_admin(10,7)=-Y107;
Y_admin(11,11)=Y+Y2T; Y_admin(11,2)=-t*Y; Y_admin(11,10)=-Y2T;
```

C.2 File “LoadFlow_Testsystem1”

```
% Calculation of the initial condition for dynamic response of the system
% Linarized Jacobi-Matrix

Parameter_TestSystem1;
Y_system=Y_admin;

%% Start parameter for calculation (voltages and angles and the powers as well)
coef_U=1;
coef_S=1/100;

% Node 1 (Slack Node)
U1=1.040; phi0=0; U1k=U1*exp(j*phi0)*coef_U;

% Node 2
U2=1.025;     phi2=-0.0015;        P2=-140;       Q2=57;       S2=(P2+j*Q2)*coef_S;
U2k=U2*exp(j*phi2)*coef_U;

% Node 3
U3=1.025;     phi3=-0.0026;        P3=-100.0;     Q3=20;       S3=(P3+j*Q3)*coef_S;
U3k=U3*exp(j*phi3)*coef_U;

%Node 4;
U4=1.026;        phi4=-0.0027;       P4=0.0;        Q4=0;        S4=(P4+j*Q4)*coef_S;
U4k=U4*exp(j*phi4)*coef_U;

%Node 5;
U5=0.996;     phi5=-0.0017;        P5=125.0;      Q5=-50;      S5=(P5+j*Q5)*coef_S;
U5k=U5*exp(j*phi5)*coef_U;
```

```
%Node 6;
U6=1.013;   phi6=-0.0017;   P6=90.0;   Q6=-30;   S6=(P6+j*Q6)*coef_S;
U6k=U6*exp(j*phi6)*coef_U;

%Node 7;
U7=1.026;   phi7=-0.0017;   P7=0;   Q7=0;   S7=(P7+j*Q7)*coef_S;
U7k=U7*exp(j*phi7)*coef_U;

%Node 8;
U8=1.016;   phi8=-0.0017;   P8=80.0;   Q8=-35.0;   S8=(P8+j*Q8)*coef_S;
U8k=U8*exp(j*phi8)*coef_U;

%Node 9;
U9=1.032;   phi9=-0.0020;   P9=0.0;   Q9=0.0;   S9=(P9+j*Q9)*coef_S;
U9k=U9*exp(j*phi9)*coef_U;

%Node 10;
U10=1.022;   phi10=-0.00180;   P10=0.0;   Q10=0.0;   S10=(P10+j*Q10)*coef_S;
U10k=U10*exp(j*phi10)*coef_U;

%Node 11;
U11=1.012;   phi11=-0.00160;   P11=0.0;   Q11=0.0;   S11=(P11+j*Q11)*coef_S;
U11k=U11*exp(j*phi11)*coef_U;

P=[real(S2); real(S3); real(S4); real(S5); real(S6); real(S7); real(S8); real(S9); real(S10);
real(S11)];
Q=[imag(S2); imag(S3); imag(S4); imag(S5); imag(S6); imag(S7); imag(S8); imag(S9);
imag(S10); imag(S11)];

S=[S2; S3; S4; S5; S6; S7; S8; S9; S10; S11];
```

```
% Admittance matrix

Y_admin=Y_system;
[N M]=size(Y_admin);

U=[U1k; U2k; U3k; U4k; U5k; U6k; U7k; U8k; U9k; U10k; U11k];  %Voltage vector

Ustart=U; % Start condition for LoadFlow Calculation

%% Newton-Raphson method with linearization process
for iter=1:100; % Iteration number
J=JacobianMatrixFull(Y_admin,U);
% Calculation of the power
[Us Soutput]=VoltageCalculationFull(J,Y_admin,U,P,Q);
U=Us
end
UNewton=U;
```

C.3 Function “JacobianMatrixFull”

```
function J=JacobianMatrixFull(Y_admittance,U)
[N M]=size(Y_admittance);

%% dP/dU

J1=zeros(N,M);
for n=1:N
   for m=1:M
      if (m==n) % Diagonal elements
         J1(n,m)=2*abs(U(n))*abs(Y_admittance(n,m))*cos(angle(Y_admittance(n,m)));
         for k=1:M
            if (k~=n)
               J1(n,m)=J1(n,m)+abs(Y_admittance(n,k))*abs(U(k))*cos(angle(U(n))-
angle(U(k))-angle(Y_admittance(n,k)));
            end
         end
      end
      if  (m~=n) % off-diagonal elements
         J1(n,m)=abs(Y_admittance(n,k))*abs(U(n))*cos(angle(U(n))-angle(U(m))-
angle(Y_admittance(n,m)));
      end
   end
end

%% dP/dphi

J2=zeros(N,M);
for n=1:(N)
   for m=1:(M)
```

```
        if (m==n)
            for k=1:M
                if (k~=n)

J2(n,m)=J2(n,m)abs(Y_admittance(n,k))*abs(U(k))*abs(U(n))*sin(angle(U(n))-
angle(U(k))-angle(Y_admittance(n,k)));
                end
            end
        end
        if (n~=m)
            J2(n,m)=abs(Y_admittance(n,m))*abs(U(m))*abs(U(n))*sin(angle(U(n))-
angle(U(m))-angle(Y_admittance(n,m)));
        end
    end
end

%% dQ/dU

J3=zeros(N,M);
for n=1:(N)
    for m=1:(M)
        if (m==n)
            J3(n,m)=-2*abs(U(m))*abs(Y_admittance(n,m))*sin(angle(Y_admittance(n,m)));
            for k=1:M
                if (k~=n)
                    J3(n,m)=J3(n,m)+abs(Y_admittance(n,k))*abs(U(k))*sin(angle(U(n))-
angle(U(k))-angle(Y_admittance(n,k)));
                end
            end
        end
        if (m~=n)
```

```
            J3(n,m)=abs(Y_admittance(n,m))*abs(U(n))*sin(angle(U(n))-angle(U(m))-angle(Y_admittance(n,m)));
        end
    end
end

%% dQ/dphi

J4=zeros(N,M);
for n=1:(N)
    for m=1:(M)
        if (m==n)
            for k=1:M
                if (k~=n)
            J4(n,m)=J4(n,m)+abs(Y_admittance(n,k))*abs(U(k))*abs(U(n))*cos(angle(U(n))-angle(U(k))-angle(Y_admittance(n,k)));
                end
            end
        end
        if (m~=n)
            J4(n,m)=-abs(Y_admittance(n,m))*abs(U(m))*abs(U(n))*cos(angle(U(n))-angle(U(m))-angle(Y_admittance(n,m)));
        end
    end
end

%% Jacobi Matrix

J=[J1(2:1:N,2:1:M) J2(2:1:N,2:1:M); J3(2:1:N,2:1:M) J4(2:1:N,2:1:M)]; % ganze Jacobi – Matrix
```

C.4 Function “VoltageCalculationFull”

```
function [U,S,delta]=VoltageCalculationFull(JMatrix,Y_admittance,U,P,Q)

[N M]=size(Y_admittance);
I=Y_admittance*U;
Ss=diag(U)*conj(I);

PQs=[real(Ss(2:1:(N))); imag(Ss(2:1:(N)))]; % Initial complex powers
delta=([P;Q]-PQs);  % Power mismatch
deltaU=inv(JMatrix)*delta;

for k=1:1:(N-1)
   U(k+1)=(abs(U(k+1))+deltaU(k))*exp(j*angle(U(k+1))+j*(deltaU(k+N-1)));
end
Us=U;
S=Ss;
```

C.5 File “GenAngle_Testsystem1”

```
% Calculation of the Initional Condition for the Generators

XG1=0.0608; ZG1=j*XG1;  YG1=1/ZG1;
XG2=0.1198; ZG2=j*XG2;  YG2=1/ZG2;
XG3=0.1813; ZG3=j*XG3;  YG3=1/ZG3;

Zgd=diag([ZG1 ZG2 ZG3]);

I=conj(Soutput./UNewton) % Current Conditionen from Load Flow Calculation

UZgd=Zgd*I(1:3) %Voltage on Generator Impedances
Ugenerator=(UNewton(1:3)+UZgd) % Voltage Generator
GeneratorAngle=angle(Ugenerator)*180/pi;
GeneratorMagnitude=abs(Ugenerator);

% Calculate load impedance

y5Load=conj(S5)/(abs(UNewton(5)))^2;
y6Load=conj(S6)/(abs(UNewton(6)))^2;
y8Load=conj(S8)/(abs(UNewton(8)))^2;

% Replacement of the active load in passive admittances

Y_system=Y_admin;
Y_system(5,5)=Y_system(5,5)-y5Load;
Y_system(6,6)=Y_system(6,6)-y6Load;
Y_system(8,8)=Y_system(8,8)-y8Load;

V=inv(Y_system)*[I(1:3); 0; 0; 0; 0; 0; 0; 0; 0;];
```

```
I1=Y_system*(UNewton)

Y_system_ext=zeros(14,14);
Y_system_ext(4:14,4:14)=Y_system;

% Add virtual buses
% Ynn
Y_system_ext(1,1)=YG1;
Y_system_ext(2,2)=YG2;
Y_system_ext(3,3)=YG3;
% Ynr and Yrn
Y_system_ext(1,4)=-YG1; Y_system_ext(4,1)=-YG1;
Y_system_ext(2,5)=-YG2; Y_system_ext(5,2)=-YG2;
Y_system_ext(3,6)=-YG3; Y_system_ext(6,3)=-YG3;
%
Y_system_ext(4,4)=Y_system_ext(4,4)+YG1;
Y_system_ext(5,5)=Y_system_ext(5,5)+YG2;
Y_system_ext(6,6)=Y_system_ext(6,6)+YG3;

I2=Y_system_ext*[Ugenerator; UNewton]

% Reduction of the Admittance Matrix to the Generator nodes

Y_system_reduc=Y_system_ext(1:3,1:3)-
Y_system_ext(1:3,4:14)*inv(Y_system_ext(4:14,4:14))*Y_system_ext(4:14,1:3);
I3=Y_system_reduc*Ugenerator
S0=Ugenerator.*conj(I3);
```

```
JacobiFull=JacobianMatrixFullBase(Y_system_reduc,Ugenerator); % Deviation of complex powers of generators

%% Formulation of the Matrices for dynamic Simulation
% Defining the constant terms in the state matrix

M1=(diag(imag(S0(1:3)))*eye(3,3)*diag(1./abs(Ugenerator(1:3)).^2))

M2=JacobiFull(4:6,1:3);                    %dQ/dV
M2(1,1:3)=M2(1,1:3)/abs(Ugenerator(1));
M2(2,1:3)=M2(2,1:3)/abs(Ugenerator(2));
M2(3,1:3)=M2(3,1:3)/abs(Ugenerator(3));

M3=JacobiFull(4:6,4:6);                    %dQ/dphi
M3(1,1:3)=M3(1,1:3)/abs(Ugenerator(1));
M3(2,1:3)=M3(2,1:3)/abs(Ugenerator(2));
M3(3,1:3)=M3(3,1:3)/abs(Ugenerator(3));

K1=JacobiFull(1:3,1:3);                    %dP/dV
K2=JacobiFull(1:3,4:6);                    %dP/dphi


% %%%Modeling of generators%%%%%
% Initial conditions
%Moment of intertia
H1=6.4;  Hg2=18.74; H3=3.01; Hw2=2.52;
H=diag(0.5./[H1;Hg2;H3;Hw2]);
%Xd-Xd'
Xs1=0.0852; Xs2=0.776; Xs3=1.1312;
Xs=diag([Xs1;Xs2;Xs3]);
%Transient time constant
```

```
Td1=8.96; Td2=6; Td3=5.89;
Td=diag([Td1;Td2;Td3;]);
%Damping
Kd1=1.5; Kd2=0.883; Kd3=2; Ks2=0.888;
Kd=diag([Kd1;Ks2;Kd2;Kd3]);
%Pole pair
P=30;
%Base frequency
Ws=2*pi*60

% State matrix
Z=zeros(9,9);

%Angular Speed
Z(1:4,1:4)=-diag([Kd1;Kd2;Kd3;Kd2])*H; Z(2,4)=Kd2*H(2,2); Z(4,2)=Kd2*H(4,4);
Z(1,5:6)=-H(1,1)*K2(1,2:3); Z(2,5:6)=-H(2,2)*K2(2,2:3); Z(3,5:6)=-H(3,3)*K2(3,2:3);
Z(2,5)=Z(2,5)-Ks2*H(2,2); Z(2,7)=Ks2*H(2,2); Z(4,5)=Ks2*H(4,4); Z(4,7)=-
Ks2*H(4,4);
Z(1,8:9)=-H(1,1)*K1(1,2:3); Z(2,8:9)=-H(2,2)*K1(2,2:3); Z(3,8:9)=-H(3,3)*K1(3,2:3);
%Angle
Z(5:7,2:4)=diag([Ws/P; Ws; Ws/P;]);
Z(5,1)=-Ws/P; Z(6,1)=-Ws; Z(7,1)=-Ws/P;
%Voltage
Z(8,5:6)=-Xs2*M3(2,2:3)/Td2; Z(9,5:6)=-Xs3*M3(3,2:3)/Td2;
Z(8:9,8:9)=(-1*eye(2,2)+Xs(2:3,2:3).*M1(2:3,2:3)).*diag(1./diag(Td(2:3,2:3)),0)
Z(8,8:9)=Z(8,8:9)-Xs2*M2(2,2:3)/Td2; Z(9,8:9)=Z(9,8:9)-Xs3*M2(3,2:3)/Td3;



%%%Add-on Power Electronics%%%


%Base quantities
```

```
Vb=3; Ib=21.4; Zb=0.126; Lb=0.00335; Cb=0.021; Wb=377;

%Parameters of power converters
%
%Base quantities
Vb=2.7; Ib=21.4; Zb=0.126; Lb=0.00335; Cb=0.021; Wb=377;

%
n=2;
Vdc=3;
Lm=0.5e-3;
Co=2e-3;
L=2e-3;
R=0.01;



%Calculate Per Unit
Lm=Lm/Lb;
L=L/Lb;
Co=Co/Cb
R=R/Zb;
Vdc=Vdc/Vb;
W=1;

%Calculate operating points
Vin=3*sqrt(2)/pi*abs(Ugenerator(2))*.68/2.7;
Vd=abs(U(2));  %L-L,rms
D=n*Vdc/(Vin+n*Vdc);

%
Id=abs(real(Soutput(2)))/Vd;
```

```
Iq=imag(Soutput(2))/Vd
Sdc=real(Soutput(2))-0.01*(Id^2+Iq^2)+imag(Soutput(2))*1.02*j;
Idc=abs(real(Sdc))/Vdc;
Dd=(Vd-W*L*Iq)/Vdc;
ILm=Idc/(1-D);
Dq=W*L*Id/Vdc;
Vq=0;

a=1+n*D/Lm*XG2/W*3*sqrt(3)/pi

%State Matrix
A=zeros(13,13);
A(1:9,1:9)=Z;
A(10,8)=n*D/Lm*3*sqrt(2)/pi/a; A(10,11)=n^2*(D-1)/Lm/a;
A(11,10)=(1-D)/Co; A(11,12)=-Dd/Co; A(11,13)=-Dq/Co;
A(12,11)=Dd/L; A(12,12)=-R/L; A(12,13)=W;
A(13,11)=Dq/L; A(13,12)=-W; A(13,13)=-R/L;

%%%Input Matix%%%
%Input Matix
B=zeros(13,8);

%Angular speed
B(1,1)=H(1,1); B(3,3)=H(3,3); B(4,2)=H(4,4);

%Voltage
B(8,4)=1/Td2; B(9,5)=1/Td3;

%Power Electronics
B(10,6)=n^2*Lm*(Vin/n+Vdc)/a; B(11,6)=-ILm/Co; B(11,7)=-Id/Co; B(11,8)=-Iq/Co;
B(12,6)=0; B(12,7)=Vdc/L;
```

```
B(13,6)=0; B(13,8)=Vdc/L;

%%%Output matrix%%%%
C=eye(13,13);

%%%Matrix D%%%
D=zeros(13,8);

%%%Feedback Control%%%

Q=diag([500 500 500 500 500 500 500 500 500 500 500 500 500]);
R=diag([5 5 5 5 5 5 5 5]);
[k,s,e]=lqr(A,B,Q,R,0);
```

Reference

1. “Fact sheet”, http://www.awea.org/pubs/factsheets/Market_Update.pdf
2. Hau E., “Wind turbines: fundamentals, technologies, applications, economics”, chapter 3, Springer press
3. http://www1.eere.energy.gov/windandhydro/wind_how.html
4. “Power control of wind turbines”, http://www.windpower.org/en/tour/wtrb/powerreg.htm#anchor1387445
5. “Wind turbine technology: fundamental concepts of wind turbine engineering”, page 66, ASME Press.
6. Rudion K.,“Aggregated modeling of wind farm”, Dissertation in electrical engineering at University of Magdeburg, Chapter 4
7. “Offshore wind farm”, http://www.awea.org/pubs/factsheets/Offshore_fact_sheet.pdf
8. Blaabjerg F., Chen Z., “Power electronics for wind turbines”, Chapter 3, 1st edition, Morgan & Claypool Publishers.
9. Kazimierkowski M.P.,Krishnan R.,Blaabjerg F.,“Control in power electronics:selected problems”, chapter 13, Academic press
10. Momoh J.A., El-Hawary M.E.,“Electric systems, dynamics, and stability with artificial intelligence applications”, Chapter 1, New York : Marcel Dekker
11. Grigsby L.L.,“Electric Power Engineering Handbook Second Edition” Chapter 7, Taylor & Francis Group, I.I.C
12. Kundur P., edited by Balu N.J., Lauby M.K.,“Power system stability”, Chapter 1, New York : McGraw-Hill, c1994
13. Miller, N.W., Sanchez-Gasca, J.J., Price, W.W., Delmerico, R.W.,“Dynamic modeling of GE 1.5 and 3.6 MW wind turbine-generators for stability simulations”, Power Engineering Society General Meeting, 2003, IEEE Volume 3, 13-17 July 2003 Page(s):1977 - 1983 Vol. 3
14. Behnke, M.R., Muljadi, E.,“Reduced Order Dynamic Model For Variable-Speed Wind Turbine With Synchronous Generator And Full Power Conversion Topology”, Future Power Systems, 2005 International Conference on 18-18 Nov. 2005 Page(s):6 pp. – 6

15. Slootweg, J.G., Polinder, H., Kling, W.L.,“Initialization of Wind Turbine Models in Power System Dynamic Simulations”, Power Tech Proceedings, 2001 IEEE Porto Volume 4, 10-13 Sept. 2001 Page(s):6 pp. vol.4
16. Holdsworth, L., Wu, X.G., Ekanayake, J.B., Jenkins, N.,“Direct solution method for initializing doubly-fed induction wind turbines in power system dynamic models”, Generation, Transmission and Distribution, IEE Proceedings-Volume 150, Issue 3, May 2003 Page(s):334 - 342
17. Wei Qiao; Harley, R.G.; Venayagamoorthy, G.K.;,“Dynamic Modeling of Wind Farms with Fixed-speed Wind Turbine Generators”, Power Engineering Society General Meeting, 2007. IEEE 24-28 June 2007 Page(s):1 - 8
18. Cidras, J., Feijoo, A.E.,“A linear dynamic model for asynchronous wind turbines with mechanical fluctuations”, Power Systems, IEEE Transactions on Volume 17, Issue 3, Aug. 2002 Page(s):681 - 687
19. Hsu, M.-C. Chen, M.-J. Huang, W.-L. Lin, Y.-J.,“Simulating Dynamic Behavior of a Grid-Linked Wind Farm Power System in Taiwan”, Electrotechnical Conference, 2004. MELECON 2004. Proceedings of the 12th IEEE Mediterranean Volume 3, 12-15 May 2004 Page(s):1029 - 1032 Vol.3
20. Tabesh, A., Iravani, R.,“Small-signal model and dynamic analysis of variable speed induction machine wind farms”, Renewable Power Generation, IET Volume 2, Issue 4, December 2008 Page(s):215 – 227
21. Palle, B., Simoes, M.G., Farret, F.A.,“Dynamic simulation and analysis of parallel self-excited induction generators for islanded wind farm systems”, Industry Applications, IEEE Transactions on Volume 41, Issue 4, July-Aug. 2005 Page(s):1099 – 1106
22. Estanqueiro, A.I.,“A Dynamic Wind Generation Model for Power Systems Studies”, Power Systems, IEEE Transactions on Volume 22, Issue 3, Aug. 2007 Page(s):920 – 928
23. Muljadi, E., Ellis, A.,,“Validation of Wind Power Plant Models”, Power and Energy Society General Meeting - Conversion and Delivery of Electrical Energy in the 21st Century, 2008 IEEE 20-24 July 2008 Page(s):1 – 7

24. Demiray, T., Milano, F., Andersson, G.,“Dynamic Phasor Modeling of the Doubly-fed Induction Generator under Unbalanced Conditions”, Power Tech, 2007 IEEE Lausanne 1-5 July 2007 Page(s):1049 – 1054
25. Wei Deng, Xisheng Tang, Zhiping Qi,“Research on dynamic stability of hybrid wind/PV system based on Micro-Grid”, Electrical Machines and Systems, 2008. ICEMS 2008. International Conference on
17-20 Oct. 2008 Page(s):2627 - 2632
26. Lindner D.,“Multivariable control”, Lecture notes of multivariable control system at Virginia Tech
27. Zdzislaw B.,“Modern control theory”, Chapter 1, Springer Press
28. Choi, N.S., Cho, J.G., Cho, G.H.,“A general circuit topology of multilevel inverter”, Power Electronics Specialists Conference, 1991. PESC '91 Record., 22nd Annual IEEE 24-27 June 1991 Page(s):96 - 103
29. Rodriguez, J., Jih-Sheng Lai, Fang Zheng Peng,“Multilevel inverters: a survey of topologies, controls, and applications”, Industrial Electronics, IEEE Transactions on Volume 49, Issue 4, Aug. 2002 Page(s):724 - 738
30. Jih-Sheng Lai, Fang Zheng Peng,“Multilevel converters-a new breed of power converters”, Industry Applications Conference, 1995. Thirtieth IAS Annual Meeting, IAS '95., Conference Record of the 1995 IEEE, Volume 3, 8-12 Oct. 1995 Page(s):2348 - 2356 vol.3
31. Sirisukprasert, S., Huang, A.Q., Lai, J.-S.,“Modeling, analysis and control of cascaded-multilevel converter-based STATCOM”, Power Engineering Society General Meeting, 2003, IEEE. Volume 4, 13-17 July 2003 Page(s):
32. “IEEE recommended practices and requirements for harmonic control in electrical power systems”,
33. Eskander, M.N.; Ibrahim, W.M.; Abdel Aziz, M.M.; Ibrahim, A.M., “Generation Control of A Wind Farm With Variable Speed Wind Turbines For High Power Quality,” in *Proc. 2005 IEEE Telecommunications Conference, 2005. INTELEC '05.*, pp. 443 - 448.
34. Chen, Z.; Spooner, E., “Grid Power Quality with Variable-Speed Wind Turbines,” *IEEE Trans. Energy Conversion,* vol.16, pp.148 – 154 June 2001

35. Mohan N., Undeland T.M., Robbins W.P.,“Power electronics: converters, applications, and design”, Chapter 5, page 103, JohnWiley & Sons. Inc.
36. Erickson R.W.,Maksimovic D.,“Fundamental of power electronics: second edition”, Chapter 6, page 161, Kluwer Academic Publishers
37. McGrath, B.P., Holmes, D.G.,“Multicarrier PWM strategies for multilevel inverters”, Industrial Electronics, IEEE Transactions on Volume 49, Issue 4, Aug. 2002 Page(s):858 - 867
38. Vorperian, V.,“Simplified analysis of PWM converters using model of PWM switch. Continuous conduction mode”, Aerospace and Electronic Systems, IEEE Transactions on Volume 26, Issue 3, May 1990 Page(s):490 – 496
39. Se-Kyo Chung, “A phase tracking system for three phase utility interface inverters,” *IEEE Trans. Power Electronics,* vol. 15, pp. 431 - 438, May 2000.
40. P. Kundur ; edited by Neal J. Balu, Mark G. Lauby, “Power system stability and control,” New York : McGraw-Hill, c1994 pp. 320
41. Ridley, R.B.; Cho, B.H.; Lee, F.C.Y., “Analysis and interpretation of loop gains of multiloop-controlled switching regulators,” *IEEE Trans.Power Delivery*, vol. 3, pp. 489 - 498, Oct. 1988.
42. Fang Zheng Peng; Jih-Sheng Lai, “Generalized instantaneous reactive power theory for three-phase power systems,” *IEEE Trans. Instrumentation and Measurement*, vol. 45, pp. 293 - 297, Feb. 1996.
43. Norman S. Nise, “Control systems engineering,” 4th ed., Hoboken, NJ : John Wiley, c2004, ch.9-10
44. Schulz, S.; Cho, B.H.; Lee, F.C., “Design considerations for a distributed power system,” in Proc. 1991 IEEE Power Electronics Specialists Conf., pp. 611-617.
45. Byungcho Choi; Jaeyeol Kim; Cho, B.H.; Seungwon Choi; Wildrick, C.M., “Designing control loop for DC-to-DC converters loaded with unknown AC dynamics,” *IEEE Trans. Industrial Electronics*, vol. 49, pp. 925 - 932, Aug. 2002.
46. Wildrick, C.M.; Lee, F.C.; Cho, B.H.; Choi, B., “A method of defining the load impedance specification for a stable distributed power system,” *IEEE Trans. Power Electronics,* vol. 10, pp. 280 - 285, May 1999

47. Castro, R.M.G., Ferreira de Jesus, J.M.,“A wind park reduced-order model using Singular Perturbation Theory”, Energy Conversion, IEEE Transaction on Volume 11, Issue 4, Dec. 1996 Page(s):735 - 741
48. Undrill, J.M., Turner, A.E.,“Construction of power system electromechanical equivalents by modal analysis”, IEEE Transactions on Power Apparatus and Systems Volume PAS-90, Issue 5, Sept. 1971 Page(s):2049 - 2059
49. Moore, B.,“Principal component analysis in linear systems: Controllability, observability, and model reduction”, Automatic Control, IEEE Transactions on Volume 26, Issue 1, Feb 1981 Page(s):17 - 32
50. Slootweg, J.G., Kling, W.L.,“Aggregated Modeling of Wind Parks in Power System Dynamics Simulations”, Power Tech Conference Proceedings, 2003 IEEE Bologna Volume 3, 23-26 June 2003 Page(s):6 pp. Vol.3
51. Peoller M., Achilles S.,“Aggregated Wind Park Models for Analyzing Power System Dynamics”
52. Anderson F.,“Power system control and stability: second edition”, Wiley Interscience.
53. Slootweg, J.G., de Haan, S.W.H., Polinder, H., Kling, W.L.,“Modeling wind turbines in power system dynamics simulations”, Power Engineering Society Summer Meeting, 2001. IEEE Volume 1, 15-19 July 2001 Page(s):22 - 26 vol.1
54. Tao Sun, Z. Chen, F. Blaabjerg, "Transient stability of DFIG wind turbines at an external short-circuit fault", Wind Energy, vol. 8, pp. 345-360, 2005.
55. Holdsworth L., Wu X. G., Ekanayake J. B., Jenkins N.. "Comparison of fixed speed and doubly-fed induction wind turbines during power system disturbances". IEE Proc. Generation, Transmission and Distribution, vol.150, no. 3, pp. 343-352, 2003.
56. P. Ledesma, J. Usaola, JL. Rodriguez, "Transient stability of a fixed speed wind farm", Renewable Energy, vol. 28, no. 9, pp. 1341-1355, 2003.
57. V.Akhmatov, A.H. Nielse, "Fixed-speed active-stall wind turbines in offshore applications", European Trans. on Electrical Power, vol. 15, no.2, pp. 1-1 12, 2005.

58. Salman K. Salman, Anita L. J. Teo. "Windmill modeling consideration and factors influencing the stability of a grid-connected wind power based embedded generator", IEEE Transactions on Power Systems, vol. 18, no.2, pp. 793-802, 2003.
59. M. Martins, A. Perdana, P. Ledesma, E. Agnehom, 0. Carlson, "Validation of fixed speed wind turbine dynamic models with measured data", Renewable Energy, vol. 32, pp. 1301-13 15, 2007.
60. S.M.Muyeen, R.Takahashi, T.Murata, J.Tamura, "Transient Stability Enhancement of Wind Generator by Online Logical Controller with the Consideration of Initial Condition Settings", International Power Electronic Conference (IPEC05), S29-1, pp. 1065-1071, April, 2005.
61. H. LI, Z. Chen, L. Han, "Comparison and evaluation of induction generator models in wind turbine systems for transient stability of power system", 2006 International Conference on Power System Technology. POWERCON2006.
62. Daniel J. Trudnowski ,Jawad M. Khan, Eric M. Petritz, "Fixed-speed wind generator and wind park modeling for transient stability studies",IEEE Transactions on Power Systems, vol. 19, no. 4, pp. 1911-1917,2004.
63. J.Tamura, T.Yamazaki, R.Takahashi, S.Yonaga, H.Kubo, Y.Matsumura, "Analysis of Transient Stability of Wind Generators", Conference Record ofICEM 2002, No. 148, 2002.
64. Usaola P., "Dynamic incidence of wind turbines in network with high wind penetration", Presented at IEEE Power Engineering Society Summer Meeting, Vancouver, Canada, 15th-19th July 2001
65. Li, H., Chen, Z.,"Transient Stability Analysis of Wind Turbines with Induction Generators Considering Blades and Shaft Flexibility", Industrial Electronics Society, 2007. IECON 2007. 33rd Annual Conference of the IEEE 5-8 Nov. 2007 Page(s):1604 – 1609
66. Lubosny Z.,"Wind turbine operation in electric power systems", Chapter 5, page 87-92, Springer
67. Padiyar K.R.,"Power system dynamics: stability and control", Chapter 3, John Wiley & Sons (Asia) Pte. Ltd.

68. Sauer, P. W., Pai,M.A.,“ Power system dynamics and stability”, Upper Saddle River, N.J. : Prentice Hall
69. Grainger S.,“Power system analysis”, Chapter 9, McGrawhill International edition
70. Wang X.,“Modal analysis of large interconnected power systems”, Energietechnik Press
71. Franklin G.F.,Powell J.D., Emami-Naeini A.,“Feedback control of dynamic systems”, Chapter 3, Presntice Hall
72. Burl, B.J.,“Linear Optimal Control”,Chapter 6, Addison-Wesley
73. Positive definite from Mathworld, http://mathworld.wolfram.com/PositiveDefiniteMatrix.html
74. Navarro I.R.,“Dynamic load models for power systems: Estimation of time-varying parameters during normal operation”, Dissertation of department of industrial electrical engineering and automation at Lund University
75. Lai L.L.,“Power system restructuring and deregulation: trading, performance, and information technology”, John Wiley&Sons, Ltd.
76. Kleit A.N.,“Electric choices: deregulationand the future of electric power”, Rowman & Littlefield Publishers Ltd.
77. Liu J., Thorp J.S., Chiang H.D.,“Modal control of large flexible structures using collocated actuators and sensors”, *IEEE transactions on Automatic control*, Vol.37,pp. 143-147, January 1992